Functional Composites from Graphene-Stabilised Silicone Emulsions

Marcus O'Mara

Submitted for the degree of Doctor of Philosophy

University of Sussex

November 2020

Declaration

I hereby declare that this thesis has not been and will not be submitted in whole or in part to another University for the award of any other degree.

Signature:

Marcus O'Mara

UNIVERSITY OF SUSSEX

Marcus O'Mara, Doctor of Philosophy

Functional Composites from Graphene-Stabilised Silicone Emulsions

Summary

Novel nanocomposites are emerging as promising electromechanical sensors with unparalleled sensitivities compared to traditional materials. If a percolating network of graphene can be embedded within a matrix, then system scale conductivity is conferred. The conductivity depends on a number of factors related to the morphology of the sheets and the network they form. Thus, any changes to the network brought about by mechanical stimuli such as strain will manifest as a change in conductivity. Soft polymers such as silicone elastomers undergo significant deformation even under small stress, making them ideal candidates for high sensitivity applications. Forming a percolating network of graphene in silicone is challenging due to their chemical dissimilarity. Despite this, several examples now exist of randomly distributed networks of graphene in silicone with a demonstrably high electrical response to applied strain. This work aims to extend the study of this system to templated networks of graphene in silicone by way of Pickering emulsification. The ability to structure a graphene network in this way confers additional benefits; such as a greatly reduced percolation threshold, higher conductivities at lower loadings and enhanced sensitivity. Further, we observe a robust exponential sensitivity to tensile strain, loading level-independent sensitivity and record high $\Delta R/R_0$ which facilitates the measurement of pulse and breathing (simultaneously) and high strain joint bending. This is extended to systems of lightly-interdiffused composites with potential for compressive strain or pressure sensing over an wide sensing range between 10^3-10^6 Pa, which may enable the development of electronic skin.

Publications

1. **O'Mara, M**. A., Ogilvie, S. P., Large, M. J., Amorim, A., Sehnal, A. C., Lynch, P. J., Salvage, J. P., Jurewicz, I., King, A. A. K., Dalton, A. B., Ultrasensitive Strain Gauges Enabled by Graphene-Stabilized Silicone Emulsions. Adv. Funct. Mater. 2020, 30, 2002433. https://doi.org/10.1002/adfm.202002433

2. Ogilvie, S. P., Large, M. J., Cass, A., Amorim Graf, A., Sehnal, A. C., **O'Mara, M. A.**, Lynch, P. J., Salvage, J., Alfonso, M., Poulin, P., King, A., Dalton, A. B. (2020). Nanosheet-stabilized emulsions: ultra-low loading segregated networks and surface energy determination of pristine few-layer 2D materials. arXiv.org, [2005.06330]. https://arxiv.org/abs/2005.06330

3. Large, M. J., Ogilvie, S. P., Amorim, A., Lynch, P. J.,**O'Mara, M. A.**, Waters, T., Jurewicz, I., Salvage, J. P., Dalton, A. B., Large-Scale Surfactant Exfoliation of Graphene and Conductivity-Optimized Graphite Enabling Wireless Connectivity. Adv. Mater. Technol. 2020, 5, 2000284. https://doi.org/10.1002/admt.202000284

4. Peter J. Lynch, Sean P. Ogilvie, Matthew J. Large, Aline Amorim Graf, **Marcus A. O'Mara**, James Taylor, Jonathan P. Salvage, Alan B. Dalton, Graphene-based printable conductors for cyclable strain sensors on elastomeric substrates. Carbon, Volume 169, 2020, Pages 25-31, ISSN 0008-6223, https://doi.org/10.1016/j.carbon.2020.06.078.

5. Sean P. Ogilvie, Matthew J. Large, **Marcus A. O'Mara**, Peter J. Lynch, Cheuk Long Lee, Alice A. K. King, Claudia Backes and Alan B. Dalton, 2D Materials,

Volume 6, Number 3, 6 031002, https://doi.org/10.1088/2053-1583/ab0dc3.

Patents

Title:

Composite materials made from Pickering emulsions

Abstract:

The present invention relates to a method of making a composite material, the method comprising: (1) forming a Pickering emulsion comprising a continuous liquid phase, a discontinuous liquid phase, and a 2D material; wherein the discontinuous liquid phase comprises a polysiloxane and a curing agent; (2) leaving the Pickering emulsion formed in step (1) in a sealed system for sufficient time to at least partially cure the polysiloxane; and (3) allowing any remaining liquid to evaporate.

Publication Number: WO/2021/028702

Publication Date:

18.02.2021

Applicants:

THE UNIVERSITY OF SUSSEX [GB]/[GB]

ALLIANCE RUBBER COMPANY [US]/[US]

Inventors:

Alan Dalton, Matthew Large, Sean Ogilvie, **Marcus O'Mara**

Conferences

1. **HeteroNanoCarb 2020, Benasque, Spain** - Advances and applications in carbon related nanomaterials: From pure to doped structures including heteroatom layers - Presentation - Ultra-sensitive strain gauges via graphene stabilised emulsions.

2. **Nanotexnology 2019, Thessalonki, Greece** - Latest advances in Nanosciences and Nanotechnologies - Poster Presentation: Emulsion-templated graphene-silicone composites with a robust exponential sensitivity to strain.

3. **NanoApp 2019, Munich, Germany** - Present and emerging challenges in dimensionally engineered materials - Attendee.

4. **Liquid Phase Exfoliation Workshop 2018, Dublin, Ireland** - Latest advances in Liquid Phase Exfoliation processes and applications - Presentation: Ultra-sensitive strain gauges via graphene stabilised emulsions.

5. **Hengstberger Symposium 2018, Heidelberg, Germany** - The role of defects in low-dimensional nanostructures - Attendee.

6. **Liquid Phase Exfoliation Symposium 2018, Sussex, UK** - 10 Years of Liquid Phase Exfoliation - Attendee.

7. **NanoteC18, Brighton, UK** - Nanoscale Carbon Conference - fullerenes, nanotubes, graphene and related two-dimensional Materials - Member of the organising committee.

Acknowledgements

Undertaking a PhD in Physics is never a decision to be taken lightly. Though the road is long and seldom smooth, the combined influence of a brilliant team and support network often mean the difference between success and failure. To my supervisor Alan, I'm grateful for the opportunity you entrusted to me and for all that you've taught me, academic and otherwise. I hope that this thesis finds a deserving place on your bookshelf.

To Sean, it is difficult to adequately articulate my thanks to you as both a mentor and a friend. You've made the few years both intellectually stimulating and hilarious in great but equal measure. Your contribution to my personal development and support throughout my project will not be forgotten.

To Matt, the 'King of the Lab', leader of the scientific cavalry when all hope of understanding seems lost, I'm grateful for your project saving contributions and refreshingly cutting wit. I look forward to a signed first edition of Echoes of Astyr.

To Peter, your stoicism and good virtue is greatly admired, as is your commitment to a hard-earned Guinness or Tally Ho as appropriate. Thank you for always being so approachable and answering questions big or small, smart or silly.

To Aline, its been nothing less than a pleasure to embark on this journey with you. I am envious of your work ethic and dedication, which is second to none. You're a credit to the group, and I have no doubt of the great things you'll achieve in this field. Thank you for keeping me sane.

To Manoj, thank you for always giving me more credit than I was due. Your enthusiasm is contagious and so often lifted my mood. To Abdullah, Frank, Keiran and Hannah, its been a lot of fun working with you. I hope that your energy and drive continues to show through you're work and I wish you all the very best of success with your projects.

To my house-mates Aine, Alicia, Grace and Jaci, you've been no less than spectacular. I can't imagine a better group of people to live with during the final stages of my PhD. You've been so welcoming and supportive since I moved in, and consistently help to focus me and provide a much needed distraction at just the right moments.

To my university brothers, Harry and Viet, thank you for your continued interest in my project, the constant pep-talks and your un-wavering reliability as good friends only ever a phone call away. Onwards and upwards!

To my twin brother Tom, your incredible success and support are an inspiration and I hope that one day soon I can suitably repay you for everything you've done for me, especially at the most difficult of times.

Contents

List of Figures

Chapter 1

Introduction

Our world is becoming increasingly and irreversibly connected. Billions of devices are working together to generate enormous volumes of data upon which new insights and opportunities for technological advancement will arise. Low-cost, flexible and scalable material technologies will enable a range of next-generation sensors designed to work with the human body. [1] From embedded heart rate and blood pressure monitoring to electronic skins, sensors will be utilised in combination with artificial intelligence to provide continuous health monitoring and automatic diagnosis, in addition to smarter robotics that can feel their surroundings and react accordingly.

Spearheading the technological revolution is graphene - arguably the most exciting material to be isolated and studied following the turn of the 21^{st} century. Its meteoric rise to wonder material status can be attributed to its array of superlative properties; extremely high Young's modulus, ballistic electron transport, exceptional thermal conductivity, impermeability to gases and unique optoelectronic properties, to name a few. [2–4] The potential application space is as rich as it is varied, promising a host of new and improved technologies in composites, electronics, energy storage and conversion and health. [4, 5] In Europe alone, the Graphene Flagship represents an unprecedented investment of €1 billion in order to realise the potential benefits that graphene and related 2D materials are

expected to deliver.

Polymer nanocomposites represent one of the largest fields of study for graphene. [6] A cursory Google Scholar search reveals 710,000 scholarly articles related to 'graphene composites'. The overarching goal of composite research is to construct enhanced materials with tunable properties (dependent on the relative loading levels and network structure) that can be tailored to the desired application, to imbue electrical conductivity or to enhance mechanical toughness for example. As graphene already boasts a laundry list of desirable optoelectronic, mechanical and thermal properties, the motivation to discover and demonstrate new and effective material combinations is clear. Composites present a tantalising avenue to realising these properties in macroscopic systems. In this thesis, a novel method for the production of functional graphene composites is developed and explored.

Polymers - long chains of repeating organic molecule monomer units - have become ubiquitous, underpinning many aspects of modern society. The interplay of long chains, interwoven and mobile at the molecular scale give rise to interesting physical properties such as viscoelastic behaviour [7–9] One interesting subclass of polymers are polysiloxanes, which consist of a long 'backbone' of repeating Si-O units from which various functional groups can be attached. Polydimethylsiloxane (PDMS) is one such example in which methyl groups (CH_3) are covalently bonded to the Si atoms in the Si-O backbone, resulting in a material that is biocompatible, elastic, transparent and durable. As a result, PDMS is frequently utilised in healthcare, aerospace, food, and microfluidics industries. [10–12] Evidently, the prospect of combining silicones such as PDMS with graphene is an attractive one although in practice is somewhat non-trivial.

Naturally, the properties of a composite are determined primarily by those of the constituent materials. However, their relative volume fractions, filler morphology, chemistry and arrangement within the composite also play a significant role. [13] As the quantity

of conductive filler or loading level increases, so too does the overall conductivity of the composite. For any given filler morphology, there exists a statistical average loading level at which a continuous, percolating network of the filler material forms throughout the composite known as the percolation threshold. [14] Around the percolation threshold, there is a dramatic change in the conductivity with loading level, usually spanning several orders of magnitude. [15–20]

Independently of loading level, electrical conductivity will be dominated by the conductivity of the nanosheets and also by the distribution of intersheet junction resistances. [21–25] This distribution is determined by the number of sheets and their relative arrangements; their 'contact area' and the distance that electrons must tunnel between them. Under certain processing conditions, it is possible to invoke the selective localisation of the nanosheets - *i.e.* to create a composite in which there is an excluded volume that the nanosheets will not occupy. Intuitively, this leads to a reduction in the percolation threshold since a network is more likely to be formed at lower loadings. [26–33]

Since the tunnelling current between two conductors decays exponentially with increasing distance, deformations to the a conductive network can lead to marked changes to the overall conductivity of the composite. [34,35] By placing a highly conductive network in an elastic polymer matrix, one opens the possibility of a strain sensor that is able to withstand large amounts of strain and remain conductive enough to be detected with simple electronics. [36–56] Further, soft (low modulus) polymer matrices such as polysiloxanes will deform significantly even under small mechanical stress. This ensures a high level of sensitivity, in addition to excellent stress transfer and conformability to enables the possibility of on-skin sensors. [41,48,49]

Randomly distributed networks of graphene in silicone have been demonstrated and their performance has been impressive. [41,52] However, there is considerable scope for improved performance if the morphology of graphene network can be controlled. [13] [38] While some

examples exist, their scalability and cost of production is prohibitive. [40, 57] It is this author's belief that if such a network can be demonstrated and these issues can be overcome, a viable alternative to commercial strain and pressure sensors based on nanocomposites could be realised. In doing so, this thesis aims to elucidate the key parameters required to control the composite morphology and understand how they influence macroscopic properties and overall sensor performance.

In Chapter 2, standard methods and theory for the formation and evaluation of nanocomposite networks are explored. Chapter 3 sees a range of important characterisation techniques discussed in terms of working principles and limitations. Chapter 4 details the formation and characterisation of graphene-stabilised silicone emulsions. Chapter 5 exploits the phenomenological behaviour described in Chapter 4 to create ultra-sensitive, mechanically robust strain sensors based on graphene stabilised emulsions and assesses their performance relative to nanocomposite strain sensors in the literature. Chapter 6 aims to refine the materials and production process in favour of producing economically viable and highly sensitive pressure sensors. Taken together, an understanding of the morphological influence of graphene networks on conductivity and sensor capability is discussed along with future work in Chapter 7.

Chapter 2

2D Materials, Synthesis and Processing

2.1 2D Materials

The study of 2D materials has undergone a resurgence in the field of materials science, garnering a fervent renewal of interest since the Nobel prize winning work of Andre Geim and Konstantin Novoselov on isolated graphene monolayers in 2004. [2] Prior to their discovery, conventional wisdom dictated that free-standing monolayers of any material would be thermodynamically unstable. [4] However, this notion was soon overturned with the observation of large, mechanically-exfoliated monolayer graphene in addition to bilayer and few-layer graphene (FLG). [2] Indeed, a subtle 3D wrinkling effect is now thought to give graphene monolayers resistance to otherwise destabilising thermal fluctuations, in combination with strong C-C bonds. [4] Despite the simplicity of the Scotch Tape delamination technique, the produced flakes were of remarkably high quality and exhibited surprising electrical properties [3], including extremely high carrier mobilities and densities, opening up a promising avenue for the continued miniaturisation of transistors. Other Van der Waals layered crystals such as molybdenum disulfide (MoS_2) and boron nitride (BN)

were subsequently investigated [58] while significant efforts have been made to improve the scalability and efficiency of 2D material synthesis. [59, 60] The success of this work has brought about a plethora of novel material systems with enormous potential applications.

2.1.1 Graphene

Graphene is a 2D sheet of sp^2 hybridized carbon atoms arranged in a hexagonal lattice, and forms the basis of a number of important allotropes, including 0D fullerenes, 1D carbon nanotubes, and 3D graphite as shown in Figure 2.1. [4] Each carbon atom has four electrons (s, p_x, p_y, p_z) available for chemical interaction. The s, p_x and p_y electrons hybridise to form strong covalent σ bonds to its nearest neighbours while the remaining p_z electron is highly mobile, hybridising with other p_z electron orbitals to form a gas of delocalised electrons that completely fill the π valence band and leave the π^* conduction band empty. [61, 62] Although the density of states is zero at the Dirac point, graphene exhibits a minimum conductivity associated with the quantum unit of conduction. [2] The application of an external electric field will shift the Fermi level and enable the conduction of electrons (positive bias) or holes (negative bias). Further, graphene has been shown to have an optical transparency of 97.7%, [63] thermal conductivity of 5000 W $m^{-}1$ K^{-1} [64] and specific surface area of 2630 m^2 g^{-1}. [65]

2.1.2 Electrical Properties

The electronic structure of graphene can be derived using the tight binding model, and shows semi-metallic behaviour in addition to an unusual linear relationship between the energy and momentum of the charge carriers at the so called K and K' points, regions of high symmetry in the reciprocal lattice, as shown in Figure 2.2. [4, 61, 62, 66, 67]

The linearity of the energy momentum relationship is a direct consequence of the geometry of the lattice and implies that electrons and holes travel with zero *effective*

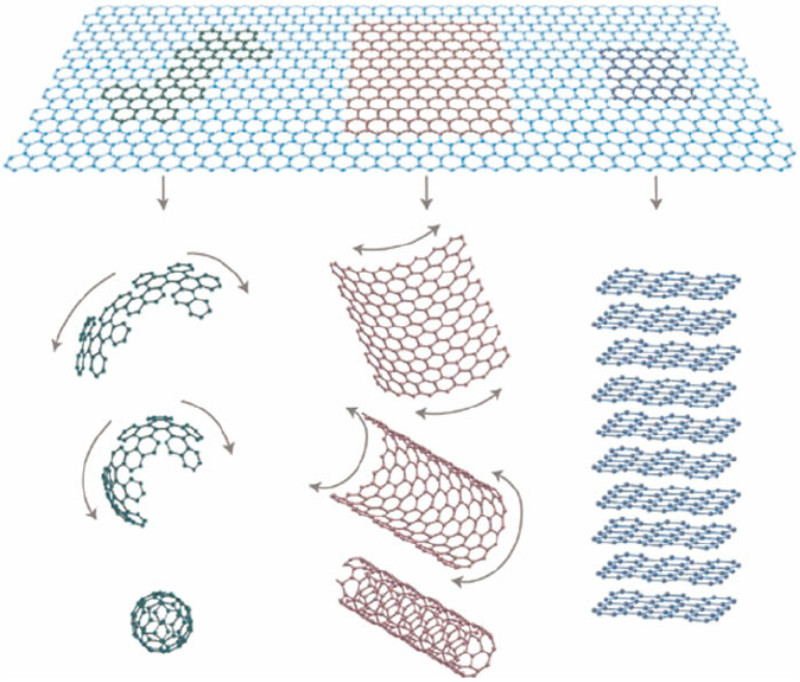

Figure 2.1: **Formation of carbon allotropes from wrapping, rolling and stacked 2D graphene**; 0D fullerenes, 1D nanotubes and 3D graphite. Reproduced from [4].

mass. [4] That is, there is minimal interaction between charge carriers and atomic nuclei that would otherwise scatter travelling charge carriers, maximising their overall drift velocity and mean free path length. [68] The carrier mobility is intrinsically limited by phonon scattering to 200,000 cm^2 V^{-1} s^{-1} at room temperature. Mobilities of 15,000 cm^2 V^{-1} s^{-1} have been observed experimentally with the difference attributed to defects within the lattice. [3, 69, 70] As a result, graphene has been viewed as a potential successor to silicon based transistors, given that state of the art silicon transistors exhibit significantly smaller carrier mobilities of $\sim$1400 m^2 V^{-1} s^{-1}. In practice however, the lack of an inherent band gap results in low on-off ratios in graphene based transistors and high static power consumption. [71]

2.1.3 Mechanical Properties

Until the first successful demonstration of isolated monolayer graphene sheets, it was commonly thought that 2D sheets of any material would be thermodynamically unstable.

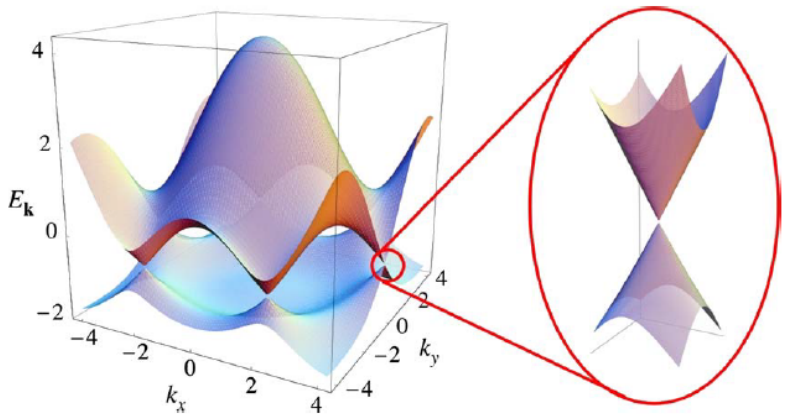

Figure 2.2: **Electronic band structure of monolayer graphene**, showing the linear dispersion relation exhibited in massless Dirac fermions at the K and K' points of the Brillouin zone where the conduction and valence bands meet. Reproduced from [66].

[4, 72] In fact, the stability and record breaking mechanical properties are owed to the strength of the σ bonds. Defect-free monolayer graphene is widely touted as the strongest material ever discovered, with a breaking strength of 42 N m^{-1} and a corresponding intrinsic tensile strength of ∼130 GPa and stiffness of 1 TPa; assuming an effective thickness of 0.335 nm. [73] To illustrate, a 1 m^2 sheet of graphene would be able to support the weight of a 4 kg cat, despite being only one atom thick. Indeed, the discovery of graphene's impressive mechanical properties led to a surge in interest as researchers looked to utilise graphene in various composite systems for mechanical reinforcement. [74]

2.2 Liquid Processing of 2D Materials

For all of graphene's superlative qualities, there has to be a strong economic case for its adoption. Initially, success can be found in a commercial setting by creating new markets from novel applications that exploit graphene's unique properties, or significantly improved performance for an existing application. [5, 75] As the cost of production falls however, so to does the improvement threshold required to bring a graphene product to market.

Inevitably, the ratio of performance to cost increases with growing expertise in processing methods.

A multitude of production processes exist for graphene (and its related materials), and the reality is that each produces a different *kind* of graphene, with various morphological and chemical properties arising from the specific processing conditions. [13, 76] While each has its merits, only those that strike a reasonable balance between electronic quality, price and scalability will ever be commercially relevant. [77, 78]

The benchmark for graphene quality (with respect to structural integrity) is set by mechanically-exfoliated highly-orientated pyrolytic graphite using Scotch Tape. [2] Aside from the obvious scalability issues, there is a lack of selectivity using this method since large (>10 µm) sheets must be actively located and processed. For pristine graphene, two methods have emerged dominant - liquid phase exfoliation (LPE) and chemical vapour deposition (CVD).

Typically for CVD, a hydrocarbon gas such as methane is passed over a transition metal substrate such as copper at very high temperatures of around 1000 °C. The carbon atoms dissociate and seed the substrate in domains of varying crystallographic orientation, forming large polycrystalline films with carrier mobilities up to 7350 $cm^2\ V^{-1}s^{-1}$. [5, 79] Such films are of very high optoelectronic quality, with >90% transparency and <30 Ω/□, enabling large, flexible screens up to 30" [80]. Unfortunately, many electronic applications require the graphene to be transferred to an alternative (usually dielectric) substrate, while the temperature requirements are highly energy intensive, increasing the overall complexity and expense of the technique. For applications where such high crystal quality and size is not a strict necessity and mass throughput and processability is preferred, such as in the production of inks, composites and coatings, liquid phase exfoliation is the natural choice. [58]

2.2.1 Liquid Phase Exfoliation

Liquid phase exfoliation (LPE) is one of the major routes to producing 2D materials. In contrast to CVD, where graphene is grown 'bottom-up' from a 0D point to a 2D sheet, LPE involves the 'top-down' delamination of 3D crystals into 2D sheets. For graphene, this is usually achieved by dispersing graphite powder in an appropriate solvent and applying enough hydrodynamic shear to overcome the Van der Waals attraction between individual layers. Energy delivery strategies include ultrasonication, high-shear mixing or high-pressure homogenisation. [58, 59, 81–90]

Ultrasonication results in a process called cavitation, in which the ultrasonic oscillation leads to the formation and subsequent collapse of bubbles or voids, resulting in a powerful shock-wave that exfoliates the graphite crystal. [58, 86] High-shear mixing relies on the generation of a high shear force between a rotor and stator. High-pressure homogenisation drives the dispersion through microchannels [60] or toward fluid flowing in the reverse direction [90] at pressures up to 300 MPa to generate shear and promote exfoliation. [87]

In all cases, attractive inter-sheet forces will seek to re-aggregate the newly exfoliated sheets to reduce their interfacial energy with the liquid phase. In order to minimise this effect, a solvent system that closely mimics the surface energy of the nanosheets is preferred. 'Good' solvents (*N*-methylpyrrolidone, dimethylformamide, benzyl benzoate) [91] were found to have surface tensions of around 40 mN m^{-1}, although they generally suffer from high toxicity and high boiling points, which makes their eventual removal more challenging. The use of low boiling points has been demonstrated although these are generally less effective at preventing re-aggregation. Water is a naturally poor solvent for graphene owing to its high polarity and surface tension (73 mN m^{-1}) by extension. Indeed, the high interfacial energy between water and graphitic materials is readily characterisable, manifesting as hydrophobicity. Nanosheets can however be electrostatically stabilised through the addition of surfactants with hydrophilic heads and hydrophobic tail groups

(e.g. sodium dodecyl sulfate, Triton X-100) [86, 88, 92, 93] or sterically stabilised by certain polymers to protect against re-aggregation. [58] It should be noted however that the presence of such additives will hamper the electronic conductivity of the end-product, although this can be mitigated through additional washing or annealing steps. [89]

A major drawback of LPE is the difficulty in controlling the distribution of flake lengths and layer numbers that arise following the exfoliation process. [58] Monolayers exhibit the best electrical properties but are typically too small for effective composite mechanical reinforcement, often measuring at less than 1 µm along their longest dimension . [58] While the strength of graphene's σ bonds greatly exceed the Van der Waals attraction between atomic layers, exfoliation is an inherently violent process and tearing of the nanosheets along the plane is expected and observed. Indeed, the average area of a nanosheet is given empirically by Equation 2.1;

$$\langle LW \rangle = D_{ML}^2 \langle N \rangle^{\beta} \tag{2.1}$$

where L and W correspond to the length and width of the sheet, N the number of layers in the sheet, D_{ML} (≈ 40 nm for graphene) a material dependent constant associated with the size of a monolayer, and $\beta = 2.5 \pm 0.5$ an empirical constant. [83] Simply put, thinner sheets tend to be smaller sheets.

Since nanosheet morphology is heavily deterministic of the resulting properties, further processing of the exfoliated dispersion is usually required. Size selection is can be achieved via one or more centrifugation steps, whereby a dispersion of sheets are subject to a large centrifugal force (typically hundreds or thousands of G's) for minutes or hours. Since the size of a nanosheet is related to the gravitational force experienced, largeer, thicker sheets will sediment while smaller, thinner sheets will remain dispersed in the supernatant. This can be repeated multiple times under increasingly intense centrifugal fields to select for nanosheets within a desired size range, a process known as cascade centrifugation. [59]

To extract the nanosheets from suspension, a final centrifugation step could be performed

with the sediment retained or, alternatively, the suspension can be vacuum filtered and washed with deionised (DI) water. In both cases, most of the unbound surfactant is removed and the solids content can be extracted and measured via Thermogravimetric analysis. The exfoliated nanosheets can then be redispersed at high concentrations in a new solvent via ultrasonication. [90]

2.3 Nanosheet Networks and Composite Materials

As outlined in the introduction, composite materials generate significant interest due to the broad range of material properties that can be engineered by selecting the right combination of matrix and filler. Although polymers have an incredibly diverse range of properties they are almost always insulating, which can limit the number of applications. Carbon derivatives, such as carbon black (CB) [94–99], carbon fibres (CFs) [100–104], carbon nanotubes (CNTs) [105–109] and graphene related materials (GRMs) [110–114] may be added to polymers to imbue conductivity and enhance mechanical strength. Car tyres, for example, are manufactured with carbon-black to increase durability, [115] while carbon-fibre reinforced polymers have become synonymous with high performance aerospace materials owing to their high strength to weight ratio. [116] Carbon nanotubes appeared as a natural successor to carbon fibres due to their superior electromechanical properties at the microscale. Realising the same properties at the macroscale is much more challenging however. [117] Though nanotube networks typically percolate at very low loading levels due to their high aspect ratio, at high loading levels, CNT-based composites often become too brittle for many applications. [15, 118]

Graphene nanoplatelets (GNPs) are similarly attractive as a filler material due to their excellent electromechanical properties and high aspect ratios. [13] Composites require significant quantities of filler by nature, so it is advantageous that GNPs can be produced on the tonne scale via liquid phase exfoliation. [86]

One property of PDMS that presents a challenge when seeking to produce nanocomposites with desirable properties is the high rotational freedom of the polymer backbone. [119] This allows methyl groups with a characteristically low surface energy (≈ 52 mN m^{-1}) [120] and chemical reactivity to present themselves at interfaces. The consequence is that a homogeneous dispersion of layered nanomaterials (≈ 70 mN m^{-1}) [58, 86, 121, 122] within a PDMS matrix becomes challenging due to the creation of a high energy barrier to mixing.

One method to counter this is by adopting a Hansen parameter approach [123] whereby mutually compatible solvents are identified based on their chemical similarity to both the nanosheets and matrix. This enables the effective dispersion of nanosheets in addition to the solvation or dissolution of the polymer melt, in turn facilitating the homogeneous blending of PDMS with a nanosheet dispersion. [91] Once the solvent is removed, the high viscosity of PDMS kinetically prevents long-range motion of the nanosheets and significant re-aggregation such that an isotropic composite can be formed. [41]

2.3.1 Percolation Theory

Composites can be made conductive by adding a sufficient quantity of conductive filler to an insulating matrix. The statistical average loading level at which a percolating network forms is known as the percolation threshold, ϕ_c. As the loading level increases, the composite transitions from insulating, to percolating, to conducting. [14–16, 29, 30, 33, 51, 124, 125] Pre-percolation, the dominant conduction mechanism is based on electron tunnelling, a quantum mechanical phenomena whereby the electrons have an associated probability of tunnelling through a potential barrier (the height of which depends on the filler work function and matrix conductivity) that decays exponentially with increasing tunnelling distance. As the loading level increases through the percolation threshold, the average filler to filler tunnelling distance decreases and the current rises accordingly. Above the percolation threshold, a ‘connected’ network is formed and the conductivity is mostly

determined by the filler conductivity. For many network configurations, the conductivity as a function of loading level is well described by Equation 2.2; [15, 41, 125, 126]

$$\sigma \propto \sigma_0(\phi - \phi_c)^{n_e} \quad \text{for} \quad \phi > \phi_c \tag{2.2}$$

where ϕ is the filler loading level, σ_0 is usually similar to the filler conductivity and n_e is the so-called percolation exponent. Physically, it corresponds to the rate at which the conductivity saturates above the percolation threshold, where low values of n_e imply rapid saturation. The saturation rate reflects the range of junction resistances within the composite; higher values of n_e imply a larger range of junction resistances. Since the tunnelling current is extremely sensitive to the distance between fillers, n_e is a reasonable indicator of how uniform their spatial distribution is with respect to one another. Nanocomposites in the literature tend to have values of < 4, although exponents as low as 1.33 [15] and high as 11.9 have been reported. [41]

The percolation threshold is a useful tool for comparing various processing techniques involved in composite manufacture since it depends on the aspect ratio of the filler and the distribution of the filler within the network. Aspect ratio scales with graphene quality [86], while the efficient distribution of the filler is critical to reducing the number of junctions to promote higher conductivities at low loadings. Since the network morphology and resultant electromechanical properties are largely dictated by the processing method, [13] it is instructive to consider some common production schema.

2.3.2 Random *vs* Segregated Networks

A simple method to incorporate graphene into a polymer matrix that results in a random network is melt blending, whereby the filler is distributed in the network using high-shear forces. [127–130] It is a routine industrial process with immediate scalability. However, as the viscosity of the polymer melt increases, so too do the shear forces required to facilitate homogeneous dispersion - which can lead to folding, crumpling and scission of the sheets

along the basal plane. [131] This reduces the aspect ratio of the sheets, increasing the percolation threshold and number of junctions, reducing the overall conductivity. [132]

Solution blending may be used to overcome the issues associated with high polymer viscosity. In this scenario, a relatively viscous polymer is mixed with a dispersion of graphene in a mutually compatible solvent. [41]. This prevents the nanosheets from re-aggregating when introduced to the polymer by reducing the enthalpy of mixing. By extension, less energy is required to ensure a homogeneous dispersion of nanosheets, mitigating sheet folding, crumpling and scission. While the electrical properties are therefore improved, the use of solvents is less environmentally friendly and they eventually have to be removed. The difficulty lies in finding mutually compatible solvents that simultaneously disperse the graphene nanosheets and solvate the polymer, although Hansen solubility parameter matching can be used to identify possible candidates. [58, 133]

Segregated networks rely on the selective localisation of filler within the matrix to enable higher conductivities at lower loadings. Several methods to achieve this exist, including layer-by-layer assembly[[134], latex blending [15, 125] and emulsion templating. [135–139] For the sake of brevity, only the latter two are discussed herein.

Latexes are aqueous dispersions of polymeric particles tens or hundreds of nanometers in size. If the aqueous phase is allowed to evaporate, the latex particles will coalesce and, in the presence of a cross-linking agent (e.g. sulfur) may be vulcanised into an elastomer. [140, 141] There are now several examples of combining aqueous dispersions of nanomaterials (e.g. CNTs, [15] graphene [125]) with latex. These composites naturally promote the formation of a segregated network, as the diffusion of the nanomaterial into the latex particle is orders of magnitude slower than the diffusion through the aqueous phase due to viscosity effects. As the blend dries and vulcanises, the filler becomes trapped at the interstitial sites. Since the latex particles present an excluded volume that the nanomaterial does not readily occupy, a percolating network can be formed at very low

loadings. [28, 29, 125, 142]

Emulsion templating draws many similarities with latex blending, although the mechanism of network formation is fundamentally different. Emulsion templating is based on Pickering stabilisation, whereby emulsions of two immiscible liquids can be stabilised by the presence of adsorbed particles energetically trapped at the oil-water interface. [135–139]. This phenomena has been demonstrated with clays, [143, 144] graphene oxide [145] and graphitic multilayers. [146–148]

Latexes are emulsion-polymerised colloids typically stabilised by naturally occurring proteins, polymers or surfactant to facilitate polymerisation during the production process. [140, 141] Consequently, conductive latex composites can be produced below the percolation threshold exhibited in traditional random networks. However, the poor solubility of graphene in water requires the use of surfactant stabilisers which are known to inhibit sheet conductivity. [58] Although Pickering stabilisation offers a certain degree of freedom in the choice of the polymer-solvent system and enables the use of pristine graphene, finding an appropriate system has proved challenging. In the literature, emulsions are mostly formed using poorly-exfoliated graphite [146–149] with few demonstrations of emulsions stabilised by few-layer material. [150]

2.3.3 Electrical Properties

The electrical properties of nanocomposites are generally classified in terms of their percolation threshold, ultimate conductivity and the constants associated with them. A wide range of results taken from a recent review [13] are plotted in Figure 2.3 and grouped by filler type and production method. Broadly speaking, pristine GNP composites can achieve high ultimate conductivities, with multiple examples between 10-1000 S m^{-1}. Further, their high aspect ratios enable percolation thresholds at and below 0.1 vol.% It should be noted however that there is still significant scatter among the filler types and indeed,

categorising electrical performance by the production method reveals similar scatter, likely because the generalised method does not capture the diversity of individual realisations. Perhaps the only immediate conclusion that can be drawn is that solvent-assisted dispersion via solution blending generally leads to higher ultimate conductivities than melt mixing.

Let us consider some specific examples. Boland *et al.* [41] begin by exfoliating pristine graphite in NMP, before redispersing into chloroform following a centrifugation and vacuum filtration step. [151] They then add a boric acid cross-linking agent to a low molecular weight silicone oil to create a viscoelastic putty, which is then dissolved in the graphene-chloroform dispersion. The chloroform is evaporated off and cured resulting in a composite with an isotropic, homogeneous and randomly orientated graphene network. The author's achieve a percolation threshold of 1.75 vol.%, measuring 2×10^{-10} S m^{-1} at 4.5 vol.% and an ultimate conductivity of 0.1 S m^{-1} at 15.75 vol.%.

In a similar example, Yang *et al*, [52] dispersed pre-exfoliated graphene oxide (1.84 wt% oxygen) with less than 3 layers in tetrahydrofuran (THF) via ultrasonication. This was then stirred into a solution of high molecular weight polysilicone dissolved and sonicated to promote even dispersion. This GO-silicone blend is then dropcast into an anhydrous ethanol solution to flocculate the GO and silicone. The ethanol supernatant is removed and a vulcanising agent is added to the composite before curing, reducing the graphene oxide. The authors achieve a percolation threshold of 0.94 vol.% and an ultimate conductivity of 50 S m^{-1}. The relative improvement to Boland *et al.*, is attributed to the higher aspect ratio of the rGO sheets (<3 layers compared to 20 $\pm$ 4 layers).

In other polymer systems, there is typically a significant improvement in electrical conductivity when forming a segregated network. To better understand the data, It is instructive to consider the specific production method. For the lowest percolation threshold measured (0.03 vol.%) - Wu *et al.* produced ultra-high-molecular-weight polyethylene (UHMWPE) composites by blending UHMWPE powders with graphene oxide suspended

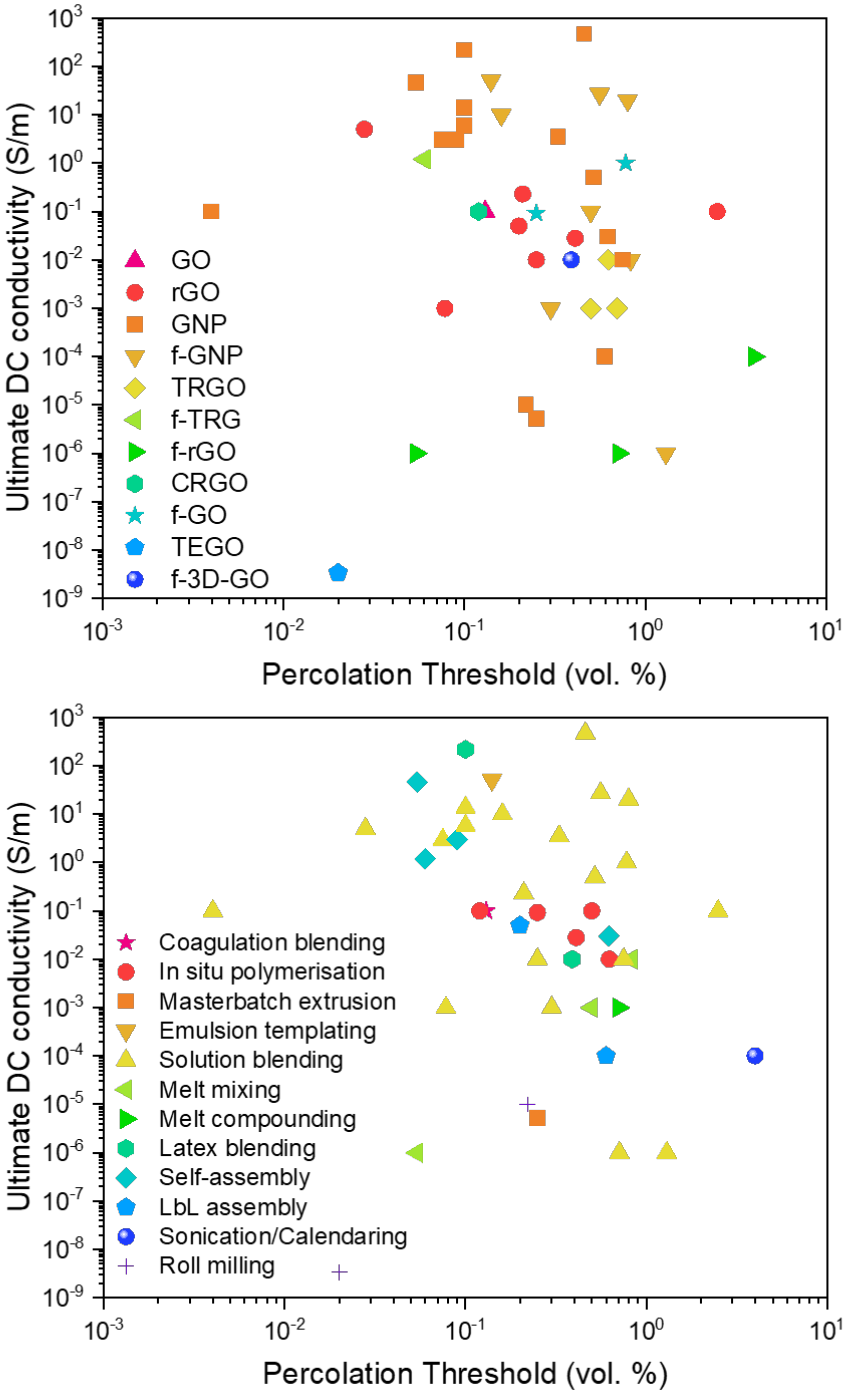

Figure 2.3: **Literature survey of percolation threshold and ultimate conductivity organised by filler material (top) and processing method (bottom) for a range of nanocomposites found in the literature.** [13]

in a water/ethanol solution. The solvent is evaporated leaving GO coated powders, which are then reduced in hydrazine before being compression moulded and hot-pressed into composite sheets. The net result is a segregated network of reduced graphene oxide since the GO adsorbs onto UHMWPE particles that do not dissolve, resulting in the ultra low percolation threshold. Similar results were reported by Pang *et al.* [152]

Qi *et al.* [153] prepared three different types of polystyrene (PS) composites using CNTs, rGO and polylactic acid (PLA) via using a dimethylformamide cosolvent to dissolve and disperse the respective polymers and nanomaterials before compression molding. Polystyrene composites made with graphene achieved ultimate conductivities of 3.49 S m^{-1}, roughly two orders of magnitude higher than the CNT composites at ∼2 % loading. The percolation threshold is significantly lower for the rGO composite, at 0.33 vol.% compared to 0.50 vol.%. Although carbon nanotubes may have a higher length-diameter aspect ratio, sheet-like materials percolate at lower loadings owing to their higher dimensionality and specific surface area, increasing the probability of connection. The authors were able to further reduce the percolation threshold of the rGO composite by blending PLA with the rGO-PS solution. The chemical dissimilarity between the polar PLA and the rGO-PS solution leads to selective localisation of the PLA from which the rGO is excluded. This reduces the percolation threshold by a factor of 4.5 to 0.075 vol.% with a similar ultimate conductivity at half the loading level.

As a final example, we consider the work of Woltornist *et al.*, who use graphite stabilised water-in-oil emulsions to create templated graphite foams. [147, 148] In one example, they blended a low surface tension oil phase consisting of styrene and divinylbenzene with high surface tension DI water and graphite to produce an water in oil emulsion in which the continuous phase is polymerised and eventually cured to form a graphitic foam. These foams have densities below 0.35 g cm^{-3} and bulk conductivities approaching 0.07 S m^{-1}. [147]. Interestingly, the conductivity was further enhanced up to 7 S m^{-1} by infiltrating a second

polymer into the foam void. In another example, they created poly(butyl-acrylate) foams with a percolation threshold below 5 wt.% by graphite mass. [147]

2.3.4 Electromechanical Sensing

Impressive physical properties are purely academic unless without an appropriate application. Nanocomposite strain and pressure sensors have generated enormous interest based on their unparalleled sensitivities and working range. [38, 154, 155] Commercial sensors are currently based on metal foils or capacitors, and have some inherent advantages:- accuracy, reliability and low cost. However, for a sensor to be accurate, there must be efficient stress transfer to the sensor. Soft materials such as skin have a low Young's modulus (100 kPa), such that the relatively high modulus of metals means that the foils would have to be so thin that they would lack durability. Further, the elastic limit of metals is very low, typically less than 5%, [156, 157] ruling out a number of high strain applications.

The conductivity of a material is defined by Equation 2.3;

$$\sigma = Al^{-1}\rho^{-1} \tag{2.3}$$

where A is the cross sectional area, l is the length and ρ is the resistivity. When affine stress is applied, materials will deform according to their Poisson ratio ν and the conductivity changes as a result of their new geometry. Herein lies a major strength of silicone nanocomposites - they are soft enough to deform significantly under small stress, can be made thick enough to infer durability, and have an inherent piezoresistivity which alters the conductivity far beyond that of the changing dimensions. Indeed, piezoresistivity arises due to the change in electron tunnelling distance as the composite is strained and relaxed. As a linear change in tunnelling distance leads to an exponential decrease in tunnelling current, the overall sensitivity can be very high. Indeed, sensitivity to strain is usually

defined in terms of the gauge factor G, (Equation 2.4) [158], where

$$G = 1 + 2\nu + \frac{\Delta\rho/\rho_0}{\Delta l/l_0} \approx \frac{\Delta R/R_0}{\epsilon} \tag{2.4}$$

The $1+2\nu$ accounts for the changing geometry under strain while $(\Delta\rho/\rho_0)/(\Delta l/l_0)$ accounts for the piezoresistivity. For most materials, ν takes values between 0.2-0.5 [159], intrinsically limiting materials without piezoresistive behaviour to a gauge factor G of around 2. Thus, for highly sensitive materials, we can approximate $G \approx \frac{\Delta R/R_0}{\epsilon}$. Whilst compressive strain and applied pressure are related by a material dependent compressive modulus constant, [160] sensitivity to applied pressure is more commonly defined as the change in resistance per unit pressure P, i.e. $\Delta R/R_0 P$ where P is given in kPa. [1, 161–163]

A comparative plot of the various sensors described in the literature is shown in Figure 2.4. Sensitivity ($\Delta R/R_0$) is plotted against the working strain range and colour coded according to linear (blue) and nonlinear (red) responses. It is clear that sensors with high sensitivity and high working strain remain challenging to engineer.

The random graphene-silicone composites produced by Boland *et al.* [41], displayed some interesting piezoresistive behaviour under applied strain. Notably, the composites were extremely sensitive to small deformations, with G = 450 up to 0.5%. However beyond around 1% strain, $(\Delta R/R_0)/\epsilon$ began to decrease, an effect attributed to the viscoelasticity of the material. Such non-monotonic behaviour precludes the use of these sensors as strain gauges above 1%. However, the authors were still able to demonstrate effective pulse monitoring (due to the low strain associated with a dilating carotid artery) and even sense the footsteps of a small spider walking across.

For the random rGO-silicone composites produced by Yang *et al.* [52], G was found to increase close to the percolation threshold, from 30.3 at 2.2 vol.% up to 143 at 1 vol.% while the strain range over which $(\Delta R/R_0)/\epsilon$ was linear decreased from 30% to just 4%. More interestingly, the electrical response over the entire strain range studied (up to 160%) is exponential, although the authors do not acknowledge this.

Taken together, these results suggest that graphene-silicone sensors have the potential to make excellent strain sensors, with a high sensitivity and high strain range. Since the network structure is so closely related to the resultant electromechanical properties and generally leads to an overall improvement, the investigation of functional composite sensors based on segregated networks of graphene in silicone is warranted.

2.4 Pickering Stabilisation using 2D Materials

Emulsions provide a means to generate structure within liquid systems. In order to build a graphene network on an emulsion template, it is instructive to consider the fundamentals of Pickering stabilisation using 2D materials. When two immiscible liquids are mixed, droplets of one phase will form in the other, creating an emulsion. The miscibility of two phases is determined by their chemical similarity. [123] The droplet-matrix boundary or interface has distinct thermodynamic properties relative to the pure droplet and matrix phases, as it consists of a graduated mixture of the two. The midpoint is demarcated by the Gibbs dividing line (GDL). The surface energy at the GDL, γ can be modelled via the Gibbs-Duhem equation as [181]

$$d\gamma = -SdT + Ad\Gamma + \Sigma n_i d\mu_i \tag{2.5}$$

where S denotes the entropy, T the absolute temperature, A the interfacial area, Γ the surface tension, n_i the number of moles of component i and μ_i the chemical potential of component i. At constant temperature and composition, Equation 2.5 simplifies to

$$\Gamma = \left(\frac{\partial \gamma}{\partial A}\right)_{T,n_i} \tag{2.6}$$

For an interface to be stable, Γ must be positive. [181] Now consider the surface energy of a large, single droplet. It is clear that if this droplet is broken up into multiple smaller droplets, both the surface area and number of possible configurations increase, leading to a rise in the surface energy of the system. It is always energetically favourable for two

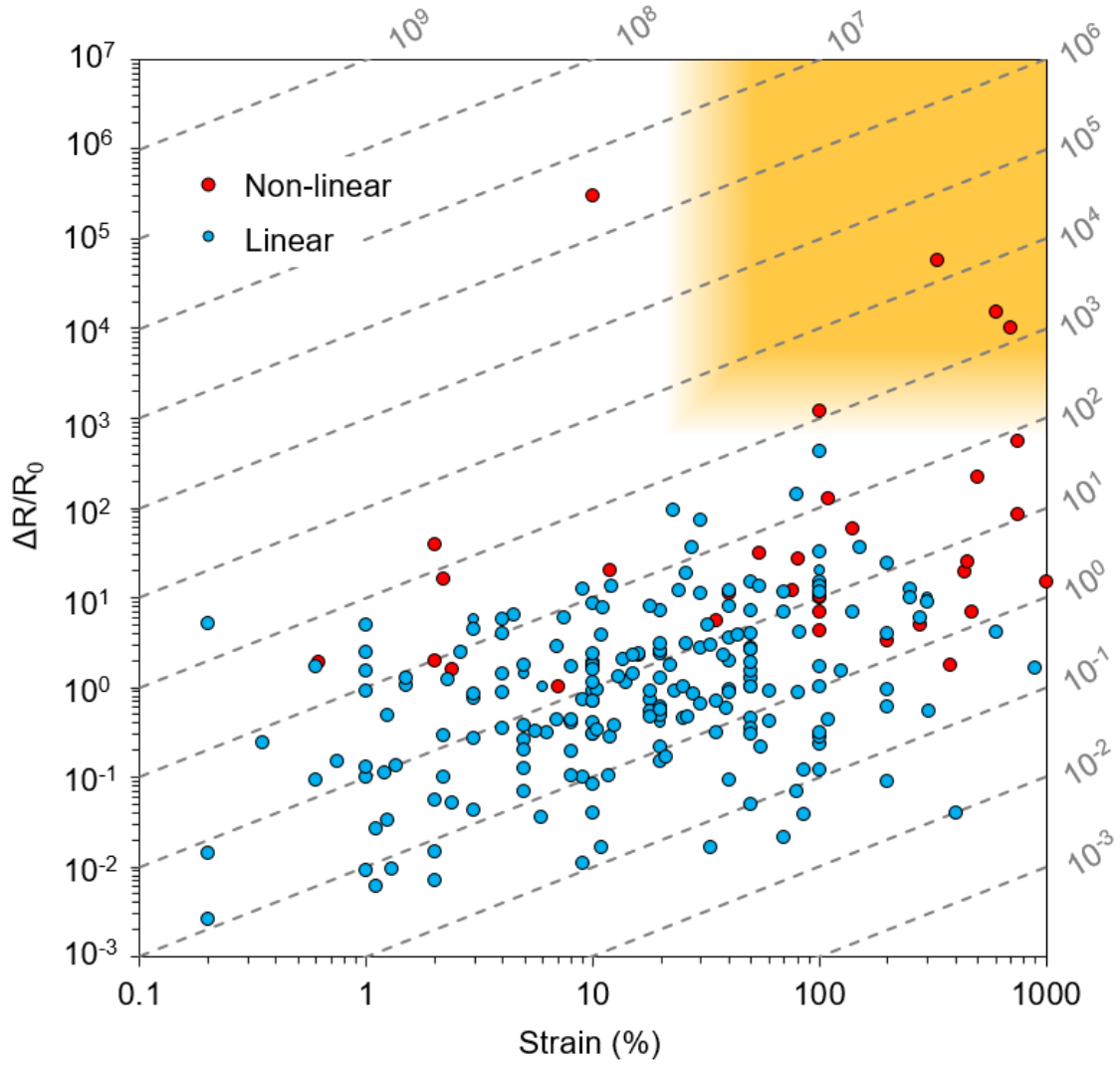

Figure 2.4: **Strain sensitivity $\Delta R/R_0$ *vs* strain, as reported in the literature**. Blue dots indicate the maximum sensitivity and strain range of linear sensors regimes while red dots indicate the maximum sensitivity and strain range of non-linear sensors extracted from over 230 references. [37, 39, 40, 42, 44–51, 53, 55, 56, 111, 124, 155, 164–180] The dashed grey lines correspond to the gauge factor G. The gold region highlights the challenge region of high sensitivity and high strain, defined by relative sensor performance.

smaller droplets to coalesce into a larger droplet should they come into contact. Thus, emulsions only exist in a metastable state.

As the emulsion ages, a number of breakdown processes occur that eventually destabilise the emulsion. These include creaming and sedimentation, flocculation, Ostwald ripening, coalescence and phase inversion. [182]

Creaming and sedimentation occur when the density of the droplet phase is significantly lower or higher than the continuous phase. As the density mismatch increases, the continuous film that separates the droplets becomes thinner as the droplets are confined to a reduced volume, raising the probability of rupture and coalescence.

Flocculation is the aggregation of droplets in which the droplet size remains unchanged, driven by Van der Waals attraction. This increases the probability of coalescence by continuous thin film rupture due to Brownian motion of the individual molecules in each phase. [183]

Ostwald ripening arises due to the non-zero miscibility of one phase within the other, even when the phases are considered immiscible. Smaller droplets are more prone to dispersing into the matrix as they have a higher surface relative to their volume. The dispersed molecules are either absorbed by larger droplets or adsorb onto their surface. The net effect is a larger average droplet size. [184]

Phase inversion may be brought about following a change in temperature or emulsion composition. For example, a sufficient change in temperature may shift the relative surface energies of the phases enough to cause the orientation of the emulsion to reverse. Alternatively, increasing the droplet phase volume above a critical threshold may cause catastrophic phase inversion. [185] Similarly, changing the composition of the phases and hence their relative surface energies may lead to phase inversion.

The diversity of these processes mean that one or more strategies may need to be employed to ensure the stability of the emulsion. The motivation for introducing a

stabiliser at the interface is to create an energetic barrier that prevents adjacent droplets from coalescing. These can be electrostatic and/or steric in nature, that is, through the repulsion of similarly charged particles or from the physical prevention of close contact through the presence of adsorbed particles. The latter is the fundamental operating principle of Pickering emulsions. [137, 186–188]

To form an emulsion, a blend of suitably immiscible solvents must be found. Non-polar solvents typically have the low surface tension Γ_o associated with oil, while polar solvents have the relatively high surface tension associated with water, Γ_w. If the surface tension mismatch is suitably large, the solvents will be immiscible. The surface energies of liquids can be related to the directly measurable surface tensions by the surface entropy via equation 4.1 [189]; $\gamma_s = \Gamma + TS$, where for liquids at 300 K, $TS = 29$ mN m^{-1}. This is particularly useful for making comparisons between solid and liquid phases as surface tension is not defined for solids.

Both the stability and orientation of Pickering emulsions are determined by spreading coefficients, which are defined by the interfacial energies between oil, solid and water phases at the oil-water boundary. The spreading coefficients for the solid-oil and solid-water are given by

$$S_{so} = \gamma_{so} - \gamma_{sw} - \gamma_{ow} \tag{2.7}$$

$$S_{sw} = \gamma_{sw} - \gamma_{so} - \gamma_{ow} \tag{2.8}$$

Where γ_{so}, γ_{sw} and γ_{ow} are the interfacial energies at the solid-oil, solid-water and oil-water interfaces. If S_{so} and S_{sw} carry the same sign, the Pickering emulsion will be stable, while their relative magnitudes dictate the resulting orientation - oil-in-water (o/w) or water-in-oil (w/o). [150] However, with no currently accepted way to determine the interfacial energy of solids, a more complete description of emulsion formation, orientation and stability is needed to better exploit the benefits of emulsion templating. This topic is explored in Chapter 4.

Chapter 3

Characterisation Techniques

3.1 UV-visible Extinction Spectroscopy

Ultraviolet-visible spectrometry probes the electronic transitions in atoms and molecules using light of a given wavelength that is absorbed and/or scattered by the analyte. The resulting extinction spectra can be used to fingerprint the analyte, based on which wavelengths are able to excite electrons to higher energy states and those that are prone to scattering. In a typical UV-visible spectrometer, visible light from a tungsten lamp and UV light from a deuterium lamp are passed through a diffraction grating to split the light into its constituent wavelengths in sequence. The monochromatic light is split again and passed through two samples, where one serves as a reference, before hitting a detector. The intensity ratio between the reference and test sample is then measured, as schematised in Figure 3.1.

For light of wavelength λ or wavenumber $\tilde{\nu}$ to excite an electron from the electronic state E_1 to E_2, we must have

$$\Delta E = E_1 - E_2 = hc\tilde{\nu} \tag{3.1}$$

In the dilute limit, the intensity of absorbed or transmitted light is determined by the

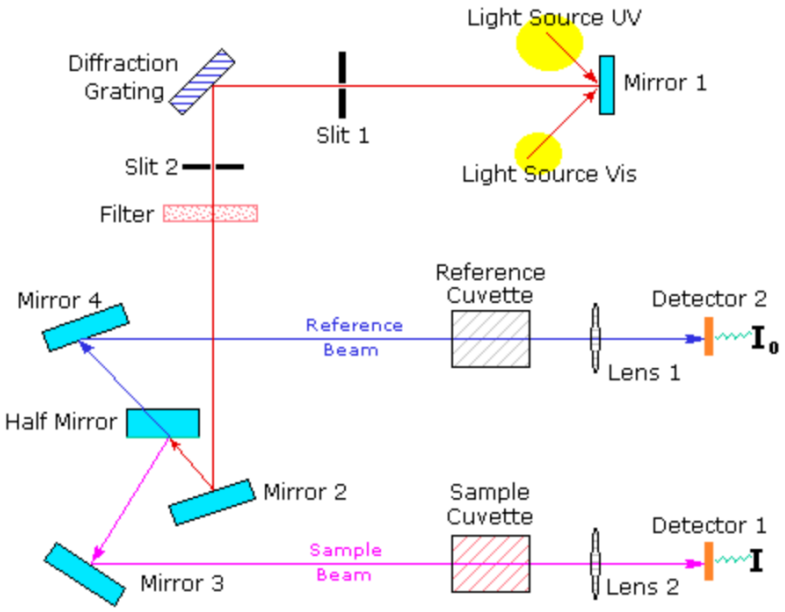

Figure 3.1: **Schematic diagram of a typical UV-visible extinction spectroscopy experiment**. A test sample is irradiated with monochromatic light at a range of wavelengths before the intensity of the transmitted beam is compared against a reference sample.

Bouguer-Beer-Lambert law, where

$$\ln\left(\frac{I_0}{I}\right)_{\tilde{\nu}} = \ln\left(\frac{100}{T(\%)}\right)_{\tilde{\nu}} \equiv A_{\tilde{\nu}} = \epsilon_{\tilde{\nu}} cl. \tag{3.2}$$

Here, I_0 is the light intensity from the reference sample and I the test sample, $A_{\tilde{\nu}}$ is the absorbance, $T_{\tilde{\nu}}$ is the transmittance (in %), $\epsilon_{\tilde{\nu}}$ is the extinction coefficient and l is the path length through each sample in cm.

The extinction coefficient $\epsilon_{\tilde{\nu}}$ is a function of the wavelength and is characteristic of the substance being studied. Because $\epsilon_{\tilde{\nu}}$ can vary by several orders of magnitude over the spectral range, the logarithm is usually taken when mapping the absorption spectra. When $\epsilon_{\tilde{\nu}}$ is known, the concentration of the dispersed substance c_{conc} can be deduced from the associated absorption spectra using

$$c_{conc} = \frac{A_{\tilde{\nu}}}{\epsilon_{\tilde{\nu}} l} \tag{3.3}$$

Although this is the most frequent application of UV-Vis spectroscopy, additional in-

formation on the average layer number $\langle N \rangle$ and sheet length $\langle L \rangle$ may be extracted from the extinction spectra. Indeed, the shape of the absorption spectra is sensitive to the size of nanosheets due to the different electronic behaviour of edges relative to the center. [82, 85, 190]. This makes UV-Vis spectroscopy an invaluable tool for the rapid characterisation of nanosheet dispersions.

3.2 Raman Spectroscopy

Raman spectroscopy is, alongside infrared (IR) spectroscopy, one of the most common vibrational spectroscopic methods for fingerprinting chemical species. It is based on the inelastic scattering of photons from monochromatic excitation sources such as lasers. Typically, the associated energy shift following scattering will form a spectrum between 200-4000 cm^{-1}, with features corresponding to vibrational modes of the materials studied. Raman spectroscopy and IR spectroscopy are complementary methods as some vibrational modes will only be visible using one of these techniques, according to the so-called selection rules. In practice, samples require very little if any preparation, and can be imaged in ambient conditions. Difficulties such as fluorescence may arise in resonant Raman spectroscopy, although steps can be taken to mitigate such effects.

Raman scattering arises due to the interaction between the electric field of an incident photon and the molecule irradiated. This electric field oscillates with initial frequency v_i according to

$$E(t) = E_0 \sin(2\pi v_i t) \tag{3.4}$$

where E_0 is the amplitude. This interaction induces in a molecular electric dipole p on collision, such that

$$\vec{p} = \alpha \vec{E}. \tag{3.5}$$

The induced dipole is proportional to the molecular polarisability α, or the tendency of the electron cloud to distort in an electric field. The polarisation causes a nuclear displacement q of the form

$$q(t) = q_0 \sin(2\pi v_R t) \tag{3.6}$$

where v_R is the vibrational frequency of the molecule. For small oscillations, we may Taylor expand α, yielding

$$\alpha = \alpha_0 + \left(\frac{\partial \alpha}{\partial q}\right)_0 q_0 + \dots \tag{3.7}$$

Substituting (3.5) and (3.8) into (3.6) and simplifying via a trigonometric identity gives

$$\begin{aligned} \vec{p} &= \alpha \vec{E} \\ &= \alpha_0 E_0 \sin(2\pi v_i t) + \frac{1}{2} E_0 q_0 \left(\frac{\partial \alpha}{\partial q}\right)_0 (\cos 2\pi(v - v_R)t - \cos 2\pi(v + v_R)t) \end{aligned} \tag{3.8}$$

The first term corresponds to the elastic Rayleigh scattering, while the second term corresponds to the Raman shift if the photon gains or loses energy when scattered. For a molecule to be Raman active, we require

$$\frac{\partial \alpha}{\partial q} \neq 0. \tag{3.9}$$

Red-shifted photons with lower energy appear as so-called Stokes-Raman lines in Raman spectra, while blue-shifted photons appear as anti-Stokes-Raman lines at an equal but opposite wave-number shift as depicted in Figure 3.2. Since energy levels are populated according to a Boltzmann distribution, the number density of molecules n in a given energy state E is given by $n \propto \exp(-E/k_B T)$, significantly reducing the probability for a photon to be blue-shifted.

Raman spectroscopy has been shown to be particularly useful for the characterisation of layered materials, providing information on the crystal structure, layer number, flake length and presence of defects in particular. [85] [82] [191] The G (1580 cm^{-1}), D (1350 cm^{-1}) and 2D (2960 cm^{-1}) bands (531 nm laser excitation wavelength) are associated with the in plane vibrations of the carbon atoms in a crystal lattice, where the D band and

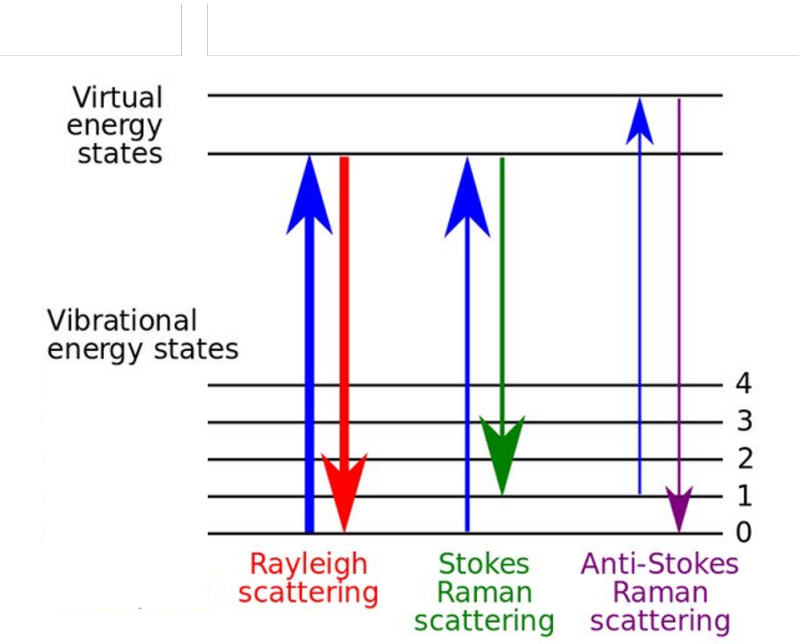

Figure 3.2: **Light scattering processes visualised in terms of energy level transitions**, showing elastic Rayleigh scattering *vs* inelastic Stokes and Anti-stokes scattering. Reproduced from the Wikimedia Commons.

it's 2D overtone appear in the presence of basal and edge defects. The relative intensity of the D and G bands, I_D/I_G varies with nanosheet length, since edge defects directly contribute to the D band intensity in the absence of basal plane defects [192]. Backes *et al* [85]. showed that the average nanosheet length for graphene in a nanosheet ensemble could be estimated to within ~20% error using

$$\langle L \rangle = \frac{0.094}{(I_D/I_G)_{graphene} - (I_D/I_G)_{graphite}} \tag{3.10}$$

where $\langle L \rangle$ is given in µm and $(I_D/I_G)_{graphite}$ takes a value of 0.05. Similarly, the average sheet thickness in number of atomic layers is described to within 25% by

$$\langle N \rangle = 1.04 \left(\frac{I_{2D}}{I_G} \right)^{-2.32} \tag{3.11}$$

Resonant Raman is a particularly useful variant where very small concentrations of the material studied can be detected by matching the excitation frequency of the laser with the energy difference between the ground state and an excited electronic state. Polarised

Raman is also useful for probing anisotropies in the material. When the electric field of the exciting photon is perpendicular to the crystal axis, the Raman intensity may be suppressed. Comparing the signal intensity at various polarisations allows the spectroscopist to determine the predominant crystal axis orientations in the sample.

3.3 Atomic Force Microscopy

Atomic force microscopy (AFM) is a powerful technique primarily used to probe the structure of materials on a sub-nanometre scale. A sample is placed on a stage that is able to move very precisely in the x, y and z planes using piezoelectric transducers (PZT), before being brought into close proximity to a sharp tip at the end of a cantilever. A number of short and long range forces act between the tip and sample, causing the cantilever to deflect away from the sample according to Hooke's law. A laser is reflected off of the cantilever and onto a 4-quadrant photodiode, enabling the deflection of the cantilever to be measured. The position of the cantilever is fed back to the stage and the stage moves accordingly. This is schematised in Figure 3.3.

In contact mode, the tip rasters across the surface at such a distance that the force experienced by the tip is repulsive. The height of the stage is adjusted to maintain either a constant height or constant force between the tip and sample. This induces relatively large lateral forces between the tip and sample, meaning hard samples must be used in this mode to prevent damage to the sample or contamination of the tip. In ambient conditions, a fine layer of moisture forms which subject the tip and sample to additional capillary forces and therefore noise.

In tapping mode, the cantilever is driven to oscillate at or close to it's resonance frequency, contacting the sample with every cycle. The tip-sample interaction causes a shift (usually a decrease) in the oscillation frequency as the local forces increase with decreasing distance to the sample. This frequency is fed back into the PZT and the height of the

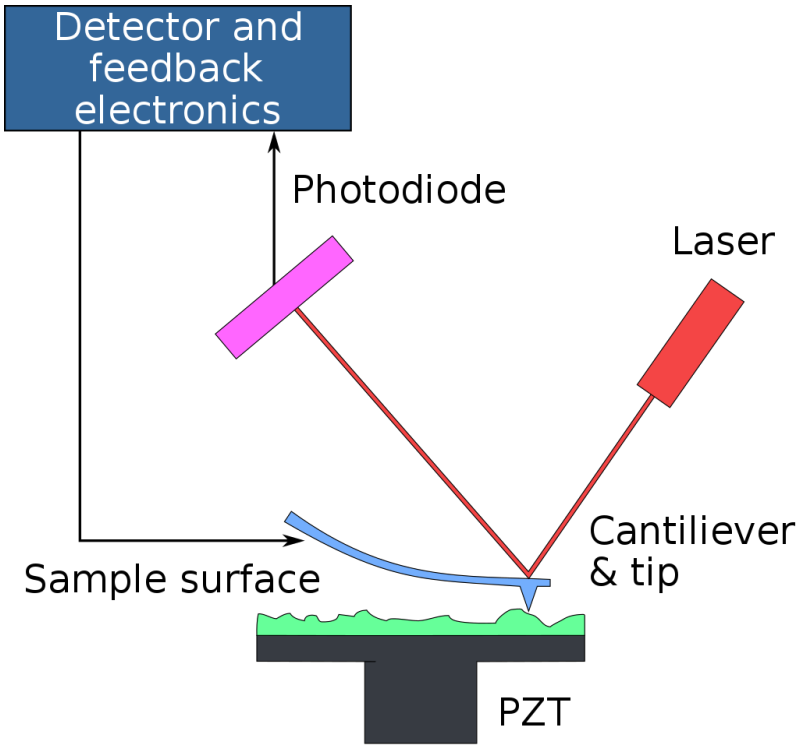

Figure 3.3: Schematic diagram of an atomic force microscope. A Laser is reflected off of a cantilever that deflects according to the sample surface geometry onto a photo-diode. The position of the laser spot on the detector is converted into spatial coordinates for the tip to generate a topological map of the sample surface. Reproduced from the Wikimedia Commons.

probe is adjusted throughout scanning to maintain the driving frequency and amplitude. This significantly reduces the lateral forces acting on the tip, enabling soft polymers or delicate samples to be imaged even in ambient conditions.

AFM has featured heavily in the characterisation of 2D materials as its high resolution is ideal for accurately measuring important nanosheet properties such as flake length and layer number. [82] [83] [84] [59] [85] Typically, a nanosheet dispersion is drop-cast or spin-coated onto pre-heated silicon before multiple sites on the sample are measured. Individual flakes are mapped and a statistical analysis is performed to obtain $\langle L \rangle$ and $\langle N \rangle$. For LPE graphene the apparent interlayer separation is typically on the order of 1 nm due to the intercalation of solvents and/or surfactant used in the exfoliation process.

Although AFM has proved undoubtedly useful in the characterisation of nanomaterials, obtaining accurate topographies is technically challenging. At the nano-scale, Van der Waals, electrostatic, capillary and double layer are just some of the forces that have to be considered to obtain the atomic scale resolution. The accuracy of the height measurement depends on the estimation of resultant force acting on the tip F and cantilever stiffness k, according to $F = kz$. While no magic-bullet model exists to account for the various interactions at play, imaging in different modes and/or simplifying the environment can help to separate signal from noise. While AFM is one of the few microscopies that can quantify height variation in the sample, the apparent width of a feature is determined largely by the tip radius, which can range from a few to tens of nanometres. Tips are prone to damage in contact mode, and are expensive to replace. Further, the typical scan size is on the order of a few hundred microns in length by microns in depth. As such, only relatively small and smooth surfaces can be imaged in a reasonable time frame.

3.4 Dynamic Light Scattering

Dynamic light scattering (DLS) measures the Brownian motion of particles suspended in solution. The rate of diffusion is related to the size of the particle, with larger particles diffusing more slowly through the solution due to viscous drag. The rate of Brownian motion can be quantified using the translational diffusion coefficient, D, while the hydrodynamic size of a particle is defined as the size of a sphere that diffuses at the same rate as the particle being measured. This sphere includes the core particle and anything bound to it's surface, e.g. adsorbed surfactant. Laser light shone into the dispersion will be absorbed and re-emitted by the suspended particles or Rayleigh scattered. The intensity of the scattered light is picked up be a nearby detector and analysed over time. The intensity fluctuates due to the Brownian motion of the particles, while the derivative increases with additional motion. Thus, smaller particles will see more rapid changes in the light intensity as a function of time.

Snapshots of the time-dependent intensity fluctuations are taken and compared against the initial measurement. The correlation between the initial measurement and each new snapshot is quantified using a correlation coefficient, a process known as autocorrelation. The auto-correlation function that describes the decay of the correlation coefficient depends on the size of the particles and can be used to measure the translational diffusion coefficient D. D is substituted into the Stokes-Einstein equation

$$d_h = \frac{kT}{3\pi\eta D} \tag{3.12}$$

where d_h is the hydrodynamic diameter of the particle and η is the viscosity of the medium. The distribution of particle sizes is referred to as the intensity particle size distribution (PSD), with the technique sensitive to particles in a sub-nanometer to several micron range - typical of nanosheets produced via liquid phase exfoliation.

Because the hydrodynamic size is based on spherical particles, care must be taken

with drawing direct conclusions on the size of dispersed nanosheets based on the PSD alone. [193] Although models exist for the hydrodynamic size of rods and discs [194], they are relatively cumbersome. Lotya *et al.* [193] present a more pragmatic approach in which the most intense hydrodynamic size αDLS is correlated with TEM data for a range of nanomaterials, including graphene, MoS_2 and WS_2. They show that α_{DLS} can be related to the average length of the sheets $\langle L \rangle$ by a power law, namely

$$\langle L \rangle = (0.07 \pm 0.03)\alpha_{DLS}^{1.5\pm0.5} \tag{3.13}$$

Although the authors acknowledge that there is a significant uncertainty of 40% in this method, the speed and facile nature with which $\langle L \rangle$ can be acquired makes it a valuable technique for rapid flake size estimation.

3.5 Scanning Electron Microscopy

In optical microscopy, the ultimate resolution is governed the diffraction limit, in which the minimum resolvable distance is $d = \frac{\lambda}{2n \sin\theta}$ where n is the refractive index of the medium and θ is the angular resolution. Therefore, the minimum feature size that can be resolved is predominantly determined by the wavelength of visible light (400-700 nm). The principal advantage to electron microscopy over optical microscopy is the range of accessible electron wavelengths, where the wavelength of an electron is given by the de Broglie equation $\lambda = \frac{h}{mv}$. Commercial scanning electron microscopes (SEMs) have typical accelerating voltages of ~1-30 keV, offering a considerable improvement in the ultimate resolution limit.

In most SEMs, electrons are produced via thermionic emission, usually from a tungsten filament. The electrons are subject to an accelerating voltage away from the source, towards one or more electromagnetic lenses used to focus the electron beam into a spot. This spot is then rastered across the sample surface, generating an image pixel by pixel. When the monochromatic electron beam is incident on the sample, many electrons will penetrate

the surface to a region known as the interaction volume. Electrons may interact with the sample in a variety of ways, from primary scattering processes to secondary processes such as auger emission or X-ray emission following induced electronic transitions. As such, a typical SEM features 3 detectors, for back-scattered electrons, secondary electrons and X-rays, as shown in Figure 3.4. Emitted X-rays are useful for characterising the chemical composition of the sample, as the binding energies of electron orbitals for different elements and chemical states are well defined. Secondary electrons provide useful topographical information for the sample as electrons able to reach the detector must be close to the surface, allowing for easy interpretation. Back scattered electrons are high-energy electrons reflected or elastically scattered from deep within the sample. As heavier elements scatter electrons more strongly, different elements will provide additional contrast.

One consequence of using electrons as a probe is the need for conductive samples. If electrons are not able to move freely through the sample, charging occurs and the image may appear very bright or lose focus. Charging can be mitigated by reducing the accelerating voltage or coating the sample with a thin film (nanometers) of sputtered metal (e.g. gold or tantalum). Further, samples are usually imaged in vacuum due to the relatively short mean free path of the electrons, ruling out the use of liquids in normal circumstances.

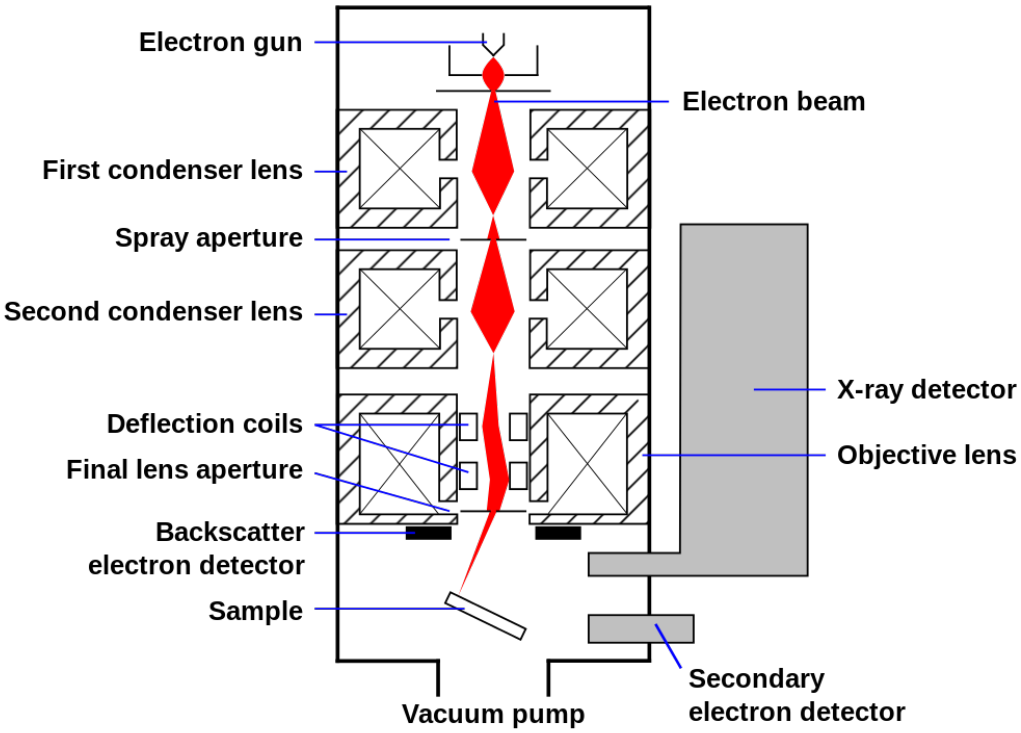

Figure 3.4: **Schematic diagram of a scanning electron microscope.** A beam of electrons is produced via thermionic emission and focused on to the sample using a series of electromagnetic lenses. Scattered electron energies are recorded and converted into topological and chemical information. Reproduced from the Wikimedia Commons.

Chapter 4

Formation of Graphene-Stabilised Emulsion Composites

In this chapter, the formation of polymer emulsions is examined using graphene as a stabiliser. It will be shown how 2D materials are naturally attractive candidates for Pickering emulsification due to their convenient surface energy and high surface area, before exploring the behaviour of polymers in emulsified systems. A process is developed for preparing hierarchically-structured nanocomposites of graphene and PDMS, which has the potential to be extended to a wide range of two-dimensional layered materials and polymer matrices. The method is based on Pickering emulsification, whereby two immiscible liquids are stabilized by solid particulates energetically trapped at their mutual interface. [135–139] Pickering stabilization of liquid-liquid emulsions has been demonstrated with clays, [143, 144] graphene oxide, [145] and graphitic multilayers. [146–148] If either of the two liquid phases contains a polymer or polymer precursors then a solid structure can be produced, with the remaining solvents removed from the structure. [148]

A solvent system that enables the production of high-quality oil-in-water emulsions is identified, in which graphene nanosheets assemble to stabilise PDMS-containing droplets. By modifying the processing conditions, these emulsions can be cured into various morpho-

logies from microspheres to nanocomposite films. The underlying mechanisms of composite formation in the emulsified systems is investigated, and how they relate to the final electromechanical properties is shown. This understanding is used to create highly elastic composites with an embedded templated graphene network.

4.1 Emulsion Orientation Characterisation

When combining two immiscible phases such as oil and water, the simple oil-in-water (o/w) or water-in-oil (w/o) emulsions or even multiple emulsions such as oil-in-water-in-oil and water-in-oil-in-water may be formed. [195] In this thesis, the analysis is limited to simple o/w and w/o emulsions.

To develop a formal understanding of how emulsions form, it is important to be able to accurately characterise the emulsion structure. The simplest method is to exploit the different densities of the droplet and matrix phases. For example, the orientation of an emulsion consisting of ethyl acetate (0.902 g cm^{-3}) and mixtures of DI water and ethylene glycol (1 and 1.113 g cm^{-3} respectively) can be determined by the buoyancy of the droplets. Sedimenting droplets imply that the denser water and EG form the droplet phase w/o, while creaming implies ethyl acetate droplets (o/w).

Other methods of characterisation include the behaviour of the droplets on glass, which has a considerably larger surface energy than liquids. Droplets may burst on contact if the encapsulated phase liquid has a surface tension greater than the continuous phase, i.e. if the emulsion is w/o. Analogously, o/w droplets will burst in contact with low surface energy silanised glass as the surface energy of the oil is often intermediate to the silanised glass and water phase. Finally, food colouring may be solubilised into one of the phases to easily visualise the orientation.

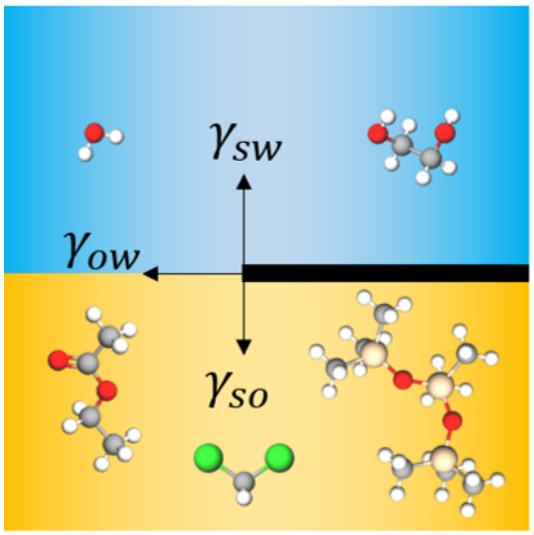

Figure 4.1: **Schematic diagram of an interfacial nanosheet within the present system.** The interfacial energies are labelled at the three-phase boundary.

4.2 Emulsion Orientation Model

Given that a number of orientations are possible, it is important to understand under what conditions a given orientation will form. The forces acting on a nanosheet trapped the oil water interface are schematised in Figure 4.1. The interfacial tension between the oil and water, Γ_{ow} cause the nanosheet to spread across the interface while the relative magnitudes of Γ_{sw} and Γ_{so} determine the orientation of the emulsion as seen in Figure 4.2. However, the interfacial energies are difficult to measure directly, so it is beneficial to re-write this condition in terms of the more readily available surface energies. This is achieved by considering the relationship between the spreading coefficients and constituent interfacial energies. [196] As discussed in Chapter 2, the spreading coefficients for the solid-oil and solid-water are given by

$$S_{so} = \gamma_{so} - \gamma_{sw} - \gamma_{ow} \tag{4.1}$$

$$S_{sw} = \gamma_{sw} - \gamma_{so} - \gamma_{ow} \tag{4.2}$$

Where γ_{so}, γ_{sw} and γ_{ow} are the interfacial energies at the solid-oil, solid-water and oil-water interfaces. The above definitions can be combined to give

$$S_{so} + S_{sw} = -2\gamma_{wo} \tag{4.3}$$

Since interfacial energies are positive, spreading coefficients must have the same sign. A stable emulsion forms if both coefficients are negative, which can only be true if

$$\gamma_{so} - \gamma_{sw} < \gamma_{ow} \tag{4.4}$$

and

$$\gamma_{sw} - \gamma_{so} < \gamma_{ow}. \tag{4.5}$$

Which can be combined to give

$$|\gamma_{so} - \gamma_{sw}| < \gamma_{ow} \tag{4.6}$$

The orientation of the emulsion (o/w or w/o) is determined by which of the oil or water phases wets more readily to the solid phase. I.e, if $S_{so} < S_{sw}$, the water phase more readily and oil droplets form leading to an o/w emulsion. Analogously, if $S_{sw} < S_{so}$ a w/o emulsion forms. It follows that the phase inversion occurs when $S_{sw} = S_{so}$, or equivalently

$$\gamma_{so} = \gamma_{sw}. \tag{4.7}$$

One can approximate the interfacial surface energies using the surface energies of the constituent phases, namely

$$\gamma_{ab} = \gamma_a + \gamma_b - 2\sqrt{\gamma_a \gamma_b}. \tag{4.8}$$

Substituting 4.8 into 4.7 gives

$$\gamma_s + \gamma_o - 2\sqrt{\gamma_s \gamma_o} = \gamma_s + \gamma_w - 2\sqrt{\gamma_s \gamma_w} \tag{4.9}$$

Simplifying and rearranging we have

$$\gamma_o - \gamma_w = 2\sqrt{\gamma_s \gamma_o} - 2\sqrt{\gamma_s \gamma_w} \tag{4.10}$$

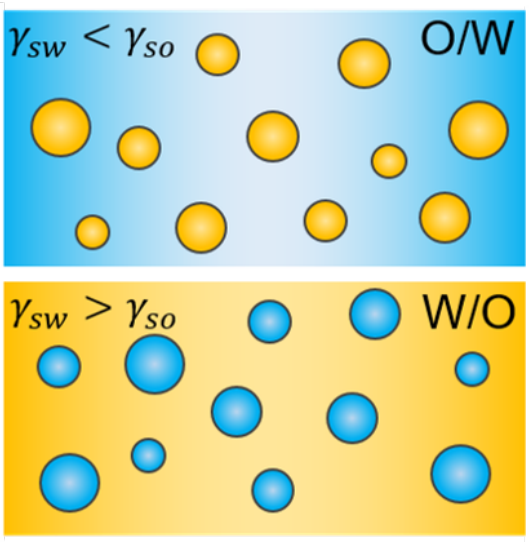

Figure 4.2: **Schematic of oil in water o/w and water in oil w/o emulsions**, where the droplet phase is stabilized by a layer of nanosheets and the relative magnitudes of γ_{sw} and γ_{so} determine the orientation

Substituting $\gamma_o = x^2$ and $\gamma_w = y^2$ gives

$$x^2 - y^2 = 2\sqrt{\gamma_s}x - 2\sqrt{\gamma_s}y \tag{4.11}$$

$$(x + y)(x - y) = 2\sqrt{\gamma_s}(x - y) \tag{4.12}$$

Revealing the phase inversion threshold:

$$\sqrt{\gamma_o} + \sqrt{\gamma_w} = 2\sqrt{\gamma_s}. \tag{4.13}$$

Once the surface energy of the stabiliser is known, suitable solvent systems for a given orientation can be predicted using Equation 4.13.

4.3 Emulsion Formation and Stability

In order for a solid to adsorb onto the droplet-matrix interface, it must have a surface energy γ_s that is intermediate to each phase, such that [196]

$$\gamma_o < \gamma_s < \gamma_w \tag{4.14}$$

For many 2D materials, γ_s is approximately sim70 mN m^{-1}, corresponding to an effective surface tension of 40 mN m^{-1}. [58] As ethylene glycol and deionised water have surface tensions of ∼48 and ∼72 mN m^{-1} respectively, while most organic solvents and polymers have surface tensions in the 20-30 mN m^{-1} range. Thus, many configurations exist for emulsions stabilised by 2D materials. Since the specific surface area of the stabiliser dictates the maximum droplet surface area that can be stabilised, 2D materials naturally lend themselves to emulsification.

The two-phase emulsion system utilized to prepare graphene-PDMS nanocomposites is illustrated in Figure 4.1. A high surface energy 'water' phase consists of water and ethylene glycol (EG), and a low surface energy 'oil' phase that contains dichloromethane (DCM), ethyl acetate (EA) and Qsil 216, a commercially available platinum-cure PDMS elastomer system. The oil phase solvents were identified by adopting a Hansen parameter matching approach with solvents intermediate to graphene and PDMS in Hansen space investigated further. Of these, DCM and EA were selected as they both solvated PDMS and were found to sufficiently disperse a commercially-available graphene powder. In principle, a similar methodology could be applied to other polymers or resins to produce nanocomposites with layered nanomaterials. The water phase consists of deionised (DI) water and EG as this mixture is found to be immiscible with all blends of DCM:EA. Additionally, changing the ratio of DI water:EG tunes the surface energy of the water phase, used to determine the surface energy of the stabiliser by Equation 4.13 and change the emulsion orientation.

The relative surface energies of the oil and water phases (γ_o and γ_w, respectively) and the solid stabiliser (γ_s) dictate the stability of the emulsion. If the condition $\gamma_o < \gamma_s < \gamma_w$ is met, an emulsion may be formed. Since both EG and water have higher surface energies than graphene, and DCM, EA, and PDMS all have lower surface energies, all compositions of the system described in Figure 4.1 form stable emulsions. As discussed, the balance of interfacial energies between the two liquid phases and the stabilizer dictate the orientation

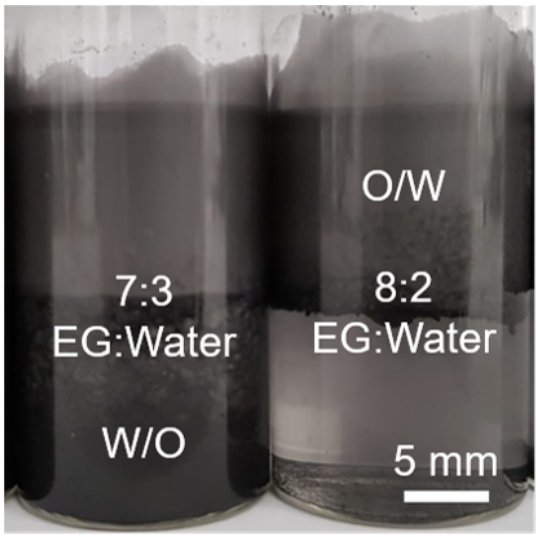

Figure 4.3: **Photograph of o/w and w/o emulsions** where the phase transition was brought about by altering the ratio of EG to water, and therefore γ_w. Scale bar 5mm

of the emulsion, [135, 196] where a water-in-oil w/o emulsion is formed if $\gamma_{so} < \gamma_{sw}$ and an oil-in-water (o/w) emulsion is formed if $\gamma_{so} > \gamma_{sw}$; shown schematically in Figure 4.2 and demonstrated in Figure 4.3. Optical microscopy of a typical w/o emulsion is shown in Figure 4.4, showcasing a network of graphene-stabilised water droplets.

Figure 4.5 plots a phase diagram over the composition of the system in terms of the surface tensions of the water and oil phases, as these are directly measurable. From Equation 4.13, the w/o-to-o/w inversion occurs when the energies of the solid-water and solid-oil interfaces are equal. [196]. It is more convenient to express the interfacial energies in terms of the more readily measurable surface energies of the solid, oil and water phases using a simple approximation such as $\gamma_{ab} = \gamma_a + \gamma_b - 2\sqrt{\gamma_a \gamma_b}$. As previously discussed, the emulsion inversion threshold can then be defined in terms of the three surface energies in the system in the previous section, such that $\sqrt{\gamma_o} + \sqrt{\gamma_w} = 2\sqrt{\gamma_s}$.

A consequence of Equation 4.13 is that the determination of the surface energies of both liquid phases for system compositions either side of the inversion threshold allows for the calculation of the surface energy of the stabiliser. As shown in Figure 4.3, the

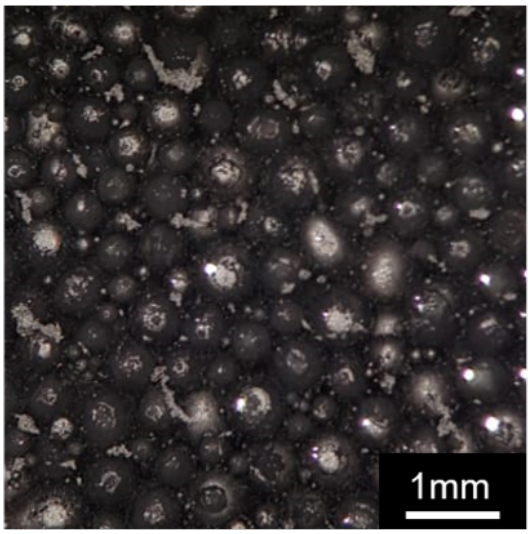

Figure 4.4: **Optical micrograph of a w/o emulsion with 0.44 vol.% graphene relative to the droplet phase.**

phase inversion threshold occurs between 70 vol.% and 80 vol.% EG in the water phase. Utilising the Wilhelmy plate method the surface tensions of EA (Γ_o = 23.3 mN m^{-1}) and DI water:EG mixtures (Γ_w = 52.6 mN m^{-1}) for the 70 vol.% mixture and 51.1 mN m^{-1} for the 80 vol.% mixture were measured. The surface energies of the liquids can be related to the directly measurable surface tensions by the surface entropy; $\gamma = \Gamma + TS$, where for liquids at 300 K TS $\approx$ 29 mN m^{-1}. [189] Two limit values of the graphene surface energy are calculated using Equation 4.13, suggesting that the true value lies in the range 65.5 mN m^{-1} < $\gamma_{graphene}$ < 66.1 mN m-$^{-1}$. This value is somewhat lower than that expected for liquid-exfoliated graphene prepared in solvents such as N-Methyl-2-pyrrolidone (NMP) where the surface energy matching is often taken to imply that $\gamma_{graphene}$ = 71 mN m^{-1}. [121] The measured graphene surface energy is consistent with relatively large, defect free graphene sheets, [121] with potentially some influence of residual surfactant; in agreement with the product specification sheet. Equation 4.13 is plotted as a solid black curve on Figure 4.5 with the defining value of $\gamma_{graphene}$ = 66 mN m^{-1} taken from the above estimate.

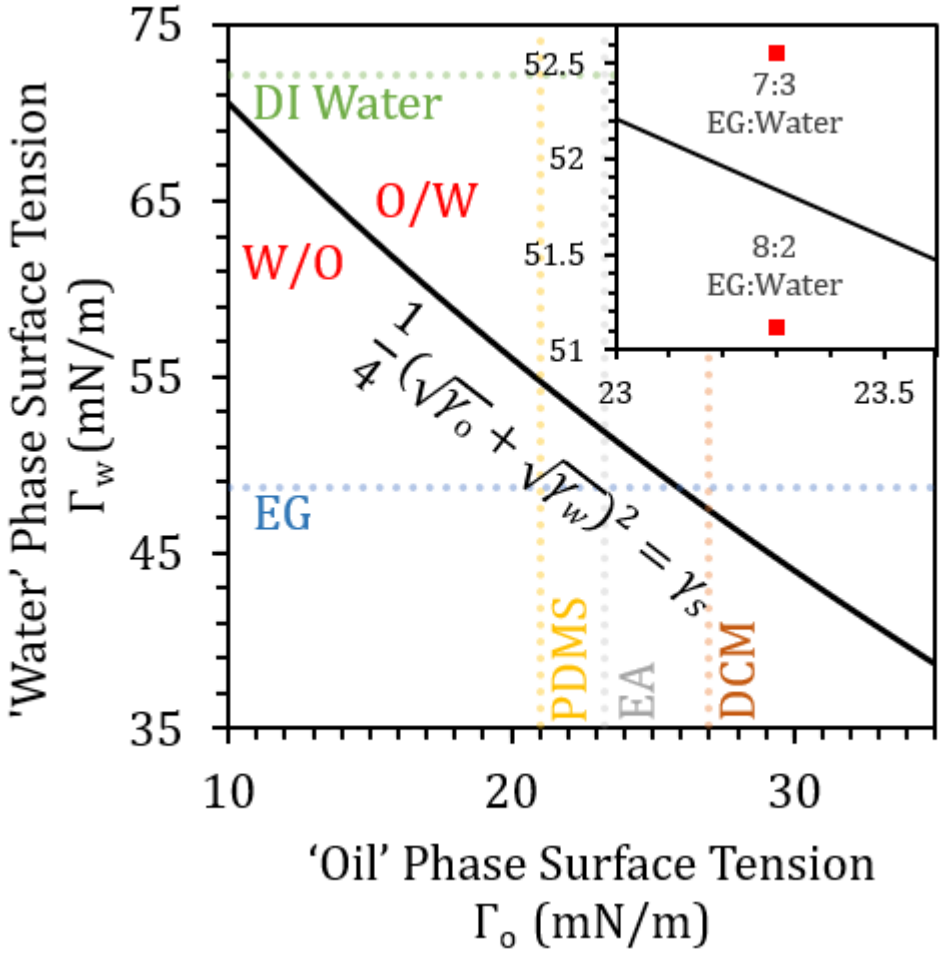

Figure 4.5: **Surface energy phase diagram for graphene stabilised emulsions** highlighting the parameter space for the system, where the phase inversion threshold marked (Equation 4.13) is defined using the surface energy of graphene, $\gamma_s = 66$ mJ m^{-2}. The surface tensions of water, EG, DCM, EA and PDMS are plotted for reference.

4.4 Factors Affecting Droplet Size

The size of a droplet and the thickness of the graphene coating can be estimated by using an intuitive mathematical argument. Assuming monodispersity, the total area of droplets covered by dispersion of nanosheets is

$$A_d = n_d \pi \langle d \rangle^3 \tag{4.15}$$

d where n_d is the total number of droplets and $\langle d \rangle$ is the average droplet diameter. Now consider the active surface area of the nanosheets, one can show that

$$A_{sheets} = V_g / N_{shell} C_{2d} \tag{4.16}$$

Where V_g is the volume of graphene, N_{shell} is the number of graphene layers and C_{2d} is the crystal spacing constant between atomic planes. The total volume of droplets is

$$V_d = \frac{1}{6} n_d \pi \langle d \rangle^3 \tag{4.17}$$

Assuming that all of the nanosheets are bound to the oil/water interface, setting $A_d = A_{sheets}$ gives

$$n_d \pi \langle d \rangle^2 = V_g / N_{shell} C_{2d}, \tag{4.18}$$

leading to

$$(6V_d / \pi \langle d \rangle^3) \cdot (\pi \langle d \rangle^2) = V_g / N_{shell} C_{2d}. \tag{4.19}$$

Simplifying, we have

$$6V_d / \langle d \rangle = V_g / N_{shell} C_{2d} \tag{4.20}$$

which can be rearranged to give

$$V_d / V_g = \langle d \rangle / 6 N_{shell} C_{2d} \tag{4.21}$$

or

$$\phi = 6 N_{shell} C_{2d} / \langle d \rangle. \tag{4.22}$$

Substituting the droplet sizes measured for w/o emulsions shown in Figure 4.6 ($\langle d \rangle$ = 635 μm ... 104 μm) at their respective loading levels (ϕ = 0.0044, ... , 0.044) along with C_{2d} = 1 nm (the effective interlayer spacing observed in liquid exfoliated graphene) and solving for N_{shell} gives $467 < N_{shell} < 901$. In this model, N_{shell} is interpreted as the number of carbon layers (regardless of exfoliation state) spaced C_{2d} times apart to form a shell of thickness S. Then, multiplying N_{shell} by C_{2d} gives an estimate of the average graphene shell thickness, $\langle S \rangle$.

An alternative way to estimate $\langle S \rangle$ is to numerically solve the analytical expression for the shell thickness. The volume of a shell of thickness $\langle S \rangle$ can be expressed as

$$V_s = \frac{\pi}{6}[(\langle S \rangle + \langle d \rangle)^3 - \langle d \rangle^3] \tag{4.23}$$

giving

$$V_s = \frac{\pi}{6}(\langle S \rangle^3 + 2\langle S \rangle^2 \langle d \rangle + 2\langle d \rangle^2) \tag{4.24}$$

Solving for $\langle S \rangle$ gives

$$\langle S \rangle \approx 0.22759U - 0.97639\langle d \rangle^2 / U - 0.66667\langle d \rangle \tag{4.25}$$

Where

$$U = ^3 \sqrt{31.416\langle d \rangle^3 + 5.1962\sqrt{39.478\langle d \rangle^6 + 188.50\langle d \rangle^3 V_s^2} + 81V_s} \tag{4.26}$$

Noting that $V_d/V_s = \phi$, we have

$$V_s = \frac{\pi \langle d \rangle^3}{6\phi} \tag{4.27}$$

Figure 4.7 shows a 3D histogram illustrating how the graphene volume fraction ϕ affects the droplet size distribution and average droplet diameter $\langle d \rangle$ of the emulsions. Since the total surface area available to stabilize the droplets increases with ϕ, a decrease in $\langle d \rangle$ is anticipated as the graphene loading increases; this scaling is clearly visible in the inset

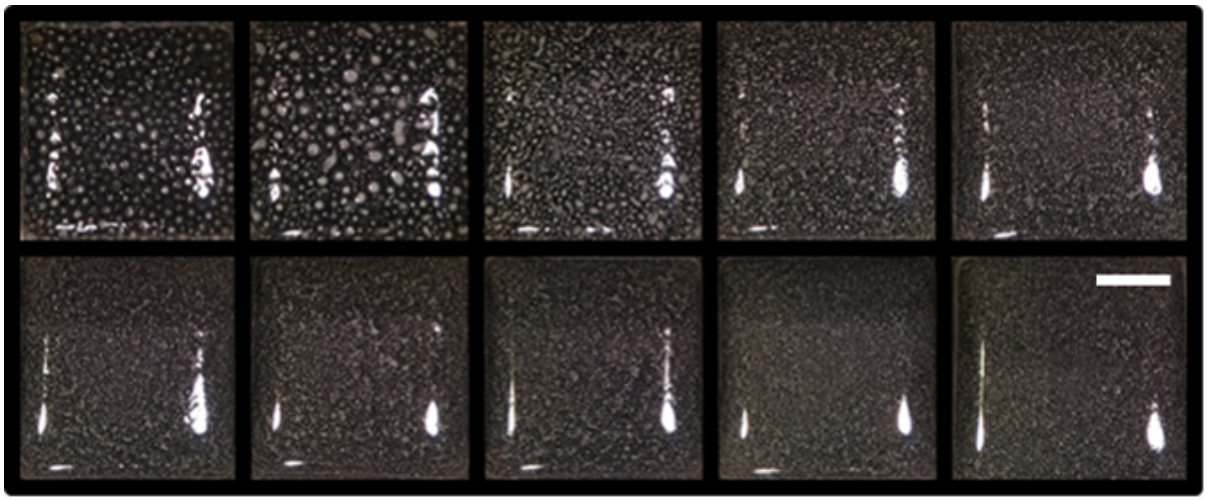

Figure 4.6: **Optical micrographs of graphene stabilised w/o droplets (DI water in ethyl acetate) as a function of loading level**. Left to right, top to bottom, ϕ = 0.44 to 4.4 vol.% graphene in 0.44 vol.% increments relative to the droplet phase. Scale bar = 5 mm.

panel. Assuming uniform droplets, one can derive a relationship between ϕ and the droplet diameter d, namely [197]

$$\phi = 6S/d \tag{4.28}$$

where S is the thickness of the graphene shell. Identifying the droplet diameter d in Equation 4.28 with $\langle d \rangle$ plotted in Figure 4.7, it is clear that the functional form $\langle d \rangle \propto \phi^{-1}$ is compatible with the data. We note that, although the droplet size distribution is clearly not uniform, the similarity between the observed functional form and the predicted functional form for uniform droplets show that this approximation is reasonable to first order.

An exact inverse relationship between $\langle d \rangle$ and ϕ would also suggest that S is constant and no over-coating of the interfaces occurs with additional graphene. However, the data may also be fitted with a general power law of the form $\langle d \rangle \propto \phi^{-0.8}$; this suggests that the shell thickness is not constant but varies with loading level as S $\propto \phi^{0.2}$. This result is interpreted to mean that the degree of over-coating may increase with graphene loading

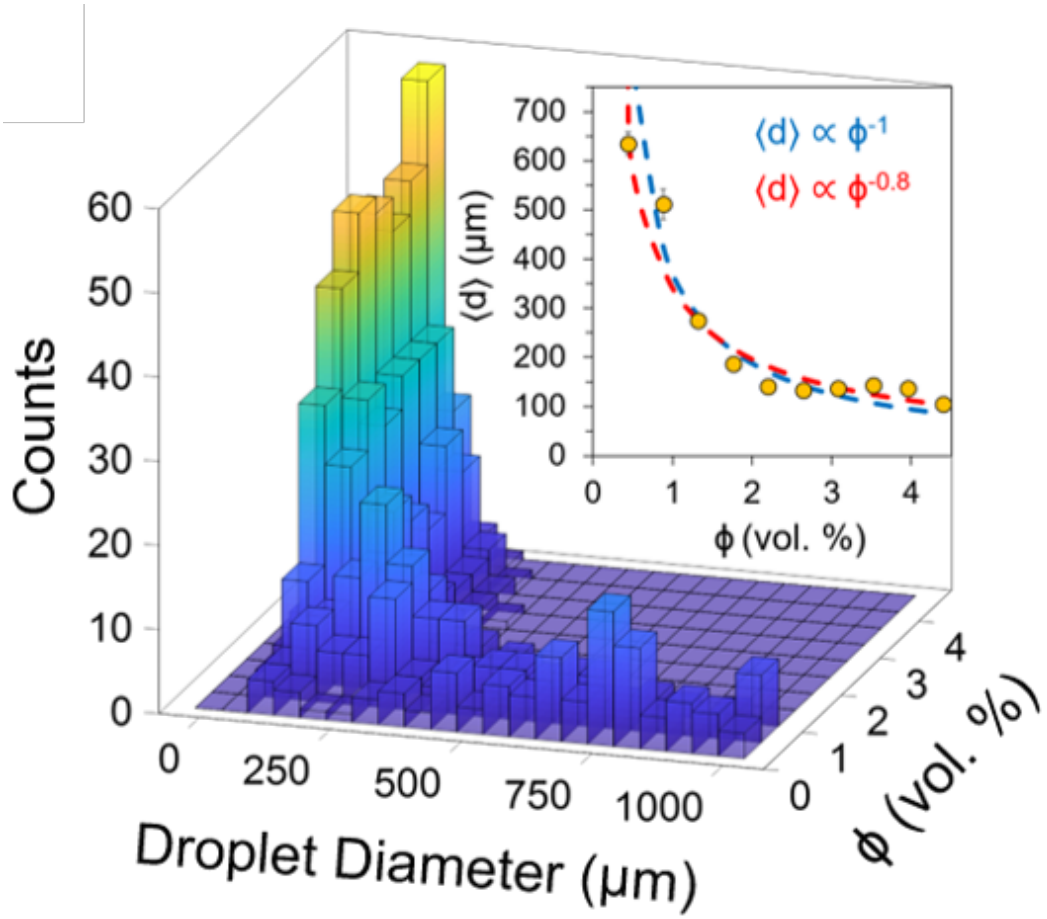

Figure 4.7: **3D histogram of droplet size distributions for w/o emulsions stabilised by ϕ = 0.44 to 4.4 vol.% graphene in 0.44 vol.% increments relative to the droplet phase.** Inset: average droplet diameter $\langle d \rangle$ *vs* ϕ with $\langle d \rangle \propto \phi^{-1}$ plotted in blue and $\langle d \rangle \propto \phi^{-0.8}$ in red.

level.

Measuring $\langle d \rangle$ for a known inclusion of graphene gives us an estimate of the average shell thickness, since from Equation 4.28 $\langle S \rangle = \phi \langle d \rangle / 6$ (provided d and S are treated as independent variables). For the data plotted in Figure 4.7, $\langle S \rangle = 0.7 \pm 0.2$ μm. Equation 4.25 serves as an alternative analytical expression for the shell thickness, yielding a compatible value of $\langle S \rangle = 1.0 \pm 0.3$ μm.

4.5 Polymer Emulsions

In order to form a graphene stabilised polymer emulsion, the polymer-solvent system requires careful consideration. Many properties of the polymer depend on the molecular weight, with high molecular weight polymers generally offering improved toughness and increased chemical resistance at the expense of low melt viscosity and ease of processing. [198] One option is to either increase the energy of mixing to facilitate a more homogenous distribution of graphene, although this is likely to cause further sheet scission and reduce the effective conductivity of the nanosheet network. Instead, as is routine with solution blending, an appropriate solvent could be added to the polymer melt to reduce its overall viscosity and promote even dispersion without impacting the average flake size.

For high molecular weight polymers, two immiscible solvents are required in which one or more is able to disperse graphene and one or more swells the polymer. In order to satisfy Equation 4.13, the high surface tension solvent is essentially limited to ethylene glycol (48 mN m^{-1}), DI water (72 mN m^{-1}) and combinations thereof. In the absence of adsorbed surfactants, graphene cannot be exfoliated or dispersed in these polar solvents. It is then necessary to search for solvents compatible with graphene and polymer. For this, a Hansen parameter matching approach is adopted. [123].

Hansen parameters describe the strength of various interactions relevant at the molecular level; with δ_d, δ_p and δ_h representing the energy from dispersion forces, dipolar

Component	δ_d	δ_p	δ_h	$R_{graphene}$	$R_{backbone}$	$R_{sidechains}$
Graphene	18	9.3	7.7	0	6.8	13.3
PDMS (backbone)	17	4	4	6.19	0	7.3
PDMS (side chains)	14	1	1	13.3	7.3	0
Dichloromethane	18.2	6.3	6.1	3.4	3.9	11.2
Ethyl Acetate	15.8	5.3	7.2	6.0	4.2	8.4
Ethylene Glycol	17	11	26	18.5	23.1	27.6
N-Methyl-2-pyrrolidone	18	12.3	7.2	3.0	9.1	15.2

Table 4.1: Hansen parameters and radii for chemical species. Parameters are taken from ref [123]

intermolecular forces and hydrogen bonds respectively. If two chemical species are close enough in the Hansen space defined by these coordinates, then they are likely to be miscible or soluble. Their interaction distance R_A is the euclidean distance between them with an additional empirical prefactor on the dispersion term, such that

$$R_A = \sqrt{4(\delta_{d1} - \delta_{d2}) + (\delta_{p1} - \delta_{p2}) + (\delta_{h1} - \delta_{h2})} \tag{4.29}$$

The Hansen parameters of relevant chemical species are listed in table 4.1. Due to the high rotational mobility of PDMS, the chemical properties of the O-Si-O backbone and CH_3 methyl groups are considered individually. Interaction distances are calculated for graphene $R_{graphene}$, the PDMS backbone $R_{backbone}$ and sidechains $R_{sidechains}$. From Table 4.1 it is evident that DCM and EA are reasonable solvents for graphene and PDMS owing to the low values of $R_{graphene}$ and $R_{backbone}$. Analogously, ethylene glycol appears to be a much poorer solvent - although it is noted that this could be offset by the presence of residual surfactant. Values for NMP, one of the best graphene solvents [58] are also given for comparison.

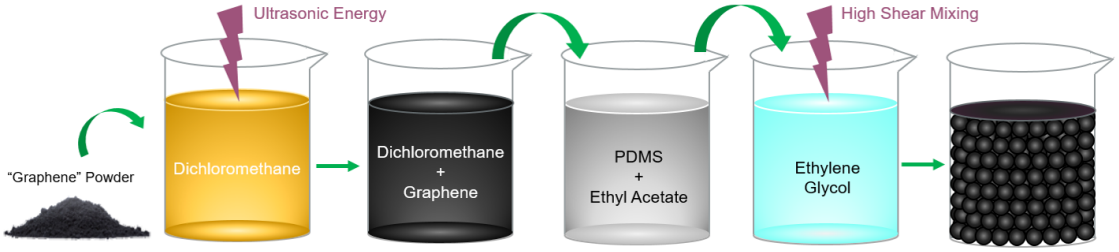

Figure 4.8: **Generalised production method for graphene stabilised oil-in-water droplets**. Graphene powder is added to dichloromethane in the desired quantity and bath sonicated. This dispersion is then mixed with ethyl acetate swelled PDMS to disperse the graphene within the PDMS. This mixture is then combined under high shear with an immiscible water phase, namely ethylene glycol to produce a graphene stabilised emulsion.

Based on the results of the compositional survey undertaken, a 1:1:2 volume mixture of PDMS:EA:DCM was found to strike a balance between PDMS content, sufficiently reducing viscosity to enable effective homogenization, and mitigate density mismatching to minimise instability caused by sedimentation or creaming of droplets. The ratio of 'oil' to 'water' is maintained at 40:60. A generalised production method for graphene stabilised polymer emulsions based on this composition is shown in Figure 4.8. By using a pre-exfoliated graphene powder, a wide variety of loading levels (0.5 - 16.5 vol.%) can be incorporated with relative ease. A photograph of 12 emulsions prepared according to Figure 4.8 at various graphene loading levels is shown in Figure 4.9.

4.6 Graphene-Stabilised Silicone Spheres

Once emulsified, the PDMS-cure system contained within the oil phase can be readily cross-linked through application of heat. This results in graphene-coated PDMS balls or 'G-balls' as depicted in Figure 4.10, once the volatile solvents are removed and the solidified particles are washed. Note the uncoated PDMS spheres adsorbed onto a larger coated droplet via Ostwald ripening that are visibly protected from coalescence via nanosheets

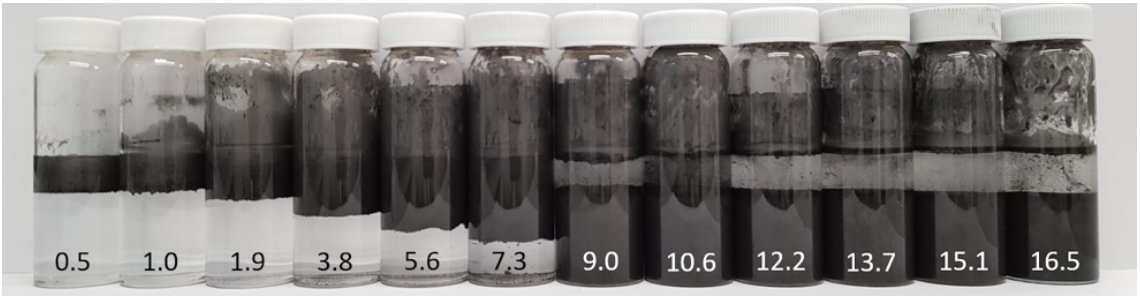

Figure 4.9: **Photograph of the oil-in-water o/w emulsions** prepared according to Figure 5.8. Left to right, 0.5 to 16.5 vol.% graphene with respect to the solids content (PDMS and curing agent). The sedimentation of the droplets is caused by the additional weight of the graphene coating at higher loadings.

trapped between them. While graphene is known to have some degree of flexibility, it is apparent that sub-micron droplets are too small to be coated by graphene sheets. The G-balls may have a variety of uses, e.g. as a filler material for polymers where templating cannot be so readily achieved, or as precursors to other structures. These will be discussed in more detail in chapter 6.

4.7 Time-dependent Morphological Properties

A strong dependence between the morphological properties of the composite and the time the uncured emulsions were allowed to stand at room temperature is observed. This is attributed to the fact that, given sufficient time, polymer chains are likely able to diffuse through the graphene shell and into neighbouring droplets, eventually leading to a macroscopically continuous film shown in Figure 4.12. [199] This transition is evident in the electron micrographs in Figure 4.13 and a schematic of polymer diffusion through a tortuous shell is presented in Figure 4.14. Analogous behaviour is observed in other composite systems, such as the diffusion of graphene sheets into solvated rubber bands [175] or the diffusion of carbon nanotubes into latex spheres. [15]

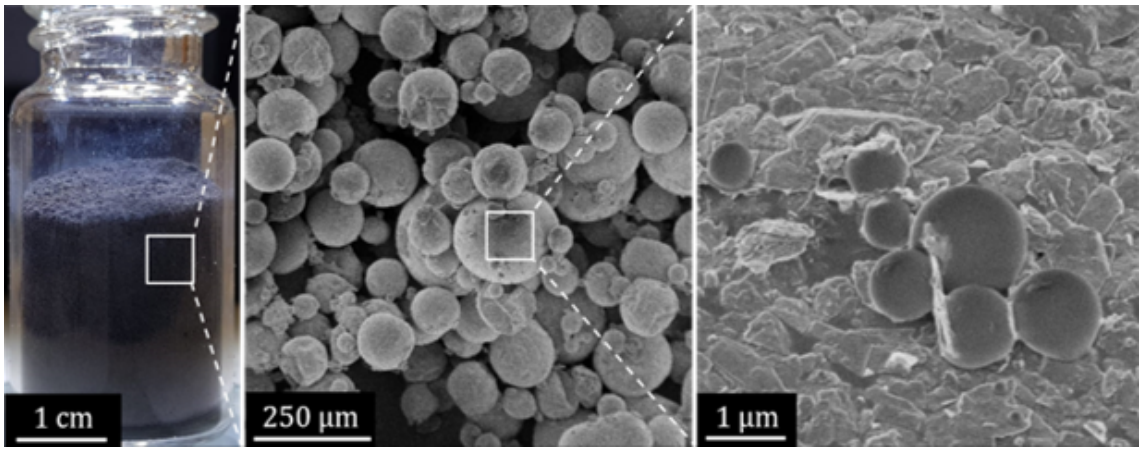

Figure 4.10: **Photograph and SEM of graphene stabilised PDMS droplets cured at 65 °C for 30 minutes immediately after emulsification**. The final panel shows uncoated, sub-micron PDMS droplets on the surface of a ∼200 μm droplet due to Ostwald ripening. Although in contact, their coalescence is prevented by the presence of an individual graphene sheet.

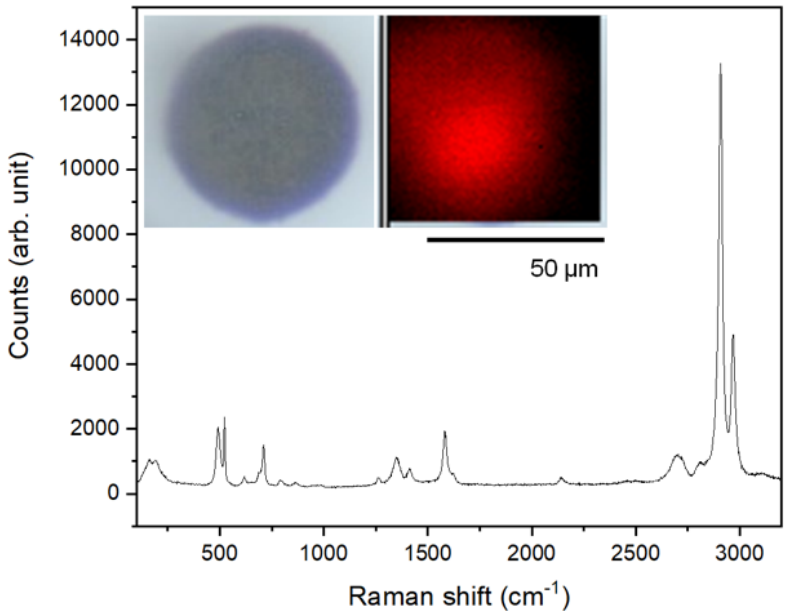

Figure 4.11: **Representative Raman spectra of a graphene stabilised PDMS sphere**. The inset shows a microscope image of the graphene stabilised PDMS sphere studied and corresponding Raman g-peak intensity (1582 cm^{-1}) map in red. Scale bar 50 µm.

Peak position (cm^{-1})	**Peak assignment**
161	PDMS
192	PDMS
491	PDMS (Si - O - Si stretch)
522	Substrate
617	PDMS
710	PDMS (Si-C sym. stretch)
788	PDMS (CH_3 asym. rocking; Si-C asym. stretch)
862	PDMS (CH_3 sym. rocking)
1264	PDMS (CH_3 sym. bending)
1348	Graphene (D peak)
1413	PDMS (CH_3 asym. bending)
1582	Graphene (G peak)
1624	Graphene (D' peak)
2138	PDMS
2720	Graphene (2D peak)
2804	PDMS
2908	PDMS (CH_3 sym. stretch)
2968	PDMS (CH_3 asym. stretch)

Table 4.2: **Peak assignments for representative Raman spectra of graphene-stabilised silicone spheres, as presented in Figure 4.11.**

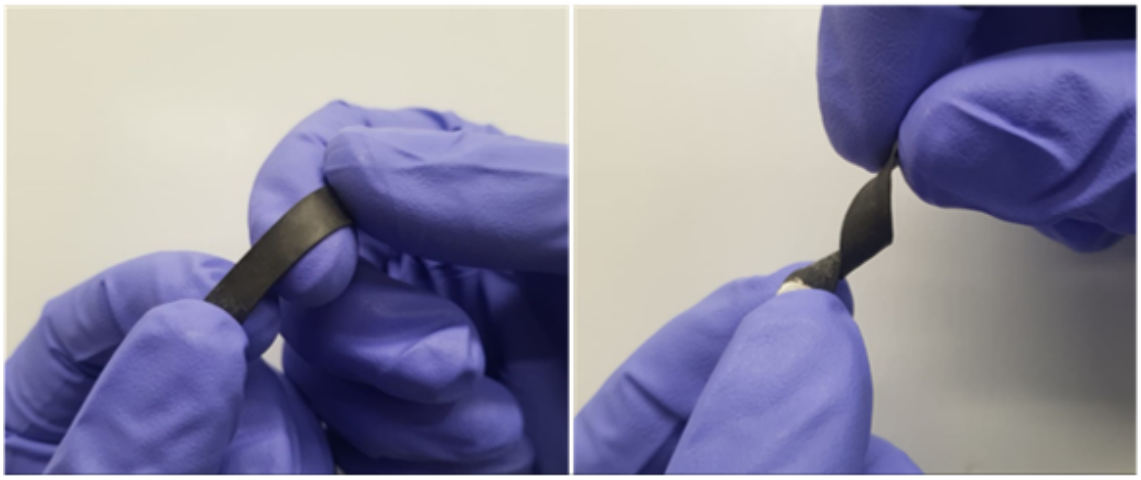

Figure 4.12: **Photographs of an emulsion-based composite film under both strain and torsion**; highlighting the mechanical robustness and flexibility of samples for which the uncured PDMS melt is allowed to interdiffuse for $t_d \approx 2500$ hours prior to curing.

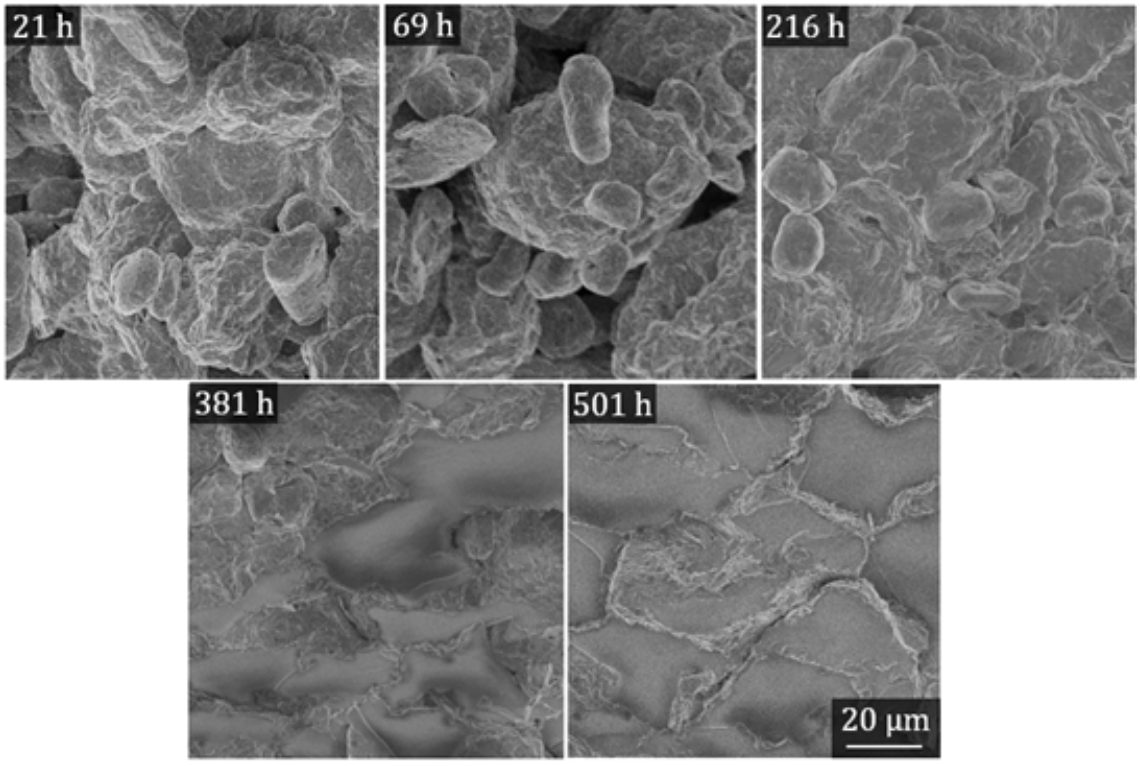

Figure 4.13: **Composite cross-section SEM micrographs *vs* interdiffusion time**; demonstrating a clear transition from discrete balls (21 h to 216 h) to cohesive elastomers (381 h to 501 h) with an embedded, segregated network of graphene nanosheets.

In this scenario, the time taken for PDMS chains to diffuse into the graphene shell depends on the average thickness $\langle S \rangle$, but more so on the tortuosity of the shell structure. For reference, Figure 4.15 illustrates how the average shell thickness may be affected under different droplet-size scaling scenarios. A simple model for the effective diffusivity D of the PDMS chains can be derived as follows. Let S be the vertical distance and/or shell thickness to be traversed. Suppose that N_{shell} sheets, each of height h are stacked in a brick-like fashion, vertically separated from one another by a distance b. Then $S = N_{shell}(h + b) \rightarrow N_{shell} = S/(h + b)$.

The additional distance that must be traversed due to the presence of the sheets is $N_{shell}\frac{1}{2}\rho_{aspect}h$, where ρ_{aspect} is the ratio of the lateral size to thickness of the sheets, such that the total distance becomes

$$x = N_{shell}(h + b + \frac{1}{2}\rho_{aspect}h) \tag{4.30}$$

Substituting $N_{shell} = S/(h + b)$ and simplifying yields

$$x = \frac{S(h(1 + \frac{1}{2}\rho_{aspect}) + b)}{h + b} \tag{4.31}$$

The diffusion coefficient can be expressed as $D = \frac{x^2}{t_d}$, where x is the displacement after a diffusion time t_d has elapsed. Substitution into Equation 4.31 and solving for D reveals

$$D = \frac{\langle S \rangle^2}{\langle t_d \rangle}\left(\frac{(h(1 + \frac{1}{2}\rho_{aspect}) + b)}{h + b}\right)^2. \tag{4.32}$$

The height of each graphene sheet is estimated using the average layer number $\langle N \rangle =$ 6.6 and interlayer spacing, $C_{2d} = 0.34$ nm. The aspect ratio is then the average length of each sheet $\langle L \rangle = 1.1\mu m$ divided by the height, $\rho_{aspect} = \langle L \rangle / \langle N \rangle C_{2d} \approx 500$. The distance between sheets is taken to be b = 1 nm, while for $\phi = 7.4$ vol.%, $\langle S \rangle = 1.2$ µm and $\langle t_d \rangle =$ 250 h based on the shell thickness models and the onset of mechanical robustness. Using

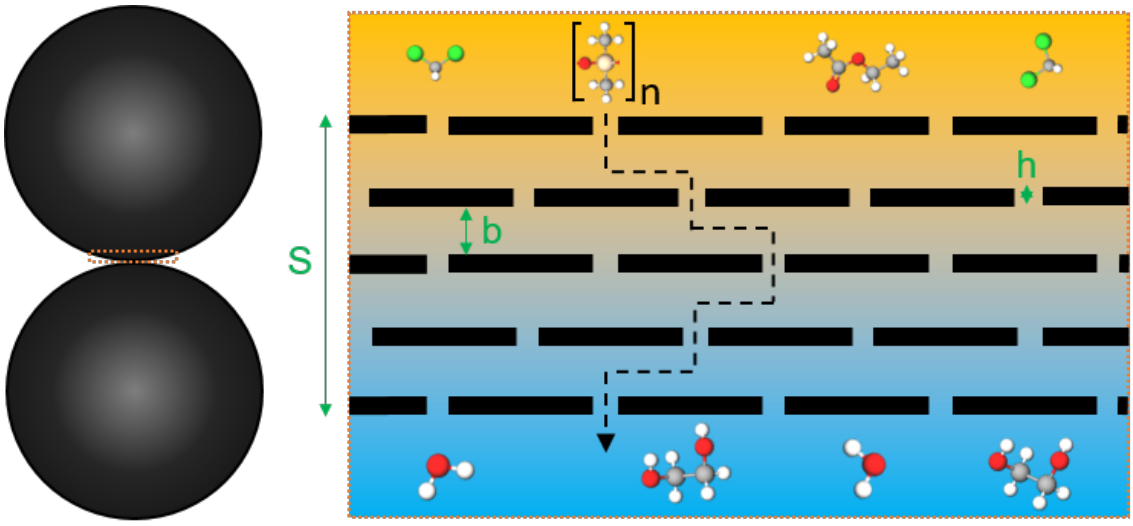

Figure 4.14: **Schematic of polymer chain diffusion through the oil-solid-water interface.** A monomer of PDMS is used in this schematic for clarity. The diffusion path length and interdiffusion time increase as a function of graphene content and nanosheet aspect ratio.

Equation 4.32 it follows that $D = 3 \times 10^{-16} m^2 s^{-1}$. This is 500 times slower than the self-diffusivity of 50,000 g mol^{-1} PDMS chains at room temperature, although unsurprising given the additional distance that must be traversed.

Good agreement between the predicted and measured values of $\langle S \rangle$ is obtained from the SEM of fractured cross-sections in Figure 4.13 with $\langle S \rangle \approx 1.2$ μm. The aspect ratio of the flakes is estimated from the average length of each sheet divided by the average number of layers and the average interlayer spacing for graphite, i.e. $\rho_{aspect} = \langle L \rangle \langle N \rangle^{-1} c_{2D}^{-1} = 200$. The intersheet spacing b is taken to be ≈1 nm. Notably, D is almost 500 times lower than the self-diffusivity of 50,000 g mol^{-1} PDMS (≈1.5 x $10^{-14} m^2 s^{-1}$) when adjusted to room temperature via the Arrhenius equation. [200] This is consistent with similar phenomena observed in the literature, in which DCM is shown to take roughly 10 times longer to diffuse through a 10 wt.% clay-PDMS composite relative to pristine PDMS. [201] In the case of polymer emulsions, the diffusing polymer chains and nanosheet aspect ratios are

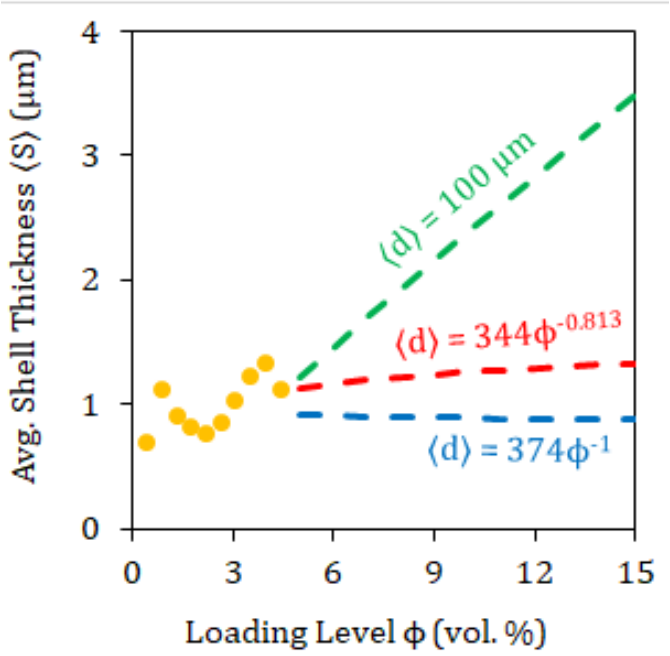

Figure 4.15: **Average shell thickness $\langle S \rangle$ *vs* graphene content ϕ (vol.%)**; calculated via Equations 4.25 to 4.27. Gold points represent the average shell thickness for the w/o emulsions presented in Figure 4.6. Green, red and blue lines represent the projected average shell thickness for the o/w emulsions shown in Figure 4.9 under maximum, expected and minimum over-coating conditions respectively.

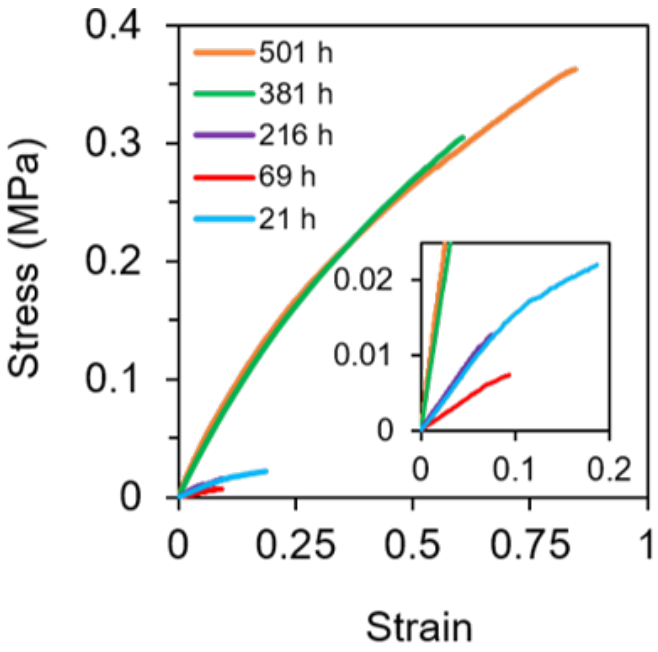

Figure 4.16: **Representative stress-strain curves *vs* interdiffusion time** for 7.4 vol.% graphene stabilised emulsion composites subjected to tensile strain until failure. Inset: Magnification of low-stress and strain region.

considerably larger than DCM and clays, explaining the additional factor of 50.

Although the ratio of PDMS to curing agent (10:1) greatly affects the degree of crosslinking, emulsion formation and polymer diffusivity of the polymer is dominated by the viscosity of the oil phase at room temperature. One strategy to reduce the interdiffusion time is to use a lower molecular weight PDMS with a reduced viscosity and higher diffusion coefficient. Attempting to accelerate the interdiffusion process by increasing the temperature to 65 °C during the rest phase leads to the premature crosslinking of the silicone spheres, producing G-balls within 30 minutes, as shown in Figure 4.10. This calculation assumes that the interdiffusion time is the time taken for mechanical integrity to be conferred to the composites, $\langle t_d \rangle \approx 250$ h, after which the toughness improves by a factor of ∼100 as shows in Figures 4.16 and 4.17. The stress strain curves in Figure 4.16 are representative of strain to failure measurements on no less than 6 samples per interdiffusion time studied, with each repeat showing a good degree of consistency, highlighted by the small standard

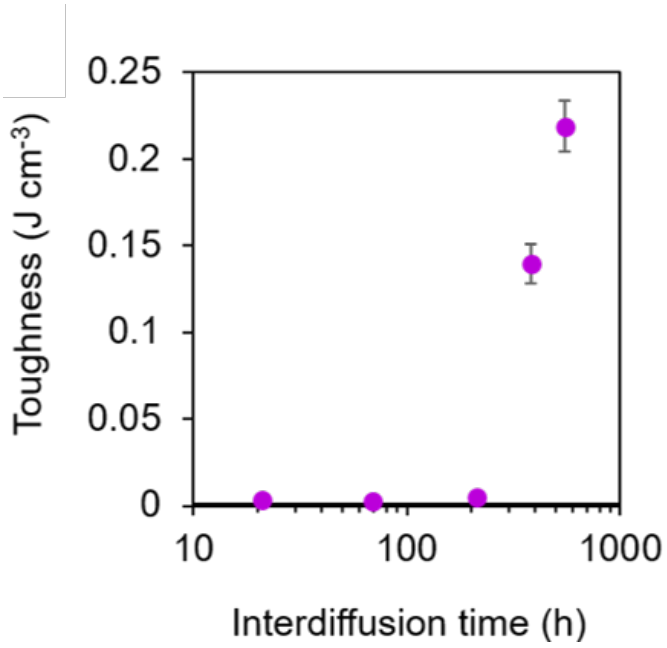

Figure 4.17: **Toughness *vs* interdiffusion time for 7.4 vol.% graphene stabilised emulsion composites subjected to tensile strain until failure,** showing a clear transition towards mechanical integrity at $t_d \approx 250$ h.

error in toughness shown in Figure 4.17. At low interdiffusion times, the performance is constant within statistical noise, while the mechanical toughness only increases drastically once a significant proportion of chains have diffused beyond the graphene shell, enabling inter-droplet crosslinking and changing the dominant failure mechanism from overcoming Van der Waals adhesion to chain pull-out or scission. [202]

Further, a doubling in conductivity is observed upon the densification of the G-balls into a continuous film as shown in Figure 4.18. This is attributed to the elimination of the void space between the G-balls increasing the electrical contact area between nanosheets and reducing the porosity of the composite film. Clearly, $\langle S \rangle$ and $\langle d \rangle$ play a vital role in composite formation and the resulting electromechanical properties.

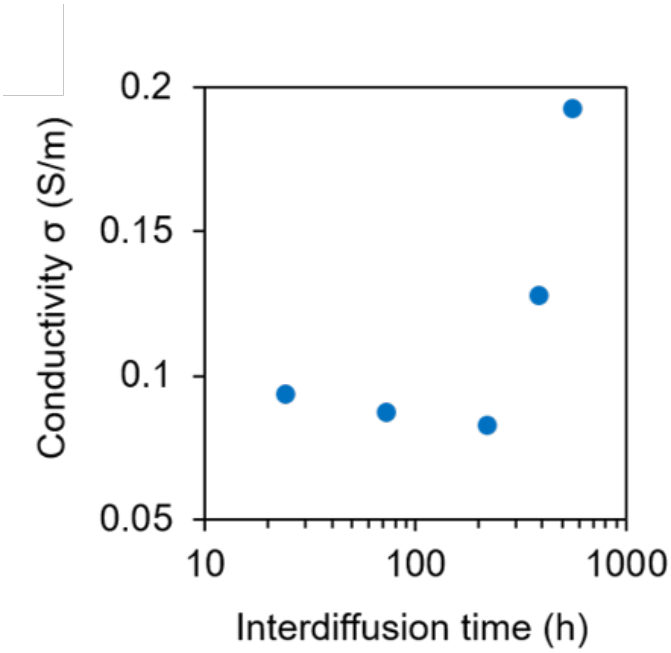

Figure 4.18: **Conductivity *vs* interdiffusion time for 7.4 vol.% graphene stabilised emulsion composites**, showing a clear increase in conductivity upon densification of the composites into elastomeric films.

Chapter 5

Electromechanical Properties of Emulsion Composites

5.1 Electrical Conductivity in Emulsion Composites

The morphology of the conductive network in emulsion-derived composites, visible in SEM of fractured cross-sections in Figure 4.13, is considerably different from the graphene networks found in traditional randomly distributed composites. By virtue of the production method, the graphene is strongly confined at droplet interfaces in the liquid system, meaning that the network structure is preserved after curing. As such, it is intuitive that electrical junctions will be of higher quality due to the reduced tunnelling distance between nearest neighbours. In random percolating networks, a significant portion of the conductive filler does not contribute to the conducting path or 'backbone' near the percolation threshold, resulting in a negligible contribution to macroscopic conductivity by comparison to the present system. In contrast, emulsion templated composites are largely self-similar over the loading levels studied, with the droplet size nearly constant only the shell thickness changes significantly. For $\langle t_d \rangle >> 250$ h, we would expect the electromechanical properties to be dictated by loading level itself rather than the varying degrees of interdiffusion through

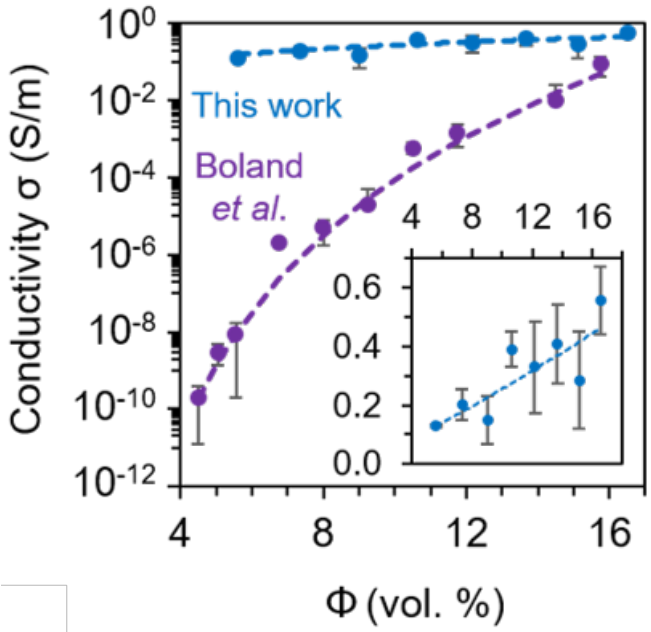

Figure 5.1: **Conductivity *vs* loading level for templated emulsion composites and a random graphene-silicone composite system** from the literature. [41]Inset is conductivity *vs* loading level for templated composites plotted on linear axes.

the different shell thicknesses.

We observe greatly enhanced conductivity at all measured loading levels with no apparent percolation threshold, compared to randomly-distributed graphene-silicone composites [41] which represent state-of-the-art soft strain sensor materials, shown in Figure 5.1. The conductivity of the templated system as a function of loading level can be fitted by, $\sigma = 0.027\phi$ with $R^2 = 0.94$ while in the random system $\sigma = 1.9 \times 10^{-15}(\phi - \phi_c)^{11.9}$ with $\phi_c = 1.75$, where ϕ here is in vol.%. The lack of a well-defined percolation threshold is to be expected for systems where droplet size increases at lower loadings, resulting in macroscopic conductive pathways at all loadings capable of forming stable emulsions. Assembling the graphene network into a reduced volume (i.e. at the oil-water interface) reduces the total filler required to achieve macroscopic conductive pathways, while interfacial tension aligns the graphene sheets to the tangent of the droplet surface. Both act to increase

the number of conductive junctions and improve the quality of those junctions through superior intersheet contact when compared to randomly distributed networks.

In order to interpret the conductivity-volume fraction scaling in these emulsion composites, it is possible to develop a simple model for the resistor network of the system and its variation with droplet size which is in turn a function of volume fraction. A network of emulsion droplets can be approximated by resistors between droplets R_j connected by two resistors in parallel corresponding to droplet surface R_s and through-droplet R_d conductivity, as schematised in Figure 5.2. Since the graphene sheets in Pickering stabilised emulsions will naturally tend toward the surface of any stabilised droplets to minimise the interfacial energy at the oil-water boundary, the resistance along the surface of the droplet can be considered distinct to the resistance through the droplet. A 2D projection of this "unit cell" as a square of side length d, with junction and surface thicknesses t_j and t_s, allows calculations of the total resistance and normalisation of the unit cell geometry. The total resistance of the unit cell, R_t is given by

$$R_t = R_j + \frac{1}{\frac{1}{R_s} + \frac{1}{R_d}} \tag{5.1}$$

such that

$$R_t = R_j + \frac{R_s R_d}{R_d + R_s} \tag{5.2}$$

For two droplets in contact, the conductivity of the junction can be approximated by $\sigma_j = L/R_j A \rightarrow \sigma_j = t_j/R_j d^2$ where d is the droplet diameter. The resistance between them can be approximated by $R_j = t_j/\sigma_j d^2$. Similarly, $R_s = 1/\sigma_s t_s$ and $R_d = 1/\sigma_d t_d$, such that

$$R_t = \frac{t_j}{\sigma_j d^2} + \frac{1/\sigma_s t_s \times 1/\sigma_d d}{1/\sigma_s t_s + 1/\sigma_d d} = \frac{t_j}{\sigma_j d^2} + \frac{1}{\sigma_s t_s + \sigma_d d} \tag{5.3}$$

Solving for the conductivity of the unit cell gives

$$\sigma = \frac{1}{d}\left(\frac{t_j}{\sigma_j d^2} + \frac{1}{\sigma_s t_s + \sigma_d d}\right)^{-1} \tag{5.4}$$

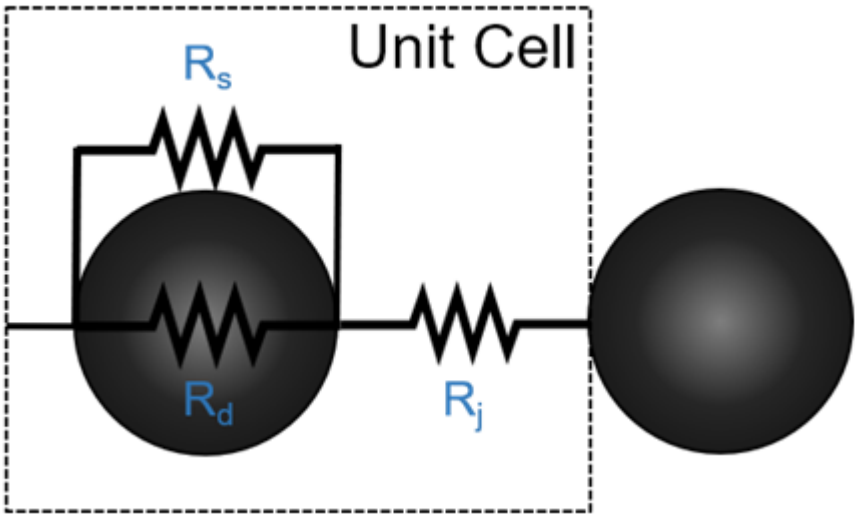

Figure 5.2: **Unit cell circuit diagram for solid stabilised droplets:** A simple model for the conductivity of a solid stabilised network of droplets using a unit cell approach. R_s, R_d, and R_j are the surface, droplet and junction resistances respectively.

In systems where the junction resistances are much lower than that of the surfaces/droplets, such as this one where the junctions are compositionally similar to the surfaces (PDMS-infiltrated graphene), the first term will be small and the conductivity scaling with droplet size will be dominated by the second term, i.e. $\frac{t_j}{\sigma_j d^2} \to 0$. Then we have

$$\begin{aligned} \sigma &= \frac{(\sigma_s t_s + \sigma_d d)}{d} \\ &= \frac{\sigma_s t_s}{d} + \sigma_d \\ &= \frac{\sigma_s \phi}{6} + \sigma_d \end{aligned} \tag{5.5}$$

In a cured state, $\sigma_d << \sigma_s$ as the droplet kernel consists of PDMS only. This results in a near direct proportionality with the gradient related to the conductivity of the PDMS-infiltrated graphene surfaces. We find that $\sigma = 0.027\phi$ provides a robust fit to the data in Figure 5.1, which suggests that the graphene conductive layer has an effective conductivity of 16 S m^{-1} based on the model calculation. Clearly this is significantly below what is typically expected of dense films of pristine graphene, further supporting the idea that the interfacial layers are interpenetrated with PDMS chains during film coalescence. Indeed,

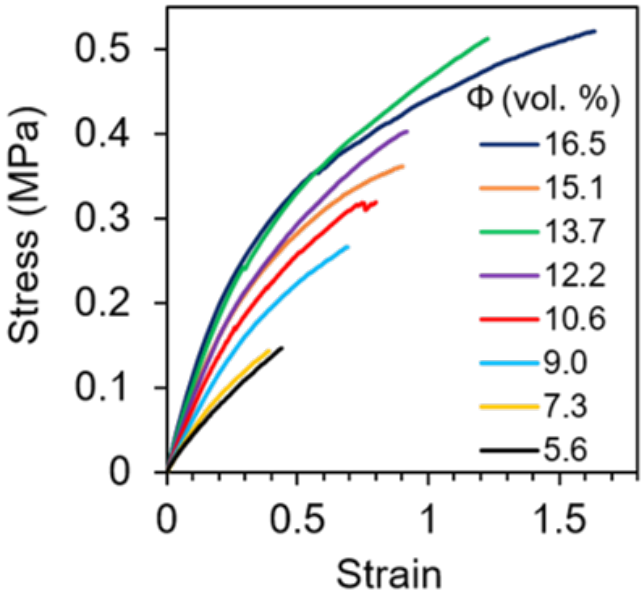

Figure 5.3: **Representative stress-strain curves *vs* graphene loading level** for graphene stabilised emulsion composites following tensile strain until failure.

assuming that the random graphene-PDMS composites in Figure 5.1 are comparable in loading-dependent conductivity (as an estimate) the functional form of the data suggests the graphene volume fraction in the shell is around 23 vol.%.

5.2 Mechanical Properties as a Function of Loading Level

In terms of the mechanical properties of the composites, the stress-strain curves in Figure 5.3 exhibit a clear increase in the strain at break and Young's modulus of the samples with increasing graphene loading. Figure 5.4 plots the Young's modulus as a function of graphene loading, which shows a linear trend over data range. The data for the random composites is plotted for comparison, [41] wherein a much greater increase of modulus with loading level is observed. It is important to note, as was discussed by Boland *et al.* [155] that nanocomposites used for strain sensing need to remain sufficiently soft that they comply with the surface being measured; human skin. As such, the much weaker dependence of modulus on loading level observed in the templated system may prove

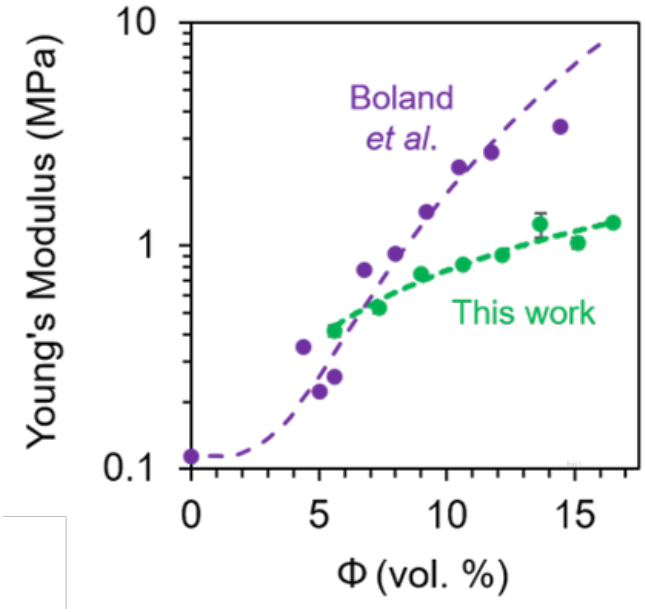

Figure 5.4: **Young's modulus *vs* graphene loading level** for graphene stabilised emulsion composites (green) and a random graphene silicone composite system from the literature (purple). [41]

beneficial to the design of on-skin sensors.

In contrast to the lower Young's modulus observed in the templated samples relative to the isotropic samples, Figure 5.5 shows that our composites, which are based on a cross-linked elastomeric silicone, have a significantly higher yield strain. The yield strain is near-constant, though both systems exhibit a decrease with increasing graphene content. We note that viscoelastic sensors with a significant viscous component will not recover once strained beyond the yield point. [41] As our sensors are highly elastic, it is possible to operate the materials over a much wider strain range.

The structure of the templated composites, as highlighted in Figure 4.13, consists of shells of graphene surrounding pristine PDMS 'cores'. These shells, which are interdiffused with PDMS chains, are responsible for increasing the Young's modulus (by virtue of interfacial stress transfer between the matrix and graphene) as well as the unusual increase in failure strain observed in Figure 5.3. The increase in failure strain is likely a result of the

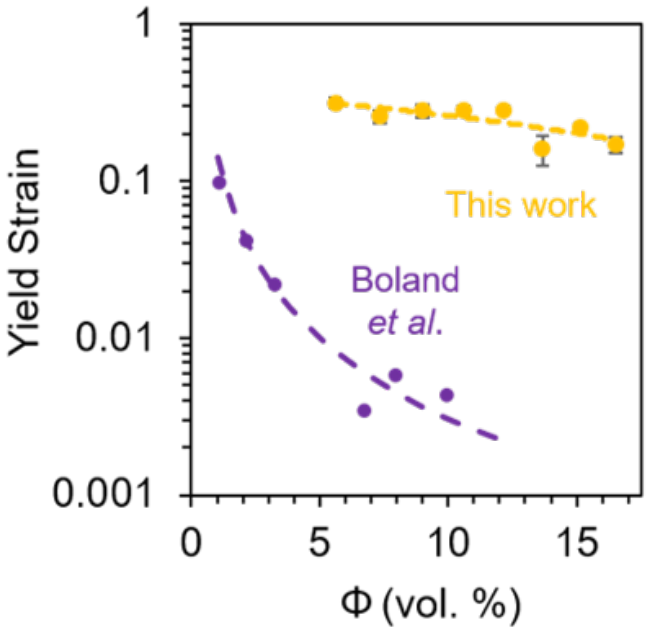

Figure 5.5: **Yield strain *vs* graphene loading level** for graphene stabilised emulsion composites (gold) and a random graphene silicone composite system from the literature (purple). [41]

reduction in overall cross-link density due to the penetration of the PDMS chains into the dense graphene shell, which interrupts inter-chain interactions both within and across the shell. Macroscopically we observe a large increase in the toughness of the composites as a direct result; see Figure 5.6. The fit suggests that composites at or below 5 vol.% would have negative toughness. Although unphysical, emulsified composites could not be formed at these loadings, and while pristine PDMS elastomers are considerably tougher at ~ 7.5 J cm^{-1}, their structure is fundamentally different and so cannot be directly compared.

A modification to the loss tangent of the composite materials with increasing graphene loading is anticipated; by virtue of lowering the cross-link density, the samples behave in an increasingly viscous but less elastic fashion (rather than being highly elastic, as is the case with pristine PDMS). A comparison of several samples' loss tangents obtained by dynamic mechanical analysis (DMA) with that of pristine PDMS films is shown in Figure 5.7, showing good agreement.

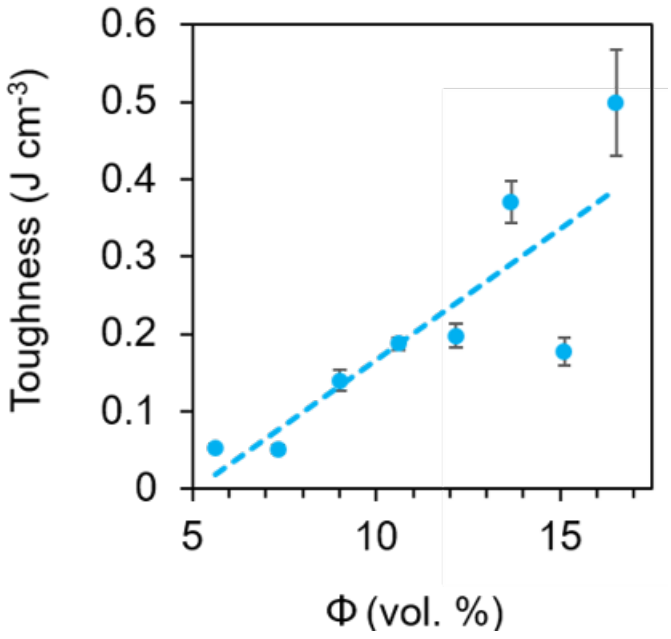

Figure 5.6: **Toughness *vs* graphene loading level** for graphene stabilised emulsion composites following tensile strain until failure.

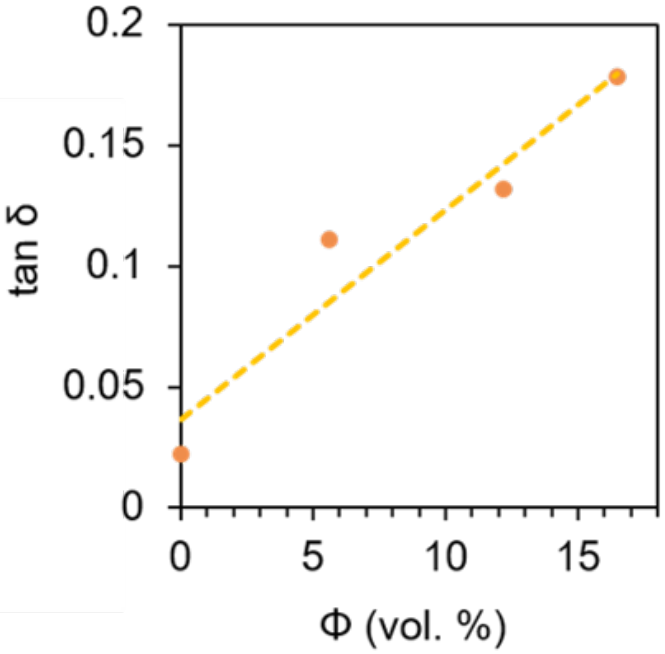

Figure 5.7: **Loss tangent tan δ *vs* graphene loading level** obtained via dynamic mechanical analysis.

5.3 Calibrating Electromechanical Response

The electrical properties and strain range of the composites demonstrated in Figures 5.1 and 5.3 naturally invite their application as strain sensors. Nanocomposites are attractive candidates for next-generation strain sensors due to their elasticity and conductivity and therefore electromechanical response but widespread adoption by industry has been hampered by non-linear effects such as hysteresis and creep, making accurate, repeatable strain readouts an ongoing challenge. [155] Strain sensitivity is most usually characterized as the relative change in resistance per unit strain known as the gauge factor G, restated here from Equation 2.4 for convenience from [203]

$$G = 1 + 2\nu + \frac{\Delta R/R_0}{\epsilon} \tag{5.6}$$

where ν is Poisson's ratio, ΔR the change in resistance, R_0 the initial resistance, and ϵ the applied strain. The gauge factor is a useful metric for characterizing sensitivity and reading out strain but applies only in the initial, linear region of R/R_0, a rule not always followed in the literature. [46, 155] Commercial strain sensors are typically based on metal foil gauges in which a significant portion of their sensitivity arises from the changing geometry under strain, as described by the Poisson ratio, ν. Since $\nu \sim$ 0.3-0.5 for most materials, higher sensitivities are only accessible via piezoresistivity. Accuracy and reliability are preferred over sensitivity and strain range, with commercial gauge devices exhibiting a highly linear response. Their main weakness, however, is their relatively low sensitivity and strain range, with gauge factors ranging from 2-5 and maximum strains of 5% strain or less. [48]. As a result of this operating range, such sensors are applicable in use cases such as measuring the deflection of rigid mechanical structures.

For practical applications, it is only necessary to have a calibrable electrical response to applied strain, i.e. consistent, strictly monotonic and detectable. The range over which these conditions hold will be referred to as the working strain range. For exponential

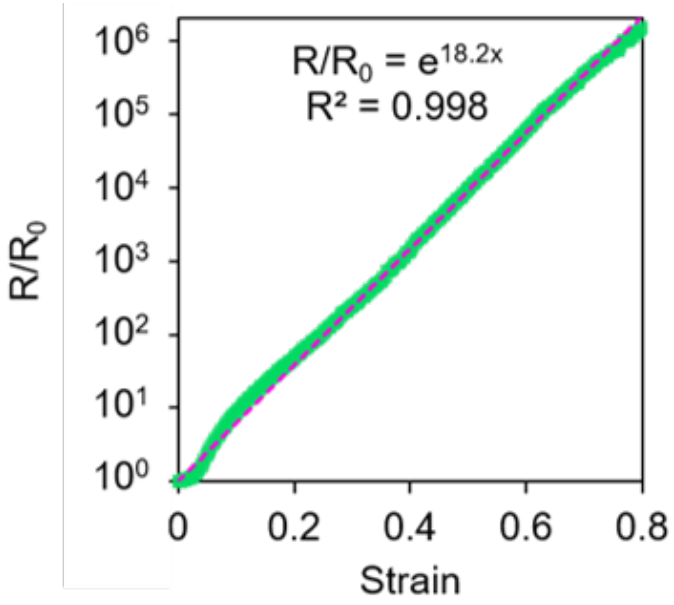

Figure 5.8: **Representative** R/R_0 ***vs*** **tensile strain** for ϕ = 16.5 vol.% graphene stabilised emulsion composite cured after 2500 h. The green points represent the sample's electrical response while the pink line is fitted using $R/R_0 = \exp(\mathrm{G}_{exp}\epsilon)$, with G_{exp} = 18.2.

responses, using $R/R_0 = \Delta R/R_0 + 1$ allows for a single parameter function of the form $R/R_0 = \exp(G_{exp}\epsilon)$ This behaviour is observed and shown in Figure 5.8, with R/R_0 as a function of strain for a high-loading composite (ϕ= 16.5 vol.%) shown over the working strain range. Plotting R/R_0 =exp($G_{exp}\epsilon$) with G_{exp} = 18.3 provides an excellent fit (R^2 = 0.998), holding up to 80% strain. Since exponentials are linear to first order, G_{exp} satisfies the definition of the gauge factor in the low strain linear regime.

Furthermore, G_{exp} appears to be independent of ϕ, fluctuating statistically randomly around 20 (Figure 5.9). This suggests that the exponential response is attributed to the deformation of the conductive network and subsequent tunnelling distance increase, with the average intersheet separation in the system remaining constant at all loading levels. The robustness of the exponential response suggests full calibration of the sensor is possible, facilitating accurate strain measurement even in the high strain regime. Note that if the calibration phase gives G_{exp} = 20, an error of ± 1 in G_{exp} corresponds to an error of

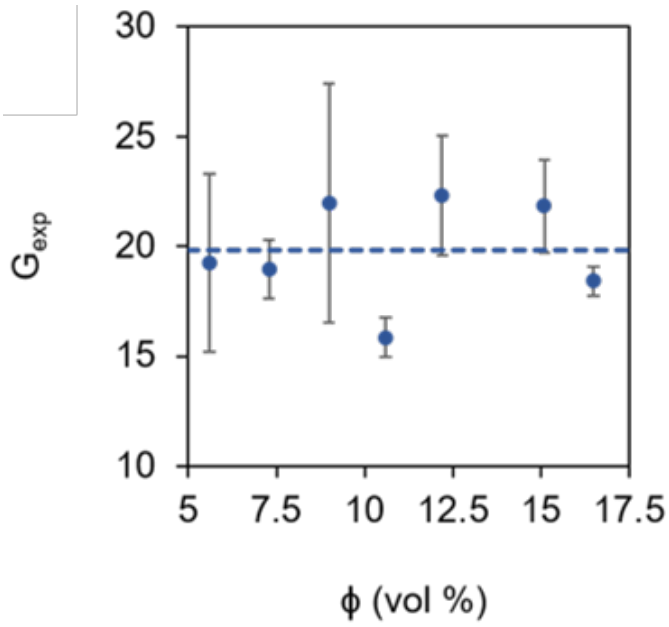

Figure 5.9: **Sensitivity exponent G_{exp} *vs* graphene loading level** where $G_{exp} = ln(R/R_0)/\epsilon$; for graphene stabilised emulsion composites cured after 2500 h.

5% in the calculated strain, as shown in Figure 5.10 (error = (true strain - estimated strain)/true strain). Although the functional form is independent of loading level, the maximum R/R_0 and working strain range are bounded by the conductivity and durability of the composite. Therefore, the highest loading level composites are the most suitable candidates for high-strain sensing.

Although exponential responses have been reported in other nanocomposite strain sensors, [36, 175] G_{exp} is significantly lower in these systems, ranging from G_{exp} = 1-5 and valid up to varying degrees of strain. Interestingly, some studies report an increase in G_{exp} at higher loadings albeit with significant scatter, [175] while others find G_{exp} to be constant across all loadings. [36] Despite the lack of standardisation in reporting strain sensor performance [155], Figure 5.11 facilitates an easy comparison of the sensors presented herein against over 230 linear and non-linear sensors found in the literature. [37, 39, 40, 42, 44–51, 53, 55, 56, 111, 124, 155, 164–180]. The maximum sensitivity, $\Delta R/R_0$ is plotted against the working strain at which this is achieved. Linear sensors (blue dots)

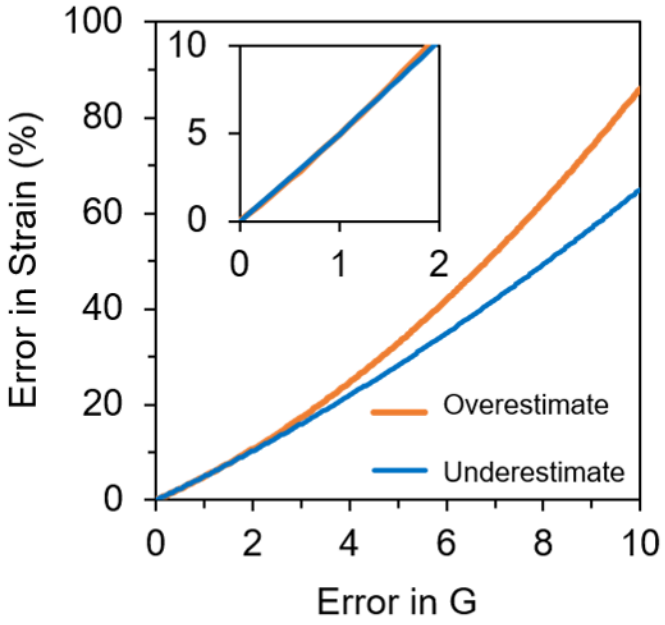

Figure 5.10: **Percentage error in strain as a function of the error in G_{exp}.** Assuming $G_{exp} = 20$, The orange line depicts the error when G_{exp} is overestimated while the blue line represents an underestimate.

have a linear functional form that runs parallel to the grey dashed lines, while non-linear sensors (red dots) seldom have a functional form that is or can be defined. The green line, $\Delta R/R_0 = \exp(G_{exp}\epsilon) - 1$ with $G_{exp} = 20$ is representative of our best sensors and is plotted up to 80% strain. When compared to both linear and non-linear strain sensors in the literature, our sensors exhibit the largest absolute change in resistance reported (Figure 5.11). This is attributed to the efficient packing and distribution of the nanosheets, enabling excellent conductivity at lower loading levels and reducing the impact on the working strain range.

The cycling performance at low strain (0.07%, Figure 5.12) and high strain (74%, Figure 5.13) is assessed. The samples were able to withstand >1000 cycles at 36% strain and >100 cycles at 74% before failure. A clear decrease in sensitivity is observed with increasing cycle number, in addition to a relatively small increase in resistance centered on the point of minimum strain in Figure 5.13. This small increase arises due to stress relaxation, a

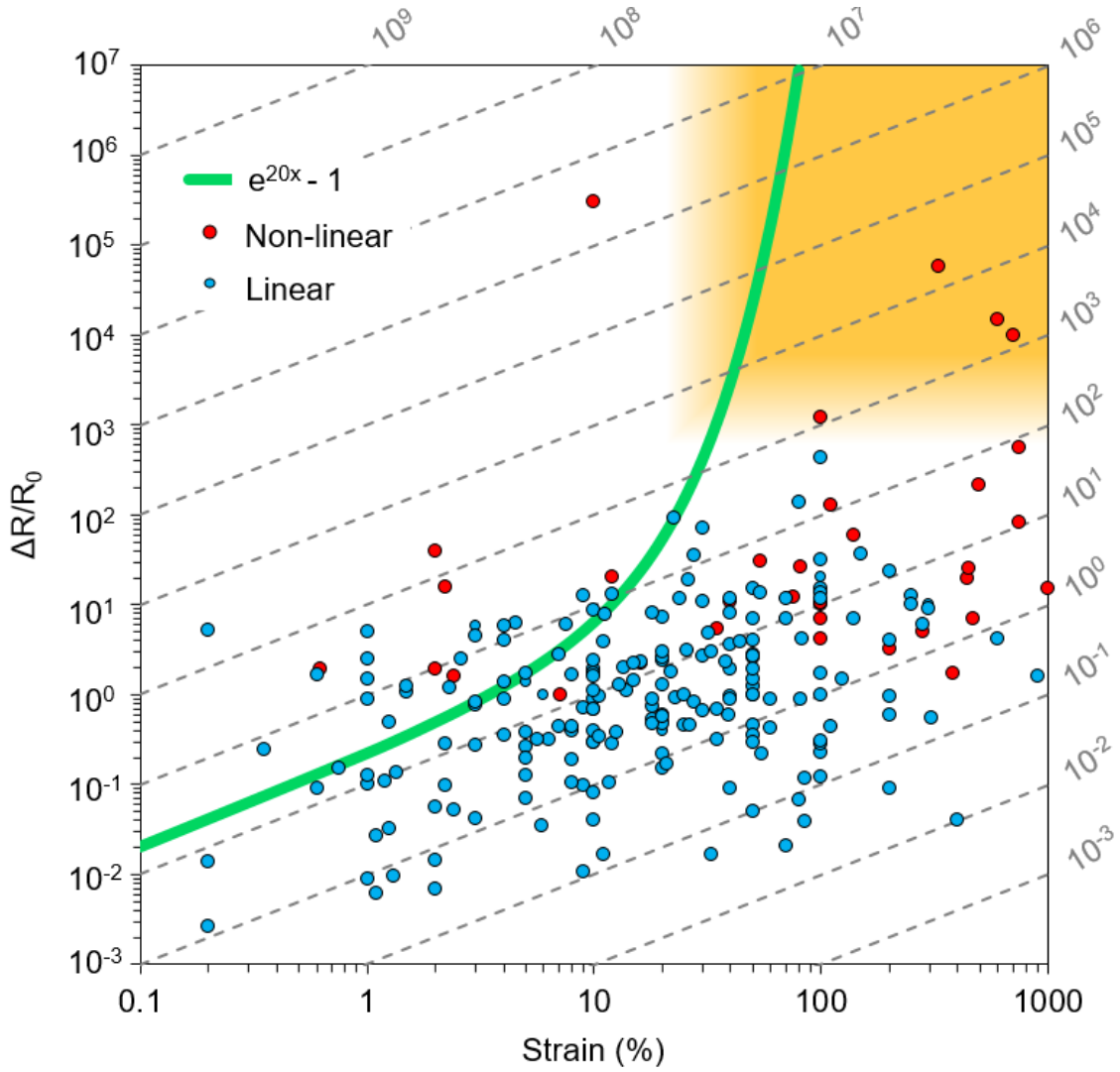

Figure 5.11: **Electrical response $\Delta R/R_0$ *vs* strain compared to over 230 references**. [37, 39, 40, 42, 44–51, 53, 55, 56, 111, 124, 155, 164–180] Blue dots indicate the maximum sensitivity and strain range of linear sensors regimes while red dots indicate the maximum sensitivity and strain range of non-linear sensors. The green line represents the response of the sensors presented herein, $\Delta R/R_0 = \exp(20\epsilon) - 1$ while the gold region highlights the challenge region of high sensitivity and high strain. The dashed gray lines correspond to the gauge factor G.

viscoelastic effect, whereby the elastomer is to release a relatively small amount of tension during the strain cycle thanks to the mobility of the constituent polymer chains. As a result, the point of zero strain shifts and the elastomer is instead slightly compressed at the end of each cycle, causing a small uptick in resistance with each cycle. This effect will be considerably more pronounced for larger strains with longer cycles, which is why it is not observed Figure 5.12.

Indeed, G_{exp} is found to decay to $G_{exp} \approx 4$ after tens of cycles, after which it remains constant independently of strain magnitude as shown in Figure 5.14. Whilst signal fatigue is undesirable, recent analysis by Boland [43] indicates that it is universal among all nanocomposite strain sensors. In particular, the author shows that $\Delta R/R_0$ decays as a function of cycle number C, such that

$$\Delta R/R_0 \propto C^{-0.1} \tag{5.7}$$

Where the exponent determines the rate of fatigue and takes an average value of 0.1 for all sensors studied. Despite this, a steady state can be reached in which the signal decay is so small that it can be neglected. The number of cycles at which this occurs is defined as the endurance limit.

It is interesting then that, for the emulsion based sensors, both R/R_0 and the sensitivity exponent G_{exp} decay as a function of $\mathrm{C}^{-0.1}$. Under cyclic strain, a typical R/R_0 *vs* time plot (Figure 5.15) has three distinct regions; the first strain cycle applied to a relaxed sample, a time-dependent fall in resistance and finally a stable oscillation between local minima and maxima.

The first exhibits the largest electrical response to applied strain that can be fitted using an exponential of the form $R/R_0 = \exp(\mathrm{G}_{exp}\epsilon)$. Upon relaxation, R trends toward R_0 at a rate that decays according to Equation 5.7, a phenomenon caused by the mobility of the nanosheets in the matrix phase. To understand this, first consider the orientation of all nanosheets in the network. As strain is applied, the nanosheets will become increasingly

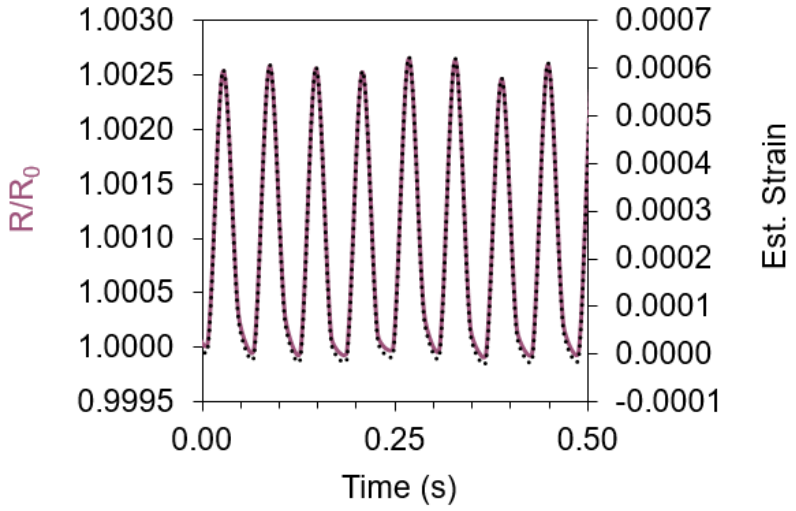

Figure 5.12: R/R_0 **(purple) and estimated strain (black dotted)** ***vs*** **time for cyclic strain of 0.07% driven at 16.67 Hz.**

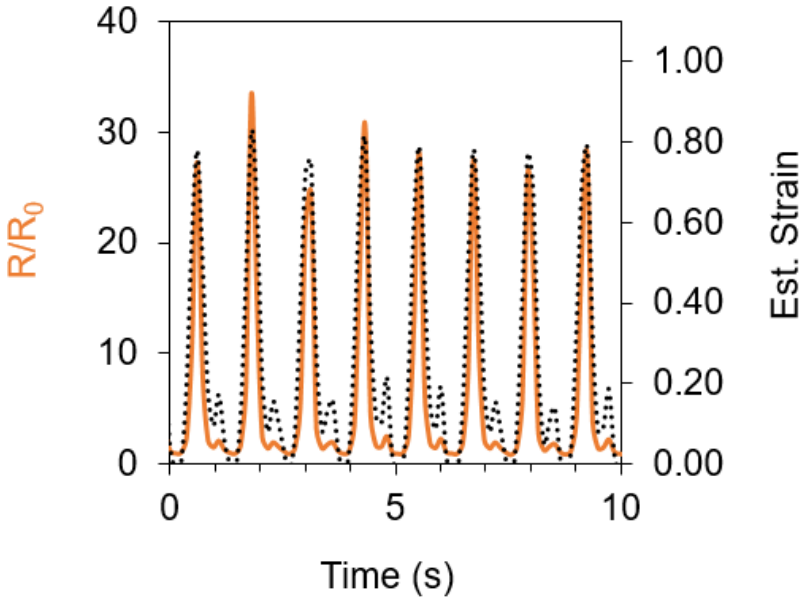

Figure 5.13: R/R_0 **(orange) and estimated strain (black dotted)** ***vs*** **time for cyclic strain of 74% driven at 0.81 Hz.**

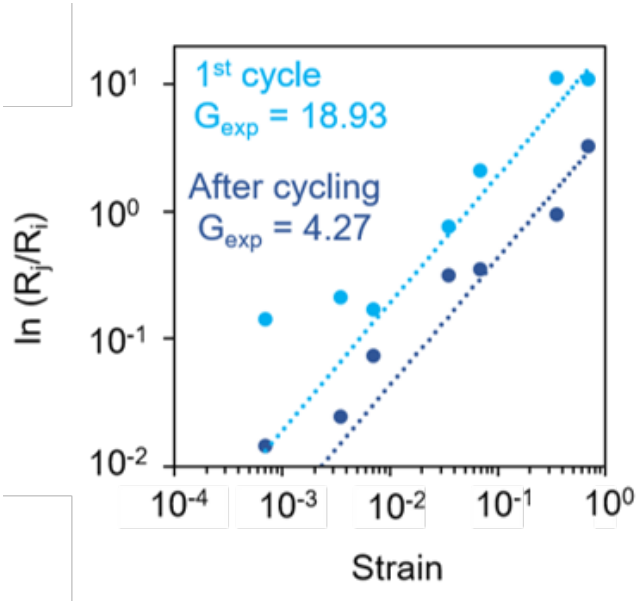

Figure 5.14: **Sensitivity decay of G_{exp} as a function of strain** between the first cycle (light blue) and > 100 cycles later, (dark blue) converging to $G_{exp} \approx 4$.

aligned along the axis of strain. At a molecular level, polymer chains will continue to reptate past one another, changing the local environment of the nanosheets and forcing them to re-orientate accordingly. We can therefore ascribe the local rotational diffusivity of the filler to the self-diffusivity of the polymer. Eventually, an equilibrium is reached in which the nanosheets are all randomly orientated, on timescales related to the polymer relaxation time. In practice, this should impose a lower bound on the driving frequency that can be analysed successfully.

Another challenge facing nanocomposite sensors is viscoelastic creep, characterised by a phase lag between applied stress and the induced strain. If a constant stress is applied and held, the strain will continue to increase or 'creep', according to an associated time constant. A related phenomenon is stress relaxation, in which the internal stresses do not dissipate immediately on the alleviation of external pressures but according to an analogous time constant. One corollary is that the tensile stress required to achieve a constant level of strain decays as a function of time. We suppose that the decreasing

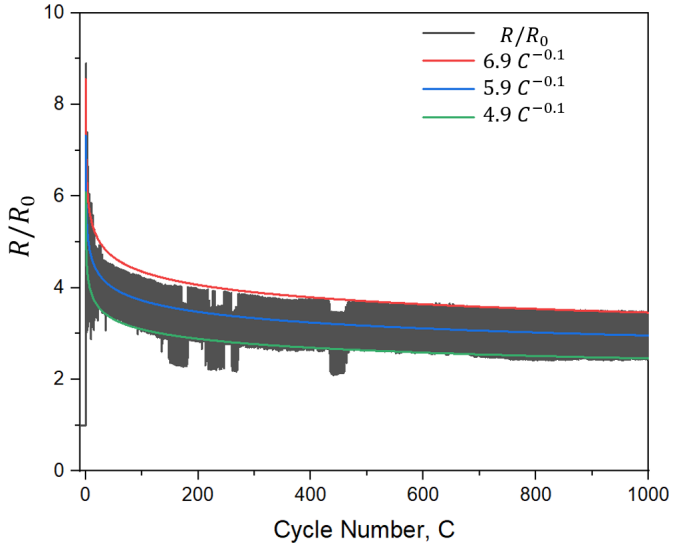

Figure 5.15: **Representative signal decay *vs* cycle number.** R/R_0 is plotted in black, while the peak to peak maxima, minima and average are estimated by $6.9\mathrm{C}^{-0.1}$ (red), $4.9\mathrm{C}^{-0.1}$ (green) and $5.9\mathrm{C}^{-0.1}$ blue respectively.

sensitivity is correlated to the stress relaxation of the sensor under cyclic tension [43], and by extension the tendency of the material to creep. Eventually, the change in stress becomes small enough that it can be ignored and the electrical response stabilises to a value of $G_{exp} \sim 4$ at the steady state limit. This value is in agreement with those reported elsewhere for sensors with an exponential response to applied strain [36, 175], which may indicate some universal phenomenon. As before, a constant value of $G_{exp} \sim 4$ after initial cycling enables an estimate of strain, as plotted on secondary axis in Figures 5.13 and 5.14.

The driving frequency is easily extracted from the time series following a fast-Fourier transform (FFT) (Figure 5.16) with high fidelity. This is promising for health monitoring applications such as heart rate monitoring.

5.4 Bodily Motion Strain Sensing

Strain scenarios specific to the human body, including finger bending, pulse and breathing are applied in Figures 5.16 to 5.20, with the electrical response examined. Figure 5.17

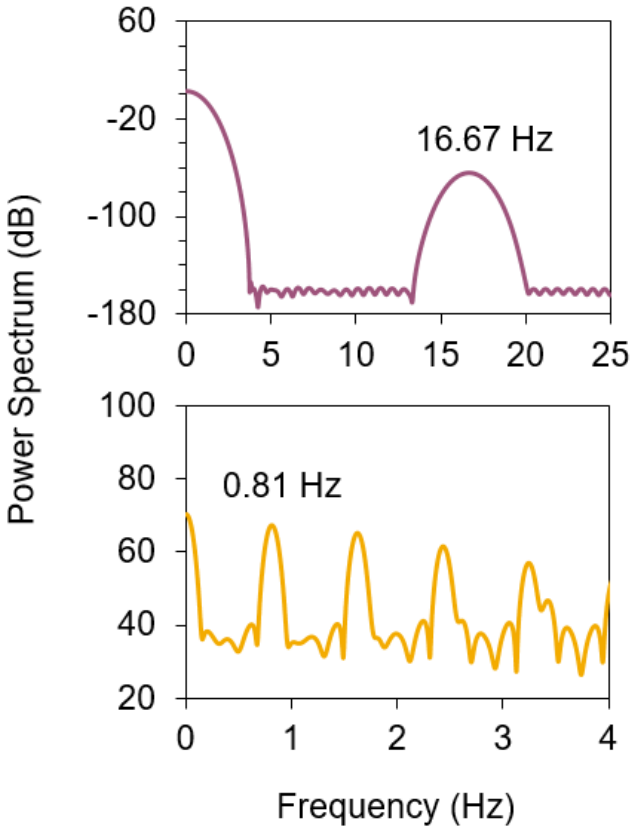

Figure 5.16: **Fourier transform of R/R_0 *vs* time for low (0.074%) and high (74%) cyclic strain** presented in Figures 5.12 and 5.13, with the peak power frequency labelled.

shows the sensor in a relaxed state when taped to the index finger (5.17A), and in a strained state under maximum bending (5.17B). In Figure 5.18 we show the electrical response to multiple fingers bends over a small (<10°) (5.18A), medium (≈ 45°) (5.18B) and large (≈ 90°) (5.18C) bending radii. When fully extended, the sensor is ≈ 4 cm, rising to ≈ 5 cm under large bending, or ≈ 25% strain. The strain is approximated using $\epsilon = ln(R/R_0)/G_{exp}$ and setting $G_{exp} = 20$, as determined in Figure 5.9 and is in good agreement with the expected strain.

The sensor is placed on both the neck and chest while the electrical response is recorded, as depicted in Figures 5.19 and Fig 5.20. When the sensor is gently pressed against the carotid artery (5.19A), the pulse is clearly detectable as shown in Figure 5.20A. Following a fast Fourier transform, a narrow peak at 59 beats per minute (BPM) emerges (Figure 5.20B). When placed on the chest, the sensor is able to detect both high-strain, low-frequency modes associated with breathing and high-frequency, low-strain modes associated with a pulse as shown in panel C. The fact that the pulse signal is easily discernible over the breathing mode speaks to the versatility of the exponential response and its potential as a biomedical sensor. Inset to Figure 5.20C is the pulse waveform once the respiration induced baseline drift is subtracted. This is also subject to a Fourier transform in Figure 5.20D, revealing a maximum at 65 BPM, typical of a resting heart rate.

5.5 Conclusion

A method of incorporating large quantities of graphene nanosheets into a PDMS matrix in a structured, controllable fashion that results in excellent electromechanical properties ideally suited to strain sensing applications has been developed. The underlying principles of the technique are established to enable additional optimisation, and in principle one may extend this approach to other polymers and nanomaterials of interest. The morphology of the emulsion-templated network imbues the composite with conductivities several orders of

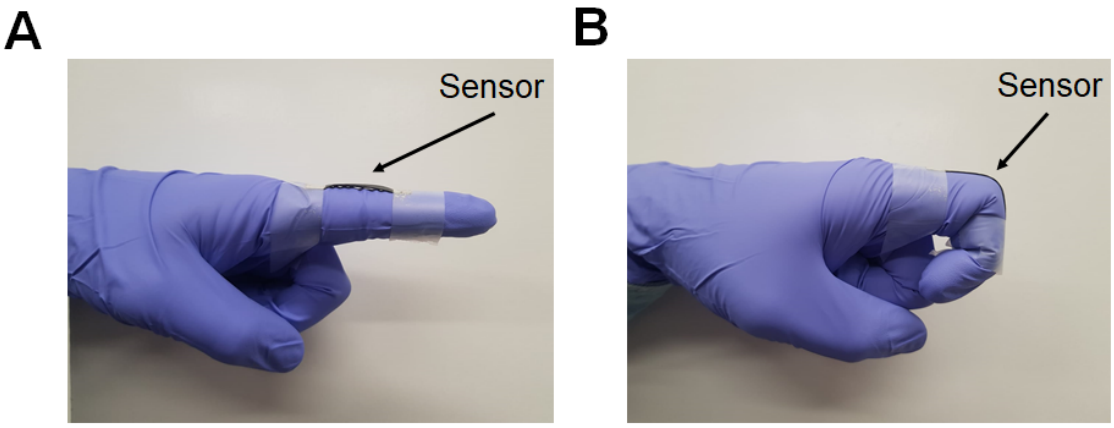

Figure 5.17: **Photograph of sensor attached to a finger in neutral and fully bent position A.** Sensor in relaxed position with finger fully extended, attached using scotch tape. **B.** Sensor under full extension for finger bending.

magnitude higher than isotropic composites at low loading levels (≈5 vol.%) and is likely responsible for the robust exponential sensitivity to strain. Able to detect strains <0.1% and >80%, these sensors enable measurements of pulse, joint motion, and respiration. Such a promising technology may prove especially useful in established fields such as healthcare, sports performance monitoring and rapidly growing fields such as soft robotics.

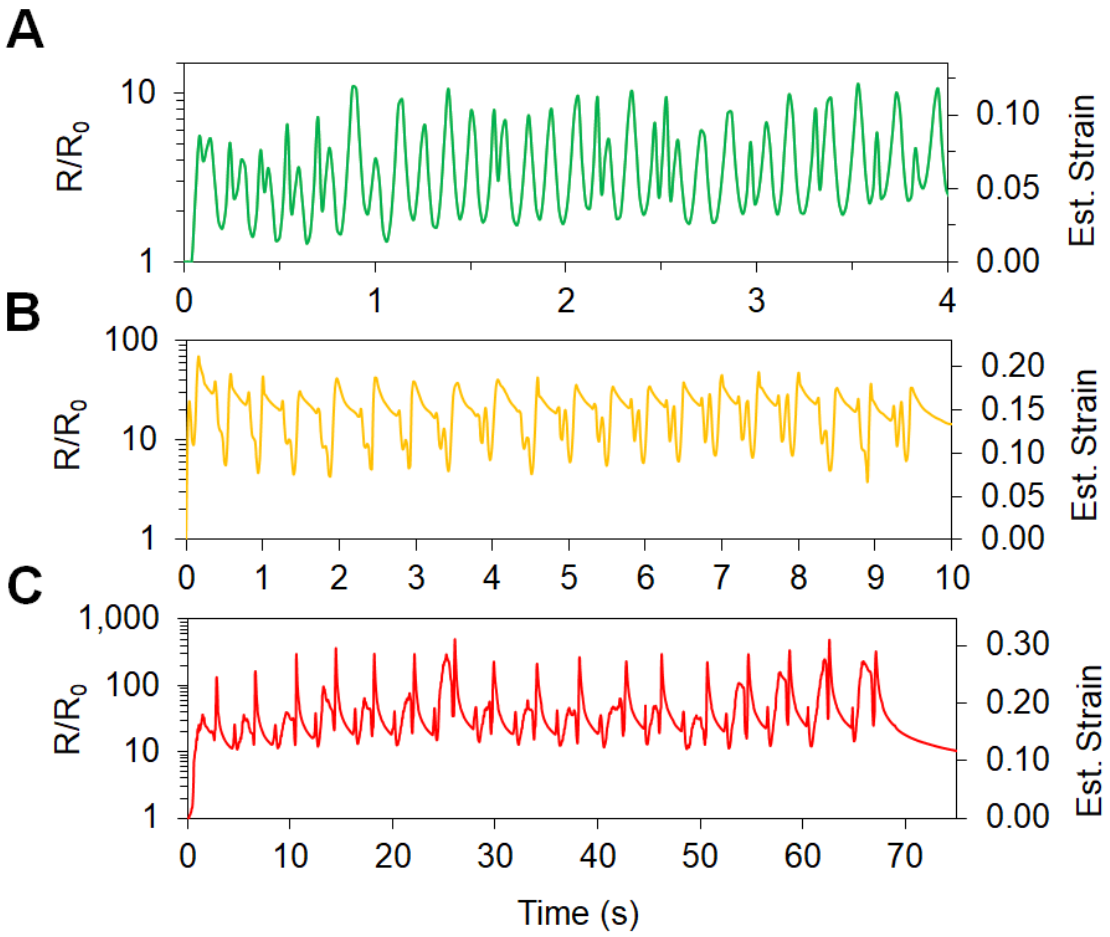

Figure 5.18: R/R_0 ***vs*** **time during repeated finger-bending with the estimated strain on the second axis.** **A.** Small ($<10°$) bending radius. **B.** Medium ($\approx 45°$) bending radius. **C.** Large ($\approx 90°$) bending radius.

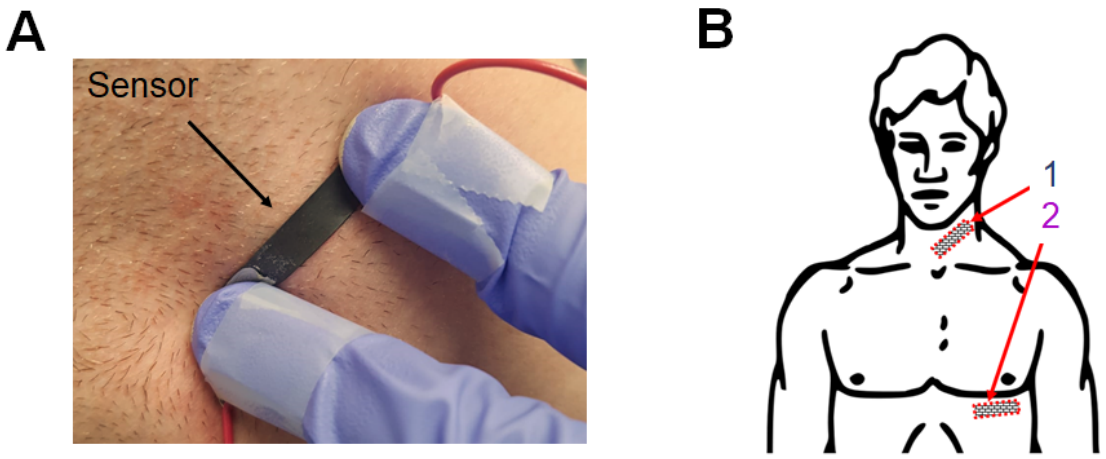

Figure 5.19: **Sensor placement for heart-rate and respiration monitoring. A.** Photo of sensor placement over the carotid artery. **B.** Diagram of sensor placement for (1) heart-rate monitoring and (2) simultaneous heart-rate and respiration monitoring.

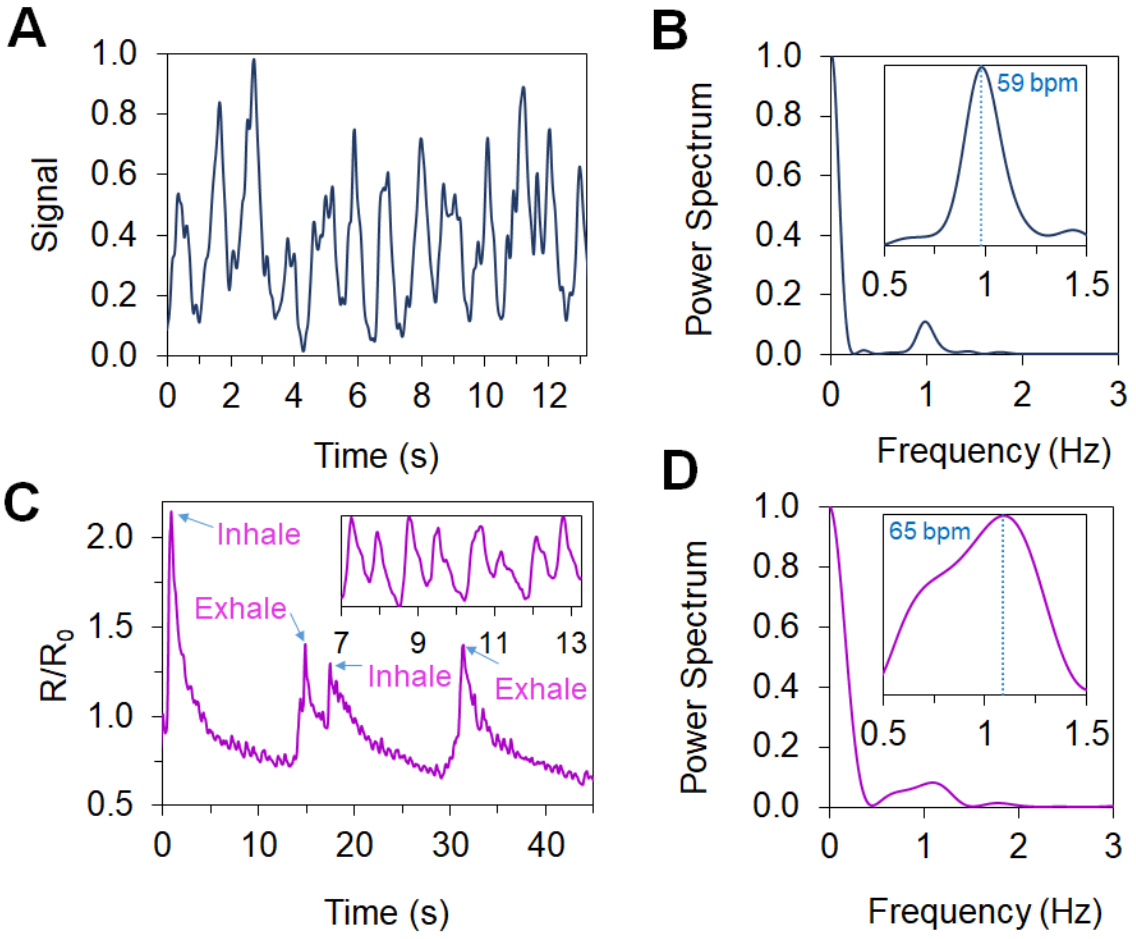

Figure 5.20: **Electrical response for heart-rate and respiration monitoring A.** Normalised electrical response from the carotid artery with baseline drift subtracted. **B.** Fast Fourier transform of electrical response in A. Inset: Peak at 59 BPM. **C.** Electrical response from the chest during respiration. Inset: Pulse waveform extracted following baseline drift subtraction. **D.** Fast Fourier transform of electrical response in C. Inset: Peak at 65 BPM.

Chapter 6

Graphene-Stabilised Porous Silicone Composites

6.1 Introduction

In this Chapter, the production and use of graphene-stabilised porous silicone composites for pressure sensing is explored. Silicone is commonly used for highly sensitive, piezoresistive nanocomposite sensors with many devices demonstrated in the literature [41, 52, 54, 57, 204] owing to its range of useful properties; biocompatibility, chemical resistivity, good transparency processability etc., but in particular its low Young's modulus, which enables excellent stress transfer between soft, elastomeric substrates similar to human skin. Not only does this ensure conformability, it imbues high sensitivity as relatively small stressors induce larger strains through the bulk, deforming the conductive network and resulting in significantly higher changes to resistivity. While pressure is the target stimuli to be measured, it is the induced strain that dictates changes to the morphology of the network and thus induces a piezoresistive response. Additionally, compressive strain sensing does not require high tensile (or compressive) strength, suggesting that the networks of graphene-coated silicone spheres studied in this thesis may be promising in this application area.

Based on a recent review by Zang *et al.* [1], the following pressure sensing ranges can be defined; ultra-low pressure (<1 Pa), subtle-pressure (1 Pa - 1 kPa), low-pressure (1 - 10 kPa), medium-pressure (10 - 100 kPa) and high-pressure (0.1 - 1 MPa). Depending on the final application, an ideal pressure sensor should be able to detect a wide range of applied pressures and exhibit a regular, repeatable response that enables calibration.

Several changes were made to the production methodology outlined in Chapter 4. The graphene used to stabilise the silicone oil droplets is produced via homogenisation in an aqueous surfactant solution as demonstrated in [90]. Few-layer graphene is size selected by centrifugation and re-dispersed in ethylene glycol. This is then blended with Ecoflex 00-30, a softer (70 kPa) platinum-cure silicone with a lower viscosity (3000 cP) and molecular weight [205] than Qsil B, without the addition of any solvents. Finally, the composites are cured immediately following emulsification, with minimal time for polymer interdiffusion across the boundary.

A summary of typical physical properties for Ecoflex and Qsil 216 is provided in table 6.1. Both silicone oils are vulcanised additively via a hydrosilylation reaction at room temperature with a platinum catalyst. In this reaction, a silicon-hydrogen (Si-H) bond is added across the unsaturated carbon-carbon double bond (C=C) of an olefin, resulting in a new silicon-carbon (Si-C) bond as depicted in Figure 6.1. [206]. Generally, the molecular weight of each polymer determines the viscosity of the oil, while the crosslink density in the cured state increases overall tensile strength at the expense of elasticity. Thus, we may infer that Ecoflex has a lower overall molecular weight in the melt state and lower cross-link density in the cured state.

There are several motivations for these changes. Aside from a significant increase to elasticity and deformability offered by Ecoflex relative to Qsil 216, they represent a significant reduction in complexity to the production process. Secondly, the morphology of the resulting composite is simpler to understand and characterise, by virtue of its similarity

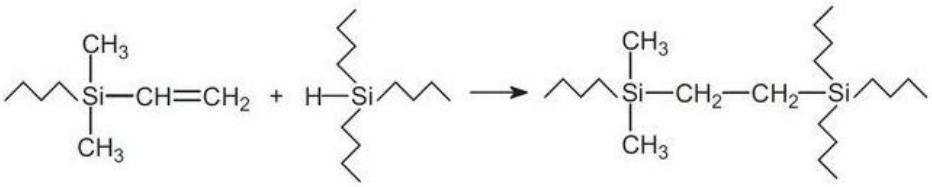

Figure 6.1: **Hydrosilylation reaction for platinum cured polysiloxanes.** A silicon-hydrogen bond is added across the unsaturated carbon-carbon double bond in the presence of a platinum catalyst, resulting in a new silicon-carbon bond. [206]

Property	**Qsil B 216** [207]	**Ecoflex 00-30** [208]
Viscosity (mPa s)	4500	3000
Specific Gravity	1.02	1.07
Tensile Strength (MPa)	4.80	1.4
Elongation at break	100 %	900%
Mix ratio	10:1	1:1

Table 6.1: Contrasting physical properties for two widely used commercially available silicone oils, Qsil 216 and Ecoflex 00-30.

to the emulsion. Based on Chapter 4, networks of conducting spheres with a well-defined morphology should form by not allowing the polymer enough time to diffuse through the graphene network *en masse*. Utilising homogenised graphene ensures greater control over the stabiliser with respect to commercially-available powders, leading to thinner films at the interface and demonstrates the versatility of the method to different graphenes.

Eliminating the solvents from the dispersed droplet phase ensures that the composites comprise graphene coated silicone spheres when cured, aiding in modelling and analysis of derived networks. It also simplifies the interpretation of composite mechanical properties since there are no modifications to the cured polymer mechanics as a result of solvation. [209]. Using a lower molecular weight polysilicone such as Ecoflex confers increased deformability in tension and compression relative to Qsil B, leading to greater sensitivity to applied pressure. The lower viscosity of Ecoflex is more closely matched with EG, reducing the shear rate required for droplet break-up during the emulsification phase. [210] Finally, loading the graphene into the continuous phase may affect its distribution in the final composite. Once the continuous phase is removed, all of the graphene will reside on the droplet surface and interstitial sites. When loaded into the droplet phase, sheets that are not bound to the interface may become trapped in the droplet core, contributing less efficiently to the overall conductivity.

6.2 Characterisation of Few-Layer Graphene

As discussed in Chapter 4, the morphology of the droplet network largely depends on the size distribution of the stabilising sheets, with smaller droplets enabled by smaller, thinner sheets. Then, it is important to characterise the average length $\langle L \rangle$ and average layer number $\langle N \rangle$. Optical spectroscopy techniques are fast and non-invasive ways to probe ensemble sheet properties.

Dynamic light scattering can be used to probe the average size of graphene sheets, albeit

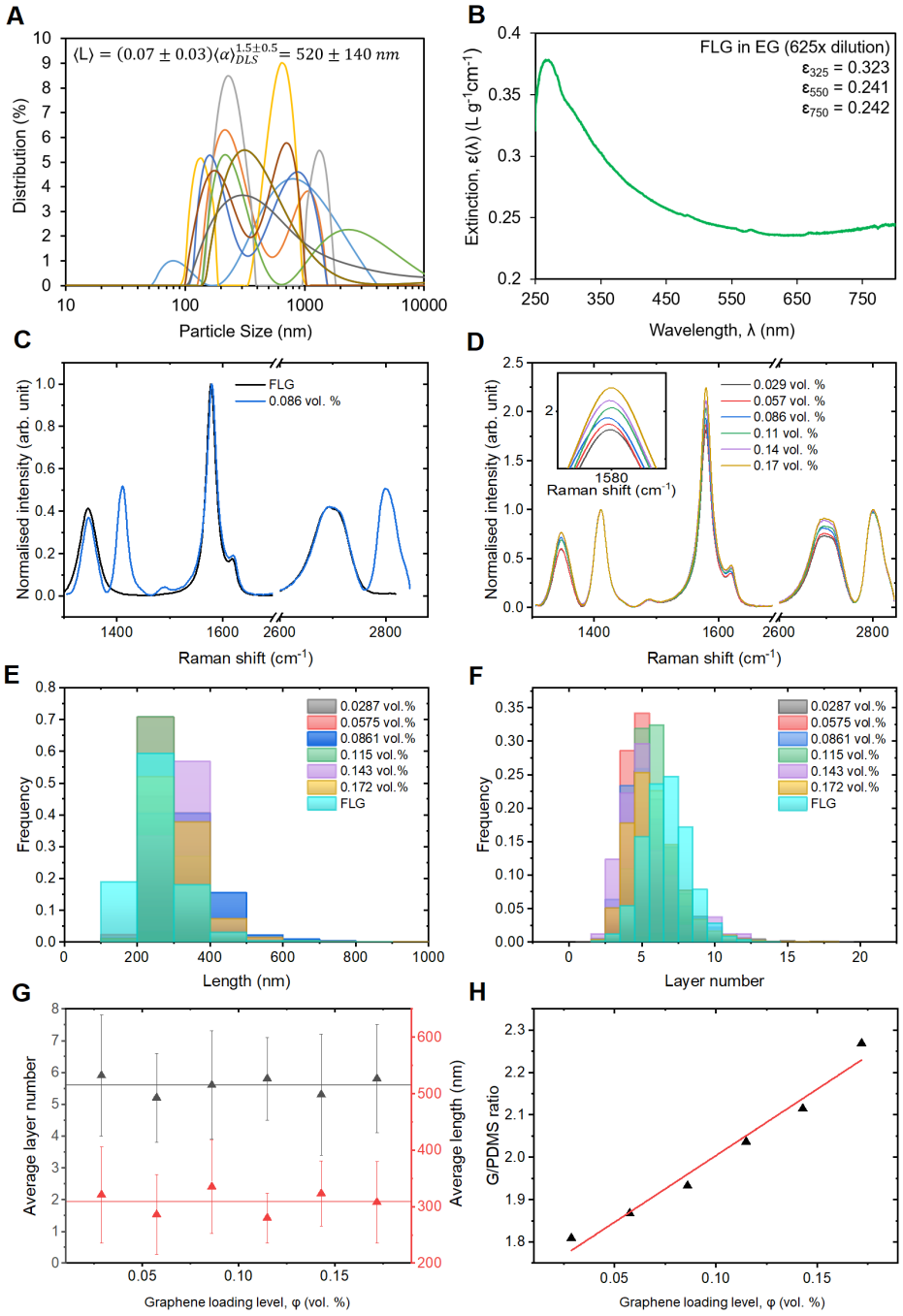

Figure 6.2: **Characterisation of few-layer graphene. A.** Particle size distribution of FLG dispersed in ethylene glycol **B.** Extinction spectra for a 625x diluted dispersion. **C.** Raman spectra for graphene film sprayed from a 25x diluted dispersion of FLG in EG *vs* graphene-stabilised porous silicone composites. **D.** Raman spectra normalised to I_{1411} *vs* loading level **E.** Nanosheet length distribution for various loadings. **F.** Nanosheet layer number distribution for various loadings. **G.** Average layer number ⟨N⟩ and length ⟨L⟩ *vs* graphene loading level, calculated from well-established Raman metrics [85]. **H.** Ratio of G (1580 cm^{-1}) to Ecoflex (1411 cm^{-1}) peak intensities *vs* loading level.

with a sizeable error of ∼40% owing to the uncertainty in the proportionality constant and exponent in Equation 3.13. [193]. Ten individual measurements of a dilute graphene-EG dispersion are taken due to the considerable variation in the particle size distributions shown in Figure 6.2A. The peak intensity for each measurement is taken as the hydrodynamic radius α_{DLS}, which is then correlated to average nanosheet length using Equation 3.13, yielding $\langle L \rangle = 520 \pm 140$ nm.

UV-visible extinction spectroscopy is used to determine the concentration of graphene in a diluted dispersion based on the extinction of incident light, from which the composite loading level is derived. A typical undiluted dispersion following redispersion into EG is calculated as 2.78 mg mL^{-1} from Figure 6.2B using Ext = ϵCl, given an extinction of 0.242 at 750 nm for a 625x dilute dispersion and a graphene extinction coefficient of ϵ_{750} = 54.5 $Lg^{-1}cm^{-1}$ [85]. Similarly, the average layer number can be estimated empirically using $\langle N \rangle$ = 25 x Ext_{550}/Ext_{325} - 14.8 [85], yielding $\langle N \rangle = 3.9 \pm 0.8$.

In Figure 6.2C, comparative Raman spectra for a thin film (100 nm ± 20 nm) sprayed from few-layer graphene in EG *versus* a 0.088 vol.% composite is shown, without any Ecoflex features from the film. Raman spectra are similarly taken over a 70 µm x 70 µm area for each loading level, as shown in Figure 6.2D. Ensemble length and layer number in the film are $\langle L \rangle$ = 258 nm ±71 nm and $\langle N \rangle$ = 6.7 ±1.6 [191] respectively, while the composites are found to have an average layer number of $\langle N \rangle$ = 5.6 ±1.7 and average size of $\langle L \rangle$ = 302 nm ± 69, as shown in Figures 6.2E, F and G. That these results are consistent (within error) and are independently in agreement with UV-vis and DLS measurements respectively lead to the conclusion that the emulsification process preserves the morphological properties of the graphene nanosheets.

The ratio of the G peak (1580 cm^{-1}) intensity to CH_3 peak (1411 cm^{-1}) intensity increases with loading level as shown in Figure 6.2H. This is expected given that the volume ratio of graphene to Ecoflex increases with loading and absorbs a greater proportion

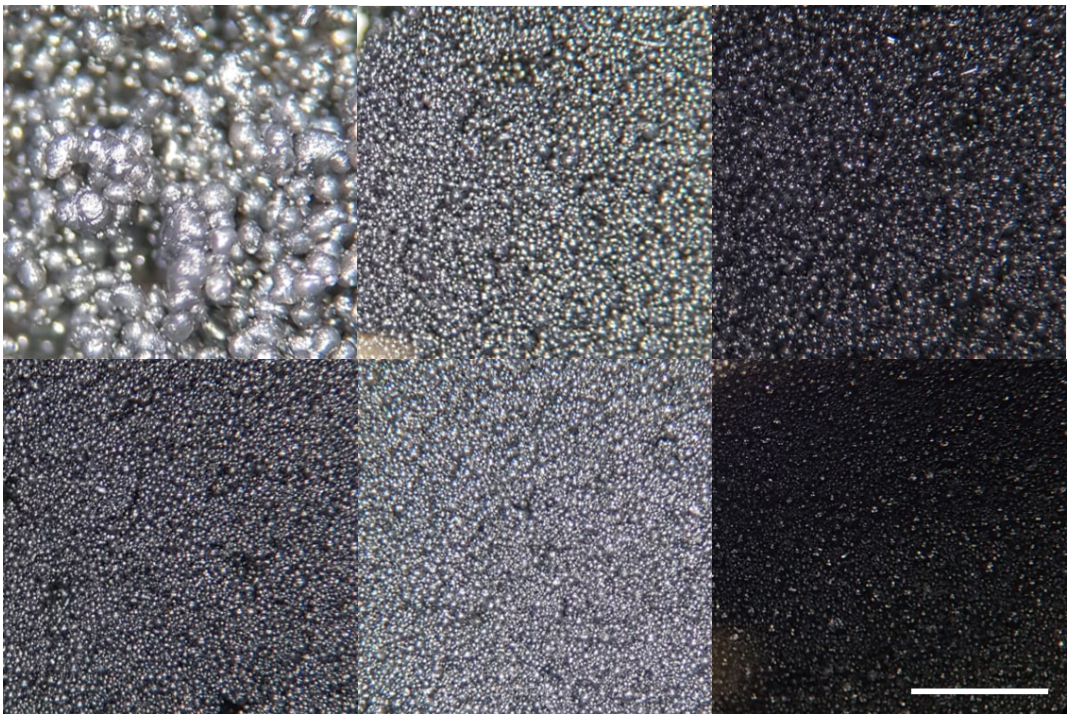

Figure 6.3: **Optical microscopy of few-layer graphene-stabilised porous silicone composites**. Left to right, top to bottom: 0.03, 0.06, 0.09, 0.11, 0.14, 0.17 vol.% measured from UV-Vis extinction spectra. Scale bar 1 mm.

of the incident laser light. Notably, the ratio of the D/G and 2D/G feature intensities are independent of graphene loading level. This supports the notion of a consistent layer number $\langle N \rangle$ and sheet length $\langle L \rangle$ for the loading levels studied. [85] The relative intensities of the asymmetric CH_3 stretch at 1410 cm^{-1} and the G peak can be related to the loading level by an empirical fit of $I_{1580}/I_{1411} = 3.14\phi + 1.69$ based on the proportionality between them. Although the offset is unphysical as $\phi \to 0$, it may be explained by the templating of the nanosheet network in which graphene is concentrated at the surface of the Ecoflex spheres, in contrast to a traditional randomly distributed network.

6.3 Composite Morphology

Figure 6.3 shows optical microscopy of the graphene-coated PDMS spheres as a function of graphene loading level, from which statistics are obtained using image analysis software.

It is apparent that both the droplet size distribution in Figure 6.4A and mean droplet size $\langle d \rangle$ in Figure 6.4B trend toward smaller and more uniform droplets as the loading level increases. As expected for emulsified systems, an inverse relationship between $\langle d \rangle$ and ϕ is observed, in which $\langle d \rangle = 6.5\phi^{-1}$. Physically, this translates to no additional over-coating, such that all additional graphene surface area at higher loadings stabilises smaller droplets. Using $\phi = 6N_{shell}C_{2d}/\langle d \rangle$ and assuming an average interlayer spacing of $C_{2d} = 1$ nm, typical of liquid phase exfoliated graphene, then there are $\langle N_{shell} \rangle \sim 14$ layers per sphere on average and this is approximately independent of loading level for the range studied, as plotted in Figure 6.4C. Since the shell thickness $\langle S \rangle = N_{shell}C_{2d}$, it follows that $\langle S \rangle = 14$ nm on average. Further, the transmittance $T(N)$ of graphene is given by [211]

$$T(N_{shell}) = (1 - \pi\alpha)^{N_{shell}} = 0.977^{N_{shell}} \tag{6.1}$$

Here $\alpha = 1/137$ is the fine structure constant that defines the coupling strength between light and charged particle interactions, and by extension the optical transmissivity of a graphene monolayer. [211] Noting that $T(14) = 72\%$ and $T(28) = 52\%$ (accounting for entry and exit through a spherical shell), single spheres would be expected to be translucent, which is indeed observed.

Further supporting the presence of thin, few-layer graphene shells, the emulsified droplets stabilised by few-layer graphene are found to be considerably smaller than those stabilised by commercially available graphene powder despite the greatly reduced loading level, where 40 µm $\leq \langle d \rangle_{FLG} \leq$ 210 µm for 0.03 vol.% $\leq \phi_{FLG} \leq$ 0.17 vol.% and 104 µm $\leq \langle d \rangle_{G-powder} \leq$ 635 µm for 0.44 vol.% $\leq \phi_{G-powder} \leq$ 4.4 vol.%, as shown in the inset to Figure 6.4B. This is attributed to the improved exfoliation state of the FLG, resulting in a higher surface area and lower bending rigidity. [212]

It should be noted that spheres with a diameter <10 µm cannot be reliably measured via optical microscopy (due to the reduced focal depth at high magnification), skewing the

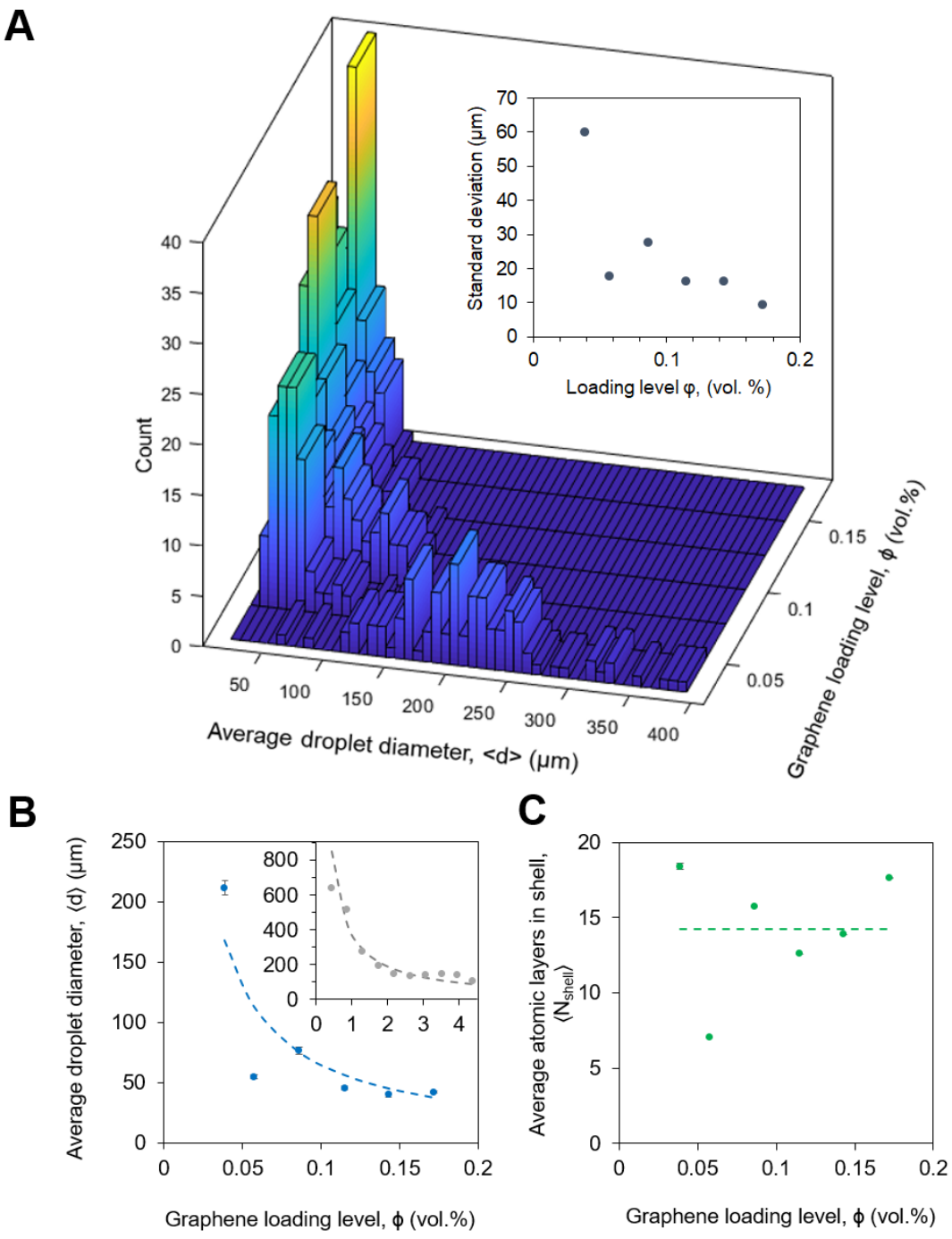

Figure 6.4: **Sphere morphology as a function of loading level. A.** Droplet size histograms plotted for as a function of loading level. **B.** Average (mean) droplet diameter *vs* loading level, with $\langle \mathrm{d} \rangle = 6.5\text{Ø}^{-1}$ plotted as a blue dashed line. Inset is the scaling for commercially available graphene powder-stabilised emulsions from Chapter 4. **C.** Average number of atomic layers in shell $\langle N_{shell} \rangle$ *vs* graphene loading level, with the average across all loadings $\langle N_{shell} \rangle = 14$ atomic layers plotted as a green dashed line.

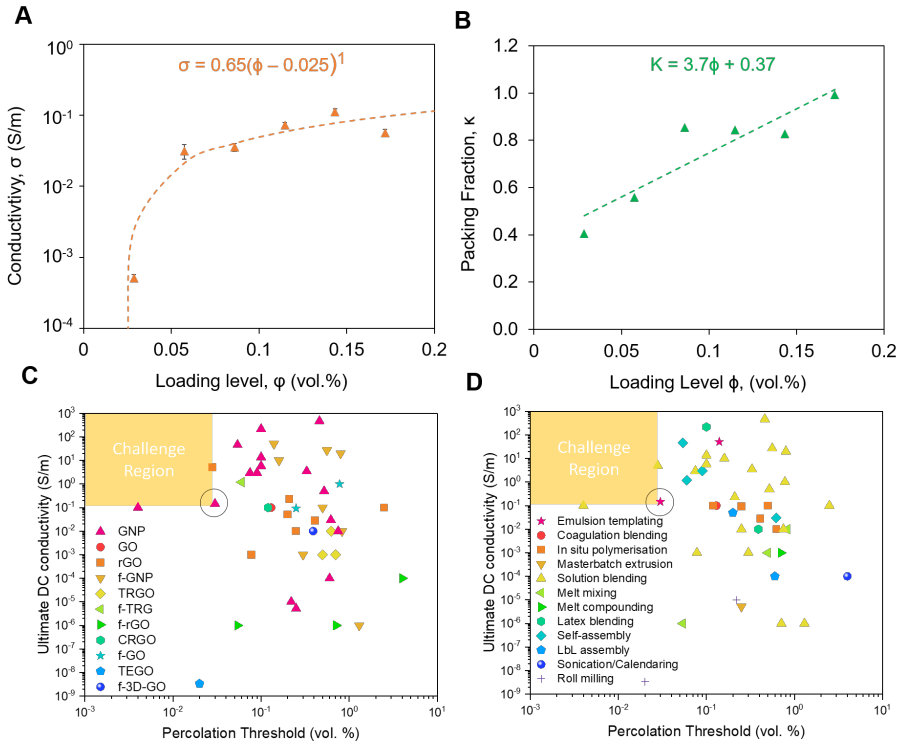

Figure 6.5: **Electrical properties of few-layer graphene composites. A.** Conductivity *vs* loading level. **B.** Packing fraction *vs* loading level. **C.** Ultimate DC conductivity *vs* loading level coloured by filler type. **D.** Ultimate DC conductivity *vs* loading level coloured by production methodology. In C and D, the present work is circled.

distributions and average droplet size measurements presented in favour of larger droplets. Consequently, the average droplet diameter ⟨d⟩, shell thickness ⟨S⟩ and transmissivity T should be treated as upper bounds.

6.4 Electromechanical Properties

The conductivity as a function of loading level is presented in Figure 6.5A. Noting that the loading level is measured with respect to the Ecoflex only (neglecting porosity), a linear scaling between conductivity and loading can be fitted, albeit with a small offset, such that $\sigma = 0.65\phi$ - 0.016 for $\phi > 0.025$ vol.%. While the linear scaling is expected for emulsion-templated systems, [150] these results can be further interpreted using percolation

theory by rewriting as $\sigma = 0.65(\phi\text{-}0.025)^1$ for $\phi > \phi_c$ and $\sigma = \sigma_{Ecoflex} < 10^{-11}$ S m^{-1} for $\phi < \phi_c$. Then, the percolation threshold is $\phi_c = 0.025$ - extraordinarily low for composite systems. [13] A percolation exponent of unity is consistent with templated composites presented in chapters 4 and 5 in addition to nano-sheet stabilised emulsions in the literature. [150] A low percolation exponent corresponds to a narrow range of inter-sheet junction resistances [41, 126] and is expected given the localisation of nanosheets at the oil-water interface and the formation of a thin film.

A linear scaling also suggests rule of mixtures behaviour above the percolation threshold. Extrapolating to $\phi = 100$ (vol.%) gives $\sigma = 65$ S m^{-1}, which is consistent with the conductivity of a thin film (120 ± 20 nm) of graphene sprayed from a graphene-EG dispersion, yielding $\sigma = 100$ S m^{-1}. The similarity between film and composite conductivity is perhaps unsurprising given the similarity of the shell morphology to films at the nanoscale, although the ultimate conductivity is much poorer than typically expected for LPE graphene, which can be in excess of 10^4 S m^{-1}. [13]

Taken together, these results imply that the shortfall in ultimate conductivity for emulsion-templated systems may be attributed to the presence of inter-diffused polymer chains and/or the use of non-ideal carrier solvents such as EG. Additional optimisation in the form of higher curing temperatures to reduce inter-diffusion or modification to the graphene (e.g. chemical functionalisation) could be explored in future work to improve the dispersibility in EG and potentially the overall conductivity.

Figure 6.5B shows how the packing fraction κ varies with increasing loading level, based on the composite density relative to pristine Ecoflex. Note κ increasing linearly with ϕ, approaching unity at 0.17 vol.%. The implication is that narrower droplet size distributions presented in Figure 6.4A pack more efficiently with increasing loading. In Figure 6.5C, the ultimate conductivity and percolation threshold of our system (*i.e.* the maximum conductivity and minimum loading level shown in A) against a variety of composite systems

that use graphene and its derivatives (graphene nanoplatelets, graphene oxide, reduced graphene oxide etc.). Figure 6.5D makes an analogous comparison for the composite production method, e.g. solution blending, emulsion templating, etc. The percolation threshold is a measure of how efficiently a network forms, while the ultimate conductivity assesses the quality of the formed network in terms of connectivity and charge transport. As shown in Figures 6.5C and D, emulsion templated composites exhibit high conductivity at low loading levels, especially when compared with other composite systems presented in the literature. [13]

To assess the pressure sensing capability of the composites, a series of tests were performed to examine the sensitivity as a function of loading level ϕ, applied pressure P, strain rate $\dot{\epsilon}$, and number of cycles c. The results are presented below.

6.5 Loading Level Dependence

The dependence of sensitivity on loading level is assessed in Figures 6.6 and 6.7. For each test, the electrical response is recorded as a function of both pressure and strain. In all cases, the relative change in resistance R/R_0 increases exponentially with applied pressure P at a rate defined by the sensitivity exponent G_{exp}, such that $R/R_0 = exp(G_{exp}P)$. The maximum pressure and relative resistance change at which this function holds defines the working pressure P_w and working relative resistance change $(R/R_0)_w$ and represent the practical sensing limits of the nanocomposites described. In Figure 6.7A, the working pressure P_w is shown to increase linearly between 0.18-0.71 MPa, such that $P_w = 3.5\phi$. Given the relatively high modulus of graphene compared to soft silicone and presence of a percolating network, a non-negligible contribution to the modulus is expected. The linearity of the fits suggests a rule of mixtures type scaling, in which the composites with additional graphene undergo greater reinforcement and are able to sustain greater pressures despite the decrease in working strain. Conversely, the working strain is broadly

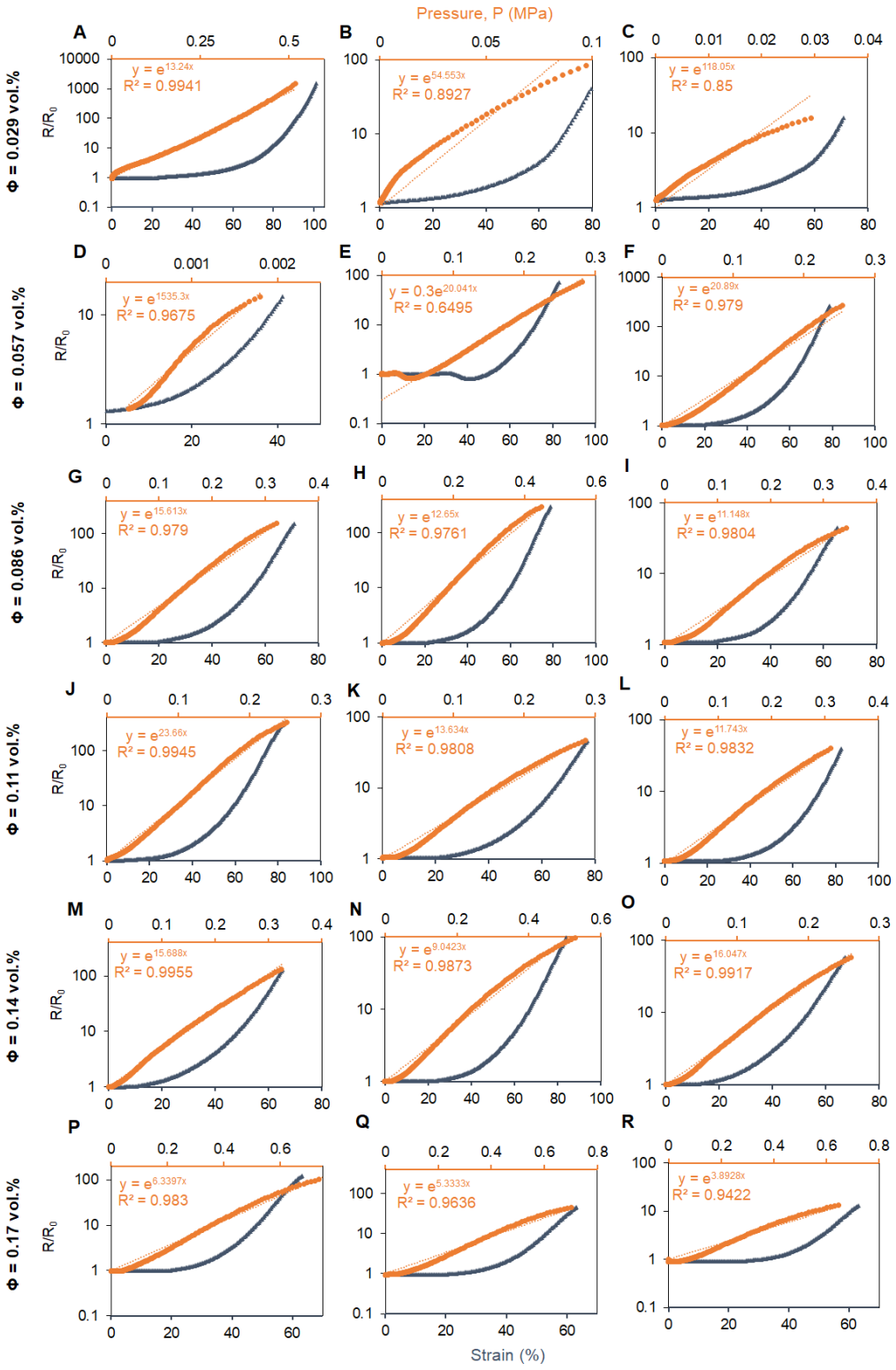

Figure 6.6: **Electrical response to applied pressure and strain *vs* loading level.** R/R_0 is plotted *vs* applied pressure P (secondary x-axis) and strain (x-axis) for increasing loading levels. **A-C.** 0.029 vol.%. **D-F.** 0.057 vol.%. **G-I.** 0.086 vol.%. **J-L.** 0.11 vol.% **M-O.** 0.14 vol.%. **P-R.** 0.18 vol.%. In all cases, R/R_0 is fitted using $R/R_0 = \exp(G_{exp}P)$ where G_{exp} is the sensitivity exponent and P is given in MPa.

flat at 74% with increasing graphene content, albeit with significant scatter as shown in Figure 6.7B. This may be ascribed to the self-similarity of the network despite the higher loadings. Interestingly, the relative resistance change appears to decay exponentially at higher loadings in Figure 6.7C, according to $R/R_0 = 470e^{-11\phi}$. That the lowest loading levels are the most sensitive is not entirely surprising, indeed, analogous phenomenology is often observed in other composite systems where the most sensitive loadings lie just above the percolation threshold [41]. It is intuitive that smaller stressors are required to disrupt a barely connected network, causing relatively large changes in conductivity. This is in spite of the lower resistivities at higher loadings, which give more scope for a relative change in resistivity as observed for the elastomeric strain sensors discussed in Chapter 5.

As a corollary, the sensitivity exponent G_{exp} decreases exponentially as a function of loading, according to $G_{exp} = 290e^{-23\phi}$ as shown in Figure 6.7D. The electromechanical variation in response for a given loading decreases dramatically at higher loading levels, and suggests that these composites may be calibrated as pressure gauges.

6.6 Strain Rate Dependence

To ascertain the dependence of sensitivity to strain rate, a target pressure of 13.3 kPa is applied to a 0.17 vol.% composite at a range of compressive strain rates, between 0.57-114% s^{-1} or equivalently 0.01-2 Hz. So as to ensure the validity of results, the tests were performed from slow to fast and after significant pre-conditioning to mitigate signal decay effects and with several minutes between tests to allow the samples to recover electrically and mechanically.

In Figure 6.8, the electrical response (blue) to the mechanical stimuli (green) are plotted on a dual axis against time. Note that although the response time is faster than the sampling rate of the IV-probe, (<0.04s or 25 Hz), the recovery time is of order 100 s for the parameters studied. It is immediately clear that the stimulus induced over shorter

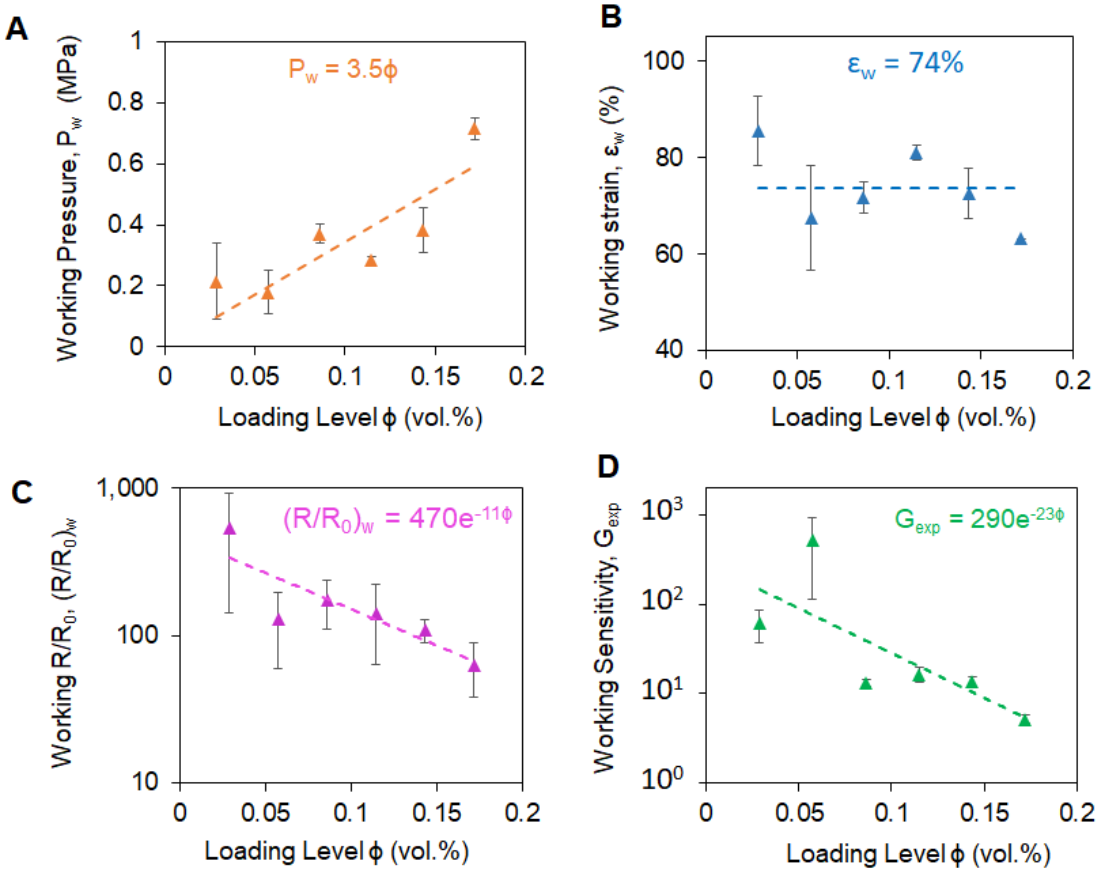

Figure 6.7: **Pressure sensing as a function of loading level for few-layer-graphene emulsion composites. A.** Working Pressure, P_w, defined as the pressure at which R/R_0 deviates from the fitting function $\exp(G_{exp}P)$, as a function of loading level. **B.** Working strain, ϵ_w as a function of loading level. **C.** Working R/R_0, $(R/R_0)_w$ as a function of loading level. **D.** Working sensitivity G_{exp} as a function of loading level.

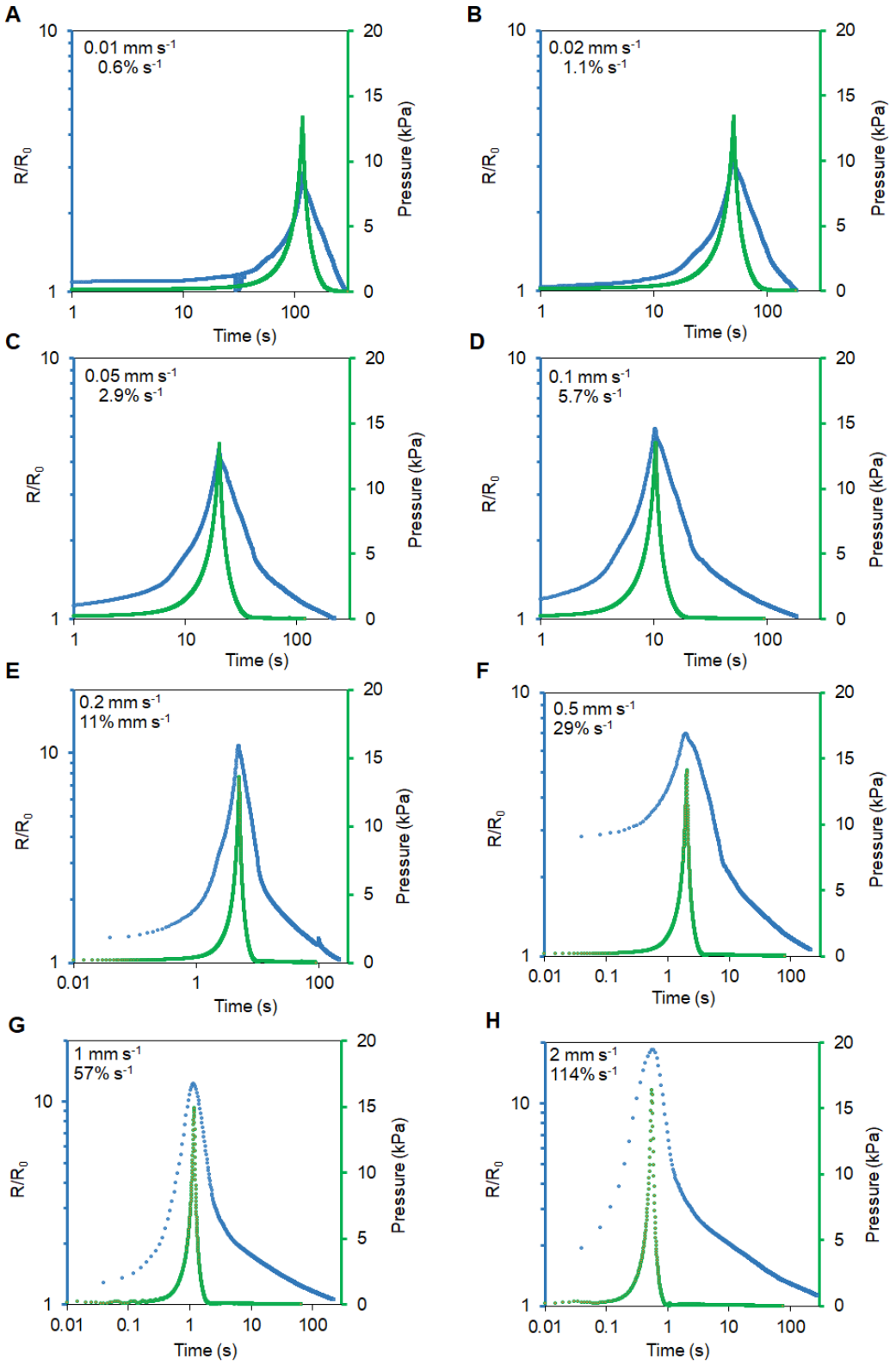

Figure 6.8: **Electrical response to applied pressure *vs* strain rate for 0.17 vol.% composite.** R/R_0 is plotted against time for an applied target pressure of 13.3 kPa (measured pressure presented on the secondary y-axis) at compressive strain rates between (0.6 - 114% s^{-1})

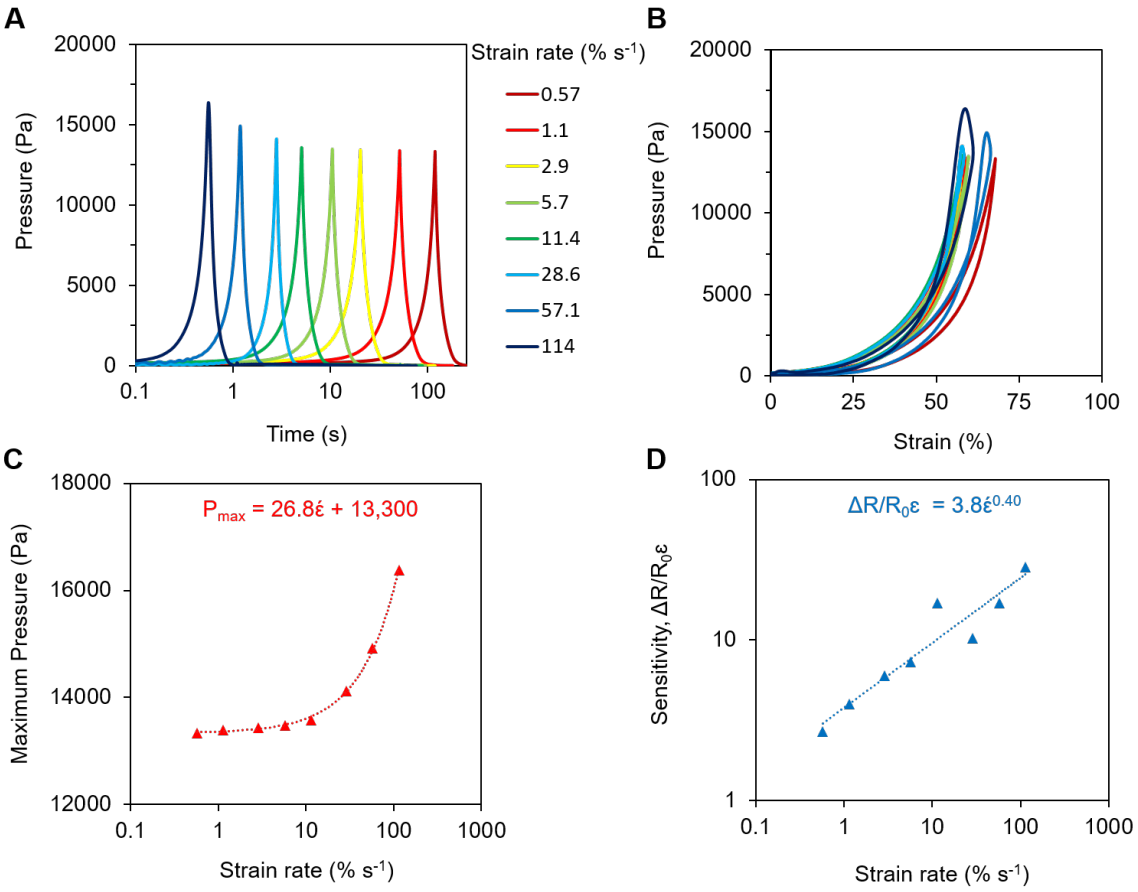

Figure 6.9: **Strain rate dependence for few-layer-graphene emulsion composites.** **A.** Pressure *vs* time profiles for (target) 13.3 kPa applied at increasing strain rates (0.01 - 2 Hz) **B.** Pressure *vs* strain for the profiles applied in A. **C.** Maximum pressure applied to the sample *vs* strain rate. **D.** Sensitivity $\Delta R/R_0\epsilon$ as a function of strain rate.

timescales invoke a stronger electrical response as the imparted stress does not have as much time to relax before the peak stress is reached, suggesting that these composites are more sensitive to high strain rates.

In Figure 6.9A, a summary of the pressure profiles applied is shown and colour coded for different strain rates. It can be seen from Figure 6.9B that the hysteresis is relatively low, indicative of sufficient pre-conditioning from initial tests of the system to determine the experimental protocol. The maximum pressure is shown in Figure 6.9C for reference,

and increases linearly with strain consistent with a constant compressive modulus, only becoming significant at strain rates above 20 % s^{-1}, partly due to strain stiffening. Since the maximum pressure increases while the compressive strain remains unchanged, it must be concluded that the electromechanical response depends in part on the stress imparted to the composite. Naturally for soft composites, one would expect an increase in relative resistance change with strain rate because of the time-dependent stress relaxation such materials exhibit. At the nanoscale, the reptation of polymer chains cause the polymer to behave like a liquid, [213] in which suspended nanosheets would be free to move and rotate according to the local environment. When stress builds in the composite, it is able to dissipate through the reptation of the polymer chains over time. If the stress is not allowed to release, as is the case during rapid compression, the weakly-interdiffused spheres oblate, increasing their surface area while reducing the inter-sheet connectivity, leading to a subsequent reduction in network conductivity. Indeed, the electromechanical response is well defined when normalised to strain, such that $R/R_0 = 3.8\dot{\epsilon}^{0.4}$ as shown in Figure 6.9D. This shows that these sensors are well suited to high-strain rate applications, over time scales in which the stress cannot dissipate.

6.7 Cycling Performance

To ascertain the cycling performance of the composites, 10 strain cycles on a 0.18 vol.% sample with increasing pressure ranging from 1 kPa to 270 kPa are performed. A typical mechanical response is shown in Figure 6.10A, where a clear decrease in mechanical hysteresis can be seen with increasing cycle number. The electrical response plotted in Figures 6.10B and 6.10C. The relative resistance change is taken between peak minima and maxima and plotted against the applied pressure for various cycle numbers in Figure 6.10D. Due to the range of pressures studied, $R_i/R_j - 1$ is plotted on a log axis where R_i and R_j represent the minimum and maximum resistance for a given cycle.

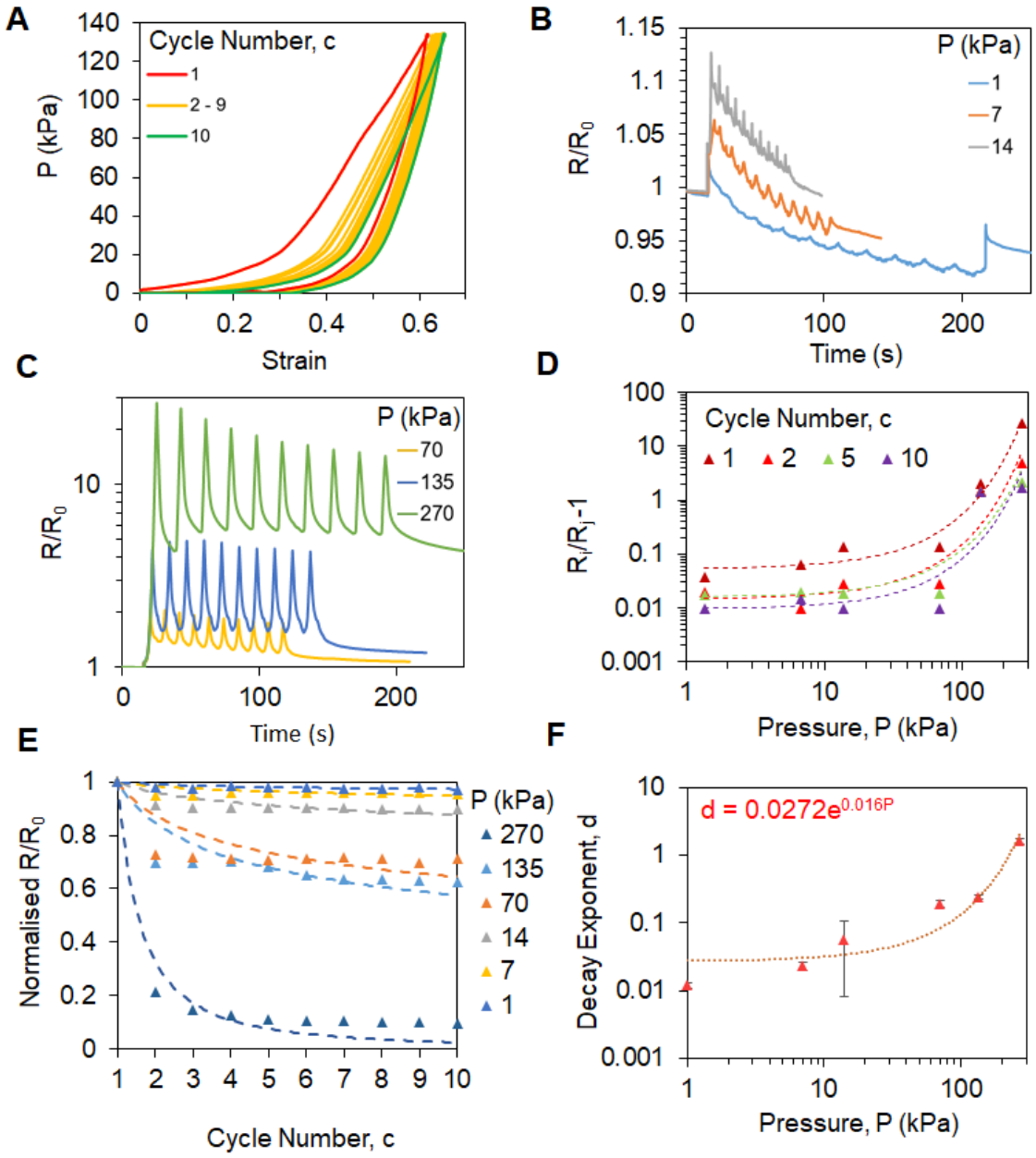

Figure 6.10: **Electrical response to cyclic pressure (1-270 kPa) for few-layer graphene emulsion composites. B.** R/R_0 for 10 cycles at 1, 7 and 14 kPa applied pressure (blue, orange and grey lines respectively). **C.** R/R_0 for 10 cycles at 70, 135 and 270 kPa (medium to high pressure, yellow, blue and green lines respectively.) **D.** R_i/R_j - 1 as a function of pressure, *i.e.* relative change in resistance for each peak. **E.** Normalised relative resistance change *vs* cycle number. **F.** Signal decay constant d (from $R/R_0 \propto c^d$) as a function of *vs* pressure.

Generally, there is a clear decrease in the sensitivity as a function of cycle number c. Signal fatigue is a well known but seldom discussed phenomenon in nanocomposite strain sensors. Recent analysis of the literature by Boland [43] has shown that many nanocomposite strain sensors exhibit a universal signal decay, in which R_i/R_j scales with $c^{-0.1}$. The decaying sensitivity is associated with the Mullin's effect, otherwise known as stress softening with cyclic strain. When subject to a cyclic strain with a constant maximum, it is well known that the induced stress in the material decays as a function of cycle number. In all experiments, a constant stress is applied which is equivalent to an increasing strain for stress softening materials under cyclic loading. By the logic presented in ref [43], this should eliminate the sensitivity decay seen in other sensors although this is not observed for this system. Indeed, normalising to the relative resistance change for the first cycle and plotting the subsequent decay in sensitivity in Figure 6.10E reveals a significant dependence on the magnitude of the applied pressure. Assuming the resistance decays as according to $R/R_0 \propto c^{-d}$, the decay exponent d exhibits an exponential dependence to the applied pressure P, according to $d = 0.0272e^{0.016P}$ as shown in Figure 6.10F. For pressures between 1-135 kPa, d takes values between 0.012 and 0.24, in close agreement with other sensors surveyed in the literature [43]. At 270 kPa, d is considerably higher than reported elsewhere, which may be indicative of sample damage with increasing cycles.

The significant change in resistivity between the first and second cycle can be explained by the templated nature of the conductive network. Mechanical stress leads to an irreversible deviation in the network structure away from the optimum formed during emulsification. Despite this, the scaling observed implies that a critical cycle number exists where the change in sensitivity becomes negligible between cycles, otherwise known as the endurance limit. [43]

6.8 Conclusion

An interesting consequence of the composite morphology is the electrical response to applied pressure. Analogously to the tensile strain sensors examined in Chapter 5, the piezoresistivity is exponentially dependent on applied pressure. This allows subtle pressures on the order of 1 kPa to be detected with high sensitivity ($\Delta R/R_0 = 0.038$ kPa^{-1}) and high pressures on the order of ∼500 kPa to be measured with sensitivities above 1000 kPa^{-1}, the largest reported to the best of this author's knowledge. Altogether, these results imply that the sensors can reliably detect pressures in the subtle pressure region (<1 kPa) through to the high pressure region (0.1 - 1 MPa). Thus, these sensors may find use in electronic skins as they are soft and flexible enough to conform to human skin, enable complete stress transfer, and remain comfortable. Moreover, these sensors remain sensitive over regions that a human is able to exert on its environment (up to 500 kPa), and are likely calibrable given sufficient pre-conditioning.

Chapter 7

Conclusions and Future Work

7.1 Conclusions

Nanocomposites sensors hold great promise for next generation sensors able to conform and comply with complex geometries, to any object and detect or measure a wide array of stimuli spanning orders of magnitude in strength, and with unparalleled sensitivity. [155] The performance of the composite depends on the constituent materials and their relative arrangement. [13] For graphene based composites, the simplest arrangement that can be achieved is that of randomly distributed nanosheet networks; with such systems having been studied extensively in the literature. In the context of sensing, silicone rubbers such as PDMS and Ecoflex are interesting matrix materials owing to their high deformability, strain range, elasticity and biocompatibility, making them particularly suited to human health and bodily monitoring applications. Graphene-silicone sensors have shown great promise, with random network composites exhibiting high sensitivity and enabling the detection of stimuli as subtle as the human heartbeat. [175] Further improvements to sensor performance may be realised in more advanced network morphologies. [38]

In this thesis, a framework has been developed that facilitates the production of advanced graphene silicone composites with structured nanosheet networks and tunable

mechanical properties. This is achieved by means of graphene-stabilised silicone emulsions. In Chapter 4, simple rules for emulsion orientation are detailed based on the surface energy of the oil, solid and water phases. The surface energy of the graphene stabiliser is then established based on the orientation transition point. The subsequent phase diagram that can be drawn allows us to predict how various combinations of oils (polymers and organic solvents) and waters (EG, DI water and combinations thereof) will emulsify with Elicarb graphene. Indeed, the emulsion orientation is an important consideration for composite production. W/o emulsions can be cured into sponges where voids are coated with graphene while o/w can produce loose coated spheres. By virtue of the orientation, w/o sponges have a continuous mechanically robust frame at the expense of a significant dielectric barrier between conducting elements. Without significant optimisation to reduce this potential barrier, such composites cannot be used for electromechanical sensing due to the obstructive sample resistivity. Conversely for o/w systems, mechanical robustness in tension is forgone in exchange for intimate contact between conducting spheres and the associated increase in inter-droplet junction conductivity. Thus, composites from o/w emulsions were pursued in light of the superior sensing capability.

A non-trivial relationship between composite morphology and emulsion curing parameters was observed. In particular, elastomeric samples with increasing tolerance to tensile strain emerged as the time between formation and curing increased. Initially this was unexpected, although further study of curing latex systems [202] revealed analogous behaviour in which the tensile strength of the latex film increased in line with the degree of polymer-chain diffusion into neighbouring latex spheres, albeit over much shorter timescales. A model was subsequently developed that accounted for the silicone polymer-chain mobility and the additional path length presented by the tortuosity of the graphene shell. The model describes the data well and can be easily extended to other polymer/layered material composite system with base assumptions on chain diffusivity and sheet morphology. By

elucidating the interdiffusion process, strategies to reduce the inter-diffusion time can be implemented - namely reducing the molecular weight of the polymer and/or the thickness of the graphene shell.

Most encouraging is the fact that tensile strength can be regained in time without sacrificing the network morphology and subsequent electrical properties. Chapter 5 explores the electromechanical properties of these mechanically robust, structured network composites and the influence of graphene content. When assessed against random network composites [161], a significant improvement to electrical conductivity spanning 7 orders of magnitude was found at the lowest loading level measured (5.6 vol%) in the Elicarb system. Graphene inclusion was shown to increase mechanical reinforcement linearly with loading level, with the highest loading level samples (16.5 vol%) providing the greatest degree of mechanical reinforcement. Relative to composites prepared at 0% graphene loading, the strongest graphene loaded composites (16.5 vol%) have a reduction in ultimate tensile strength of 36%, while the peak strain, toughness and Young's modulus increase by 13%, 19%, 62% respectively. Aside from the loss modulus, all electromechanical properties improve with increasing graphene content.

For electromechanical sensing, the electrical response to applied strain yields a consistent exponential increase in resistance that can be described using one parameter, defined in this thesis as the exponential gauge factor G_{exp}. As discussed at length in Boland [155], there is a lack of consistency in the literature in how researchers report strain (or pressure) sensor performance. The most stringent require the gauge factor to be defined over the initial linear region of $\Delta R/R_0\epsilon$. More frequently, a gauge factor will be quoted over the highest sensitivity region (particularly for sensors that deviate from linearity) as this will make the sensor appear more competitive with those in the literature. Although exponentials are linear to first order, a different view is adopted in this thesis, that is the electrical response must be well defined by a monotonic function. This ensures a sensor can be calibrated

and the stimuli measured. Adopting this approach enables a higher working range for many sensors and, in the case of exponentials is not entirely unprecedented, having been explained by the reduced inter-sheet tunnelling probability with strain. [175] [36] [214] [215]

That the electromechanical properties, in particular the conductivity and hence maximum $\Delta R/R_0$, toughness and working strain generally improve with graphene loading for the range studied suggests that improved sensor performance is attainable beyond 16.5 vol%. The insensitivity of G_{exp} to loading level simplifies the sensor calibration process. As with most if not all strain sensors in the literature [155], sensitivity decay with increasing cycle number is far from ideal considering most applications will require dynamic strain monitoring, and is seldom quantified in most publications.

Boland [155] attributes this behaviour to the Mullins effect or stress softening within a viscoelastic material. As an intrinsic property of many elastomers, the issues caused by the viscous component are difficult to avoid and so should be properly understood. Fortunately, Boland finds that a steady state can be achieved in which the decay in sensitivity can be ignored after a sufficient number of cycles, the so-called endurance limit. For the sensors presented herein, G_{exp} was found to decay to $\sim$4, independently of strain magnitude. This allows for recalibration and the accurate measurement of small (0.07%) and large (74%) strains applied cyclically.

Measurements taken in contexts specific to the human body (pulse, respiration, finger bending) can all be monitored with ease despite the differences in strain magnitude. An interesting consequence of the exponential scaling is the increased sensitivity at larger strain. This means that even smaller signals such as pulse can be seen clearly in the midst of larger strains from respiration. In all, the ultra-sensitivity, mechanical robustness and consistent performance of emulsion based composite strain sensors is attributed to the templated microstructure of the composites.

In Chapter 6, the focus shifts to the lightly interdiffused graphene coated spheres.

Aspects of the production process are simplified, including the removal of swelling solvents (DCM and EA) enabled by a shift to a lower molecular weight poly-silicone (Ecoflex 00-30) and the near-elimination of interdiffusion time. FLG produced in-house via homogenisation was used as the stabiliser to facilitate thinner shells and lower loading level composites. Taken together, these steps improve the scalability of the technique by lowering the production time, cost and demonstrate the robustness of the emulsification process to changes in materials.

Obviously, lightly interdiffused graphene coated spheres are unsuitable for tensile strain sensing. Therefore, their application as pressure sensors is assessed. As in Chapter 5, an exponential electrical response to applied pressure is observed. In this case, key sensor parameters including the working pressure P_w, strain ϵ_w, R/R_0 and sensitivity exponent G_{exp} are all affected by the graphene loading level.

7.2 Future Work

Sixteen years after it's isolation in 2004, a range of graphene related technologies are reaching maturity; with a variety of mechanically enhanced products available to purchase. Nanocomposite sensors however, are still relatively immature, and a healthy dose of scepticism leads one to question whether or not the issues facing these sensors can be overcome. Recent work by Boland has sought to bring order to the vastly different reporting standards and set requirements for the 'ideal' sensor. Indeed, an ideal sensor should exhibit a high sensitivity to strain (G $>$ 8) and have a high working range ($\epsilon_w \geq 100\%$). For on-skin applications, the sensor should be soft enough (<300 kPa) to be comfortable to wear and facilitate appropriate stress transfer between skin and sensor. [155]

In terms of sensitivity, the gauge factor ($\sim$20) of the elastomeric films in Chapter 5 is an order of magnitude higher than established technologies at low strain. The sensitivity increases exponentially with applied strain, which invites the prospect of pre-straining the

sensor to tune the gauge factor at the expense of maximum strain range for the application.

The working strain range of the most elastic sensors is ϵ_w >80%, while the Young's modulus E increases between 0.4 - 1.2 MPa. In order to meet the criteria set out by Boland, ϵ_w and E need to increase and decrease respectively. [43] This author believes that using a softer, more elastic poly-silicone such as Ecoflex 00-30 and FLG as a stabiliser could achieve both of these goals simultaneously. Further, the high interdiffusion time required for elastomeric composites (t_d >250 h) can be reduced by using FLG to reduce the shell thickness and hence tortuous path length, without significantly compromising the conductivity at lower loading levels. This is demonstrated in principle in Chapter 6, where such changes result in lightly interdiffused graphene coated spheres even for $t_d \approx 0h$.

As shown in Chapter 6, the exponential dependence on pressure is maintained despite the change in matrix and filler material. This shows that the electromechanical response is driven by the templated morphology of the network. To be truly usable as a sensor, this response must both be calibrable, i.e. well-defined by a monotonic function and also robust to a large number of cycles that would be unavoidable in real-world scenarios. It is encouraging then that such a single parameter function based on an exponential gauge factor is easily defined in these systems, and that signal decay present is similarly quantifiable and follows trends seen in the literature. [43] Once the endurance limit has been reached, a regular, repeatable response should be attainable.

Regardless of design complexity, there are a number of excellent examples of sensors that approach the concept of an ideal sensor. Whilst this author believes the sensors based on graphene stabilised emulsified silicones are truly competitive in terms of performance and potential, the production process is simple given the templated nature of the network. Simplicity keeps production costs low and elucidates avenues for improvement and further optimisation, ultimately enabling real-world applications.

Chapter 8

Experimental Methods: Appendix A

8.1 Chapter 4

To establish the phase inversion point in Figure 4.3 and plot the phase inversion boundary in Figure 4.5, 100 mg of graphene powder is added to 10 mL of ethyl acetate and bath sonicated. A mixture of EG:DI water is added in ratios ranging from 10:0 to 0:10 in 10 vol.% increments such that the water phase also totals 10 mL. The mixture is then shaken vigorously for 30 seconds and is characterised as o/w or w/o by the buoyancy of the droplet phase, as the water phase is denser than the oil phase.

To establish the droplet size dependence on graphene content, we opted for w/o emulsions as seen in Figure 4.4 and 4.6. This is because graphene has a surface energy between air and 'water' and will seek to stabilise that interface. This water-air interface is only present for oil in water emulsions and will lead to a continuous film of graphene at the surface, obscuring the contents below. For w/o emulsions however, hydrophobic containers must be used to prevent the droplets from bursting as the high surface tension water phase will seek to stabilise the even greater surface energy disparity between glass

and graphene. To ensure a w/o emulsion, the water phase consisted of 100% DI water, while the oil phase consisted of 1:1:2 PDMS:EA:DCM. 5 mg to 50 mg (in 5 mg increments) of graphene powder is weighed out into hydrophobic (silanised) glass vials before 0.5 mL of DI water is added and sonicated together. Next, 3.5 mL of the oil phase is added and the mixture is shaken vigorously. The newly formed emulsion is poured into a hydrophobic polytetrafluoroethylene (PTFE) cubic well 4 cm^3 in volume and images are taken under 10 $\times$ magnification. Using ImageJ software, 100 droplets are measured along their longest dimension for each sample, the average is taken and the standard error is calculated.

We used a Hansen parameter approach to identify co-solvents for graphene (Thomas Swan, Premium Elicarb graphene powder) and PDMS (Farnell UK, Qsil 216, 4500 mPa s). Dichloromethane (Sigma Aldrich, 1.325 g mL^{-1}, 0.413 mPa s at 25 °C) and ethyl acetate (Sigma Aldrich, 0.902 g mL^{-1}, 0.426 mPa s at 25 °C) were found to be capable of thinning the PDMS and dispersing pre-exfoliated graphene well enough to emulsify the oil-water mixture. We found that 2:1:1 parts DCM:EA:PDMS by volume offered a reasonable compromise towards matching the density of the oil and water phases, lowering the viscosity of the oil phase and maintaining an acceptable solids content.

The graphene powder used is a commercially available product, with the following taken from the datasheet: Average particle size distribution: $D_{10} = 1$ μm, $D_{50} = 4$ μm, $D_{90} = 10$ μm. Sheet resistance = typically $< 25\Omega/\square$ normalised to 25 μm. Surface area = approx., 50-100 m^2 g^{-1} (BET). D/G = <0.15 (very low defect material). Residue <1%. Surfactant <3%.

Graphene powder is added to DCM and bath sonicated (Grant XUB Bath Sonicator) at 10 °C for one hour before being added to the ethyl acetate-swelled PDMS and homogenised via vigorous shaking for 30 s. EG is then added such that the o:w ratio is 40:60 v/v before shear mixing (Silverson L5M-A) at 10,000 rpm for 2 minutes. The newly formed emulsions are re-sealed and allowed to interdiffuse for a time t_d before being re-shaken for 30 seconds

and poured into a glass petri dish. The emulsions are then placed in an oven at 30 °C for 1 hour before raising the temperature by 10 °C every hour until 70 °C is reached and subsequently maintained overnight, unless otherwise stated. This is to avoid turbulent boiling of DCM and EA from the PDMS when curing. The samples are removed from the oven and left to cool.

To determine the morphological time dependence of the composites and resulting electromechanical properties, 5 identical o/w emulsions were made using this method with $\phi = 7.3$ vol.%. They were each allowed to stand for 21 h to 501 h, before being poured into glass petri dishes and cured through incremental increases in temperature. Multiple (at least 6) strips are cut from each sample for statistical analysis, ranging between 5-7 mm wide and 25-30 mm long, individually measured by electronic calipers, with the height of each sample measured via an electronic micrometer screw-gauge for sub millimeter accuracy and precision. The ends of each strip are painted in silver and connected to a Keithley 2126B probe station capable of measuring picoamp currents. The conductivity of each sample is calculated from sample resistance and geometry, with the standard error derived in the usual way, according to $SE = \frac{\sigma}{\sqrt{n}}$, where σ here refers to the standard deviation and n the number of strips per sample. Each strip is then placed in the grips a mechanical stage (Texture Analyser, Stable Microsystems) and strained until failure. The raw force-distance curve is converted to a stress-strain curve using individual geometries and the standard error taken in a similar fashion.

Finally, SEM (Zeiss SIGMA field-emission gun SEM) microscopy and Raman spectroscopy (Renishaw inVia) microscopy is performed on stress-fractured cross-sections.

8.2 Chapter 5

To determine the effect of graphene content on composite electromechanical properties, 12 o/w emulsions are prepared at various loading levels between 0.5 and 16.5 vol.% as shown

in Figure 4.9. So as to ensure elastomeric composites, the samples are cast after ∼2500 h (107 days). At the time of casting, emulsions containing 2 vol.% of graphene or less had cured *in situ*, while $\phi = 3.8$ vol.% had partially cured. Conversely, for $\phi = 10.6$ vol.% , the aforementioned curing profile was insufficient to harden the composites likely due to reduced cross-link density near to the graphene network. For this reason, all samples with $\phi = 5.6$vol.% and above were held in the oven for an additional night at 70 °C.

Similarly to Chapter 4, multiple strips cut from each sample have their dimensions measured using electronic calipers and screw gauges. The ends of each sample are coated in silver paint to reduce contact resistance and subsequently placed in modified grips of a mechanical testing stage (Texture Analyser, Stable Microsystems). The grips were modified with sandpaper and tin-foil, attached via double sided sticky tape. Sand-paper is used to prevent current leakage between the Texture Analyser grips and the sample, while the tin foil enables a reliable electrical connection point for crocodile clips without compromising the mechanical integrity of the sample. Electrical conductivity is then measured using a Keithley 2126B probe station for sub-nano amp sensitivity and recorded over time as the sample is subjected to various tensile strain profiles in the mechanical stage.

Mechanical data is similarly extracted by converting the raw force-distance to stress-strain curve using individual strip geometries. The Young's Modulus in Figure 5.4 is calculated from the linear region of the stress strain curve, and taken at the point at which the curve deviates significantly from linearity (R^2 =0.99). Electrical data is extracted from the measured current and measured sample geometry to calculate sample conductivity, which would then vary under tensile strain. To calculate $DeltaR/R_0$, the initial resistance R_0 is identified by the local minima preceding the applied strain, which is very clearly visible. The maximum resistance is taken at the point at which a single parameter fit no longer applies with a high fidelity (R^2 >0.95), either because of a turning point (the sample is relaxed) or signal loss (the sample has failed). For cyclic strain tests, the resistance

cycles in tandem with the applied strain, verified by matching the respective periods of the applied strain waves and measured current waves, and the minimum and maximum resistances are taken as the local minimum and minimum of each current wave. The average exponent is plotted in 5.8 as a function of the graphene loading level. Subsequent strain sensing measurements are performed on the highest loading level samples, i.e $\phi =$ 16.5 vol.%, due to their superior conductivity and durability as discussed in the main text.

8.3 Chapter 6

As described in Large *et al.*, [90] a dispersion of highly concentrated graphite (60 g L^{-1}) in DI-water Triton X-100 solution (4 g L^{-1}) is passed through micro-channels at high pressures (∼30 kpsi). This induces significant shear forces on the graphite and facilitates delamination into few layer graphene nanosheets. The exfoliated dispersion undergoes two size selection steps via centrifugation (5 minutes at 200 g followed by 20 minutes at 5000 g). The final supernatant contains up to 1 g L^{-1} of FLG graphene sheets ($\langle N \rangle$ ∼5 layers). Graphene-coated silicone spheres are based on oil-in-water emulsions, which cannot be formed using DI water as discussed in Chapter 4. Instead, it is necessary to transfer the dispersed nanosheets into a lower surface tension phase such as EG. To achieve this, the supernatant is centrifuged at 5000 g for 16 hours to sediment the majority of the dispersed graphene. The supernatant is discarded along with any unbound surfactant and ethylene glycol is added to the sediment and re-dispersed via tip sonication at high concentration ∼3 g L^{-1} as shown in figure 6.1B, forming the master dispersion. This highly concentrated graphene-EG dispersion is increasingly diluted with additional EG such that the dispersion volume totals 6 mL. Then, 4 mL of Ecoflex 00-30 is prepared from a 2 part mix by stirring for about a minute before being added to each graphene-EG dispersion. The graphene loading level for each sample is then 0.03, 0.06, 0.09, 0.011, 0.14, 0.17 vol.% respectively. Each blend is immediately shear mixed at 10,000 rpm (Silverson L5M-A) for 2 minutes

and cast into a glass petri dish, having formed polymer emulsion. The samples are placed in a preheated oven at 70°C overnight, which is sufficient to cure the silicone spheres and remove the continuous EG phase.

UV-vis extinction spectroscopy is performed on the master solution diluted by a factor of 625x transferred to a disposable vial with a path length of 1 mm with EG used for reference. DLS (Anton Paar Litesizer 500) is performed 10 times in rapid succession using a a 658 nm laser excitation wavelength at 40 mW. Raman spectroscopy is performed using a 532 nm laser; through a 1800 mm^{-1} grating under a 20x objective at 10% power (3.5 mW) with an exposure time of 0.5 s and 1 μm step size. Optical microscopy is performed under 30x magnification using a generic microscope.

For the electromechanical measurements, $\sim$ 5-7 mm x 25-30 mm strips are cut from the as produced samples and placed on a glass substrate for electrical insulation between the sample and mechanical stage. As in Chapters 4 and 5, the ends of the sample are painted in silver and connected to a Keithley 2126B probe station for electrical characterisation. A 1x1 cm^2 glass slide is attached to the base of a smaller metallic compression probe (Texture Analyser, Stable Microsystems) via bluetack to enable an a pressure profile that spans the width of the sample under compression, ensuring that all conducting paths are subject to the designated pressure between the silver painted electrodes and that there is no possibility of electrical shorting through the metal probe. The force measured by the probe during compression is converted to pressure using the area of the sample under compression, while compressive strain is measured from the height of each sample and the compression distance. Analogously to Chapter 5, Electromechanical measurements are taken simultaneously for multiple strips per sample and combined to generate compressive strain sensitivity data with standard errors.

Bibliography

[1] Y. Zang, F. Zhang, C.-a. Di, and D. Zhu, "Advances of flexible pressure sensors toward artificial intelligence and health care applications," vol. 2, no. 2, pp. 140–156. [Online]. Available: http://xlink.rsc.org/?DOI=C4MH00147H 1, 21, 88

[2] K. S. Novoselov, "Electric Field Effect in Atomically Thin Carbon Films," vol. 306, no. 5696, pp. 666–669. [Online]. Available: https://www.sciencemag.org/lookup/doi/10.1126/science.1102896 1, 5, 6, 9

[3] K. S. Novoselov, A. K. Geim, S. V. Morozov, D. Jiang, M. I. Katsnelson, I. V. Grigorieva, S. V. Dubonos, and A. A. Firsov, "Two-dimensional gas of massless Dirac fermions in graphene," vol. 438, no. 7065, pp. 197–200. [Online]. Available: http://www.nature.com/articles/nature04233 1, 5, 7

[4] A. K. Geim and K. S. Novoselov, "The rise of graphene," vol. 6, no. 3, pp. 183–191. [Online]. Available: http://www.nature.com/articles/nmat1849 1, 5, 6, 7, 8

[5] A. C. Ferrari, F. Bonaccorso, V. Fal'ko, K. S. Novoselov, S. Roche, P. Bøggild, S. Borini, F. H. L. Koppens, V. Palermo, N. Pugno, J. A. Garrido, R. Sordan, A. Bianco, L. Ballerini, M. Prato, E. Lidorikis, J. Kivioja, C. Marinelli, T. Ryhänen, A. Morpurgo, J. N. Coleman, V. Nicolosi, L. Colombo, A. Fert, M. Garcia-Hernandez, A. Bachtold, G. F. Schneider, F. Guinea, C. Dekker, M. Barbone, Z. Sun, C. Galiotis, A. N. Grigorenko, G. Konstantatos, A. Kis, M. Katsnelson, L. Vandersypen,

A. Loiseau, V. Morandi, D. Neumaier, E. Treossi, V. Pellegrini, M. Polini, A. Tredicucci, G. M. Williams, B. Hee Hong, J.-H. Ahn, J. Min Kim, H. Zirath, B. J. van Wees, H. van der Zant, L. Occhipinti, A. Di Matteo, I. A. Kinloch, T. Seyller, E. Quesnel, X. Feng, K. Teo, N. Rupesinghe, P. Hakonen, S. R. T. Neil, Q. Tannock, T. Löfwander, and J. Kinaret, "Science and technology roadmap for graphene, related two-dimensional crystals, and hybrid systems," vol. 7, no. 11, pp. 4598–4810. [Online]. Available: http://xlink.rsc.org/?DOI=C4NR01600A 1, 8, 9

[6] V. Dhand, K. Y. Rhee, H. Ju Kim, and D. Ho Jung, "A Comprehensive Review of Graphene Nanocomposites: Research Status and Trends," vol. 2013, pp. 1–14. [Online]. Available: http://www.hindawi.com/journals/jnm/2013/763953/ 2

[7] R. M. Guedes, *Creep and Fatigue in Polymer Matrix Composites*. 2

[8] M. Moeller and K. Matyjaszewski, *Polymer Science*. Elsevier Science. [Online]. Available: http://public.ebookcentral.proquest.com/choice/publicfullrecord.aspx?p=934526 2

[9] J. Brandrup, E. H. Immergut, and E. A. Grulke, Eds., *Polymer Handbook, 4th Edition*, 4th ed. Wiley. 2

[10] A. Mata, A. J. Fleischman, and S. Roy, "Characterization of Polydimethylsiloxane (PDMS) Properties for Biomedical Micro/Nanosystems," vol. 7, no. 4, pp. 281–293. [Online]. Available: http://link.springer.com/10.1007/s10544-005-6070-2 2

[11] S. H. Tan, N.-T. Nguyen, Y. C. Chua, and T. G. Kang, "Oxygen plasma treatment for reducing hydrophobicity of a sealed polydimethylsiloxane microchannel," vol. 4, no. 3, p. 032204. [Online]. Available: http://aip.scitation.org/doi/10.1063/1.3466882 2

[12] H. Hillborg, J. Ankner, U. Gedde, G. Smith, H. Yasuda, and K. Wikström, "Crosslinked polydimethylsiloxane exposed to oxygen plasma studied by neutron reflectometry and other surface specific techniques," vol. 41, no. 18, pp. 6851–6863. [Online]. Available: https://linkinghub.elsevier.com/retrieve/pii/S0032386100000392 2

[13] A. J. Marsden, D. G. Papageorgiou, C. Vallés, A. Liscio, V. Palermo, M. A. Bissett, R. J. Young, and I. A. Kinloch, "Electrical percolation in graphene–polymer composites," vol. 5, no. 3, p. 032003. [Online]. Available: http://stacks.iop.org/2053-1583/5/i=3/a=032003?key=crossref.e9145bff745c6cf347c69e1b7777b62f 2, 3, 9, 12, 14, 16, 18, 97, 98, 108

[14] D. Stauffer and A. Aharony, *Introduction to Percolation Theory*, rev., 2nd ed ed. Taylor & Francis. 3, 13

[15] I. Jurewicz, P. Worajittiphon, A. A. K. King, P. J. Sellin, J. L. Keddie, and A. B. Dalton, "Locking Carbon Nanotubes in Confined Lattice Geometries - A Route to Low Percolation in Conducting Composites," vol. 115, no. 20, pp. 6395–6400. [Online]. Available: https://pubs.acs.org/doi/10.1021/jp111998p 3, 12, 13, 14, 15, 54

[16] B. Earp, J. Simpson, J. Phillips, D. Grbovic, S. Vidmar, J. McCarthy, and C. Luhrs, "Electrically Conductive CNT Composites at Loadings below Theoretical Percolation Values," vol. 9, no. 4, p. 491. [Online]. Available: https://www.mdpi.com/2079-4991/9/4/491 3, 13

[17] M. Mansor, S. Fadzullah, N. Masripan, G. Omar, and M. Akop, "Comparison Between Functionalized Graphene and Carbon Nanotubes," in *Functionalized Graphene Nanocomposites and Their Derivatives*. Elsevier, pp. 177–204. [Online]. Available: https://linkinghub.elsevier.com/retrieve/pii/B978012814548700009X 3

[18] D. Ponnamma, N. Ninan, and S. Thomas, "Carbon Nanotube Tube Filled Polymer Nanocomposites and Their Applications in Tissue Engineering," in *Applications of Nanomaterials*. Elsevier, pp. 391–414. [Online]. Available: https://linkinghub.elsevier.com/retrieve/pii/B9780081019719000144 3

[19] M. Loos, "Composites," in *Carbon Nanotube Reinforced Composites*. Elsevier, pp. 37–72. [Online]. Available: https://linkinghub.elsevier.com/retrieve/pii/B9781455731954000023 3

[20] A. Kausar and R. Taherian, "Electrical Conductivity in Polymer Composite Filled With Carbon Microfillers," in *Electrical Conductivity in Polymer-Based Composites: Experiments, Modelling and Applications*. Elsevier, pp. 19–40. [Online]. Available: https://linkinghub.elsevier.com/retrieve/pii/B9780128125410000021 3

[21] C. Wu, X. Huang, G. Wang, L. Lv, G. Chen, G. Li, and P. Jiang, "Highly Conductive Nanocomposites with Three-Dimensional, Compactly Interconnected Graphene Networks via a Self-Assembly Process," vol. 23, no. 4, pp. 506–513. [Online]. Available: http://doi.wiley.com/10.1002/adfm.201201231 3

[22] R. Taherian, "The Theory of Electrical Conductivity," in *Electrical Conductivity in Polymer-Based Composites: Experiments, Modelling and Applications*. Elsevier, pp. 1–18. [Online]. Available: https://linkinghub.elsevier.com/retrieve/pii/B978012812541000001X 3

[23] U. Khan, I. O'Connor, Y. K. Gun'ko, and J. N. Coleman, "The preparation of hybrid films of carbon nanotubes and nano-graphite/graphene with excellent mechanical and electrical properties," vol. 48, no. 10, pp. 2825–2830. [Online]. Available: https://linkinghub.elsevier.com/retrieve/pii/S0008622310002654 3

[24] J. Zhao, S. Pei, W. Ren, L. Gao, and H.-M. Cheng, "Efficient Preparation of Large-Area Graphene Oxide Sheets for Transparent Conductive Films," vol. 4, no. 9, pp. 5245–5252. [Online]. Available: https://pubs.acs.org/doi/10.1021/nn1015506 3

[25] B. Tang, G. Hu, H. Gao, and Z. Shi, "Three-dimensional graphene network assisted high performance dye sensitized solar cells," vol. 234, pp. 60–68. [Online]. Available: https://linkinghub.elsevier.com/retrieve/pii/S0378775313001870 3

[26] Z. Tu, J. Wang, C. Yu, H. Xiao, T. Jiang, Y. Yang, D. Shi, Y.-W. Mai, and R. K. Li, "A facile approach for preparation of polystyrene/graphene nanocomposites with ultra-low percolation threshold through an electrostatic assembly process," vol. 134, pp. 49–56. [Online]. Available: https://linkinghub.elsevier.com/retrieve/pii/S026635381630241X 3

[27] Y. V. Syurik, M. G. Ghislandi, E. E. Tkalya, G. Paterson, D. McGrouther, O. A. Ageev, and J. Loos, "Graphene Network Organisation in Conductive Polymer Composites," vol. 213, no. 12, pp. 1251–1258. [Online]. Available: http://doi.wiley.com/10.1002/macp.201200116 3

[28] Y. Zhan, M. Lavorgna, G. Buonocore, and H. Xia, "Enhancing electrical conductivity of rubber composites by constructing interconnected network of self-assembled graphene with latex mixing," vol. 22, no. 21, p. 10464. [Online]. Available: http://xlink.rsc.org/?DOI=c2jm31293j 3, 16

[29] J. W. Hu, M. W. Li, M. Q. Zhang, D. S. Xiao, G. S. Cheng, and M. Z. Rong, "Preparation of Binary Conductive Polymer Composites with Very Low Percolation Threshold by Latex Blending," vol. 24, no. 15, pp. 889–893. [Online]. Available: http://doi.wiley.com/10.1002/marc.200300014 3, 13, 16

[30] T. D. Dao, G. Erdenedelger, and H. M. Jeong, "Water-dispersible graphene designed as a Pickering stabilizer for the suspension polymerization of poly(methyl methacrylate)/graphene core–shell microsphere exhibiting ultra-low percolation threshold of electrical conductivity," vol. 55, no. 18, pp. 4709–4719. [Online]. Available: https://linkinghub.elsevier.com/retrieve/pii/S0032386114006442 3, 13

[31] S. A. Ju, K. Kim, J.-H. Kim, and S.-S. Lee, "Graphene-Wrapped Hybrid Spheres of Electrical Conductivity," vol. 3, no. 8, pp. 2904–2911. [Online]. Available: https://pubs.acs.org/doi/10.1021/am200056t 3

[32] N. Yousefi, M. M. Gudarzi, Q. Zheng, S. H. Aboutalebi, F. Sharif, and J.-K. Kim, "Self-alignment and high electrical conductivity of ultralarge graphene oxide–polyurethane nanocomposites," vol. 22, no. 25, p. 12709. [Online]. Available: http://xlink.rsc.org/?DOI=c2jm30590a 3

[33] C. Gao, S. Zhang, F. Wang, B. Wen, C. Han, Y. Ding, and M. Yang, "Graphene Networks with Low Percolation Threshold in ABS Nanocomposites: Selective Localization and Electrical and Rheological Properties," vol. 6, no. 15, pp. 12 252–12 260. [Online]. Available: https://pubs.acs.org/doi/10.1021/am501843s 3, 13

[34] H. Deng, L. Lin, M. Ji, S. Zhang, M. Yang, and Q. Fu, "Progress on the morphological control of conductive network in conductive polymer composites and the use as electroactive multifunctional materials," vol. 39, no. 4, pp. 627–655. [Online]. Available: https://linkinghub.elsevier.com/retrieve/pii/S0079670013000877 3

[35] Y. Yu, G. Song, and L. Sun, "Determinant role of tunneling resistance in electrical conductivity of polymer composites reinforced by well dispersed

carbon nanotubes," vol. 108, no. 8, p. 084319. [Online]. Available: http://aip.scitation.org/doi/10.1063/1.3499628 3

[36] R. Zhang, M. Baxendale, and T. Peijs, "Universal resistivity–strain dependence of carbon nanotube/polymer composites," vol. 76, no. 19, p. 195433. [Online]. Available: https://link.aps.org/doi/10.1103/PhysRevB.76.195433 3, 74, 80, 111

[37] E. Roh, B.-U. Hwang, D. Kim, B.-Y. Kim, and N.-E. Lee, "Stretchable, Transparent, Ultrasensitive, and Patchable Strain Sensor for Human–Machine Interfaces Comprising a Nanohybrid of Carbon Nanotubes and Conductive Elastomers," vol. 9, no. 6, pp. 6252–6261. [Online]. Available: https://pubs.acs.org/doi/10.1021/acsnano.5b01613 3, 23, 74, 76

[38] M. Amjadi, K.-U. Kyung, I. Park, and M. Sitti, "Stretchable, Skin-Mountable, and Wearable Strain Sensors and Their Potential Applications: A Review," vol. 26, no. 11, pp. 1678–1698. [Online]. Available: http://doi.wiley.com/10.1002/adfm.201504755 3, 20, 108

[39] X. Li, R. Zhang, W. Yu, K. Wang, J. Wei, D. Wu, A. Cao, Z. Li, Y. Cheng, Q. Zheng, R. S. Ruoff, and H. Zhu, "Stretchable and highly sensitive graphene-on-polymer strain sensors," vol. 2, no. 1, p. 870. [Online]. Available: http://www.nature.com/articles/srep00870 3, 23, 74, 76

[40] M. Zhang, C. Wang, Q. Wang, M. Jian, and Y. Zhang, "Sheath–Core Graphite/Silk Fiber Made by Dry-Meyer-Rod-Coating for Wearable Strain Sensors," vol. 8, no. 32, pp. 20 894–20 899. [Online]. Available: https://pubs.acs.org/doi/10.1021/acsami.6b06984 3, 4, 23, 74, 76

[41] C. S. Boland, U. Khan, G. Ryan, S. Barwich, R. Charifou, A. Harvey, C. Backes, Z. Li, M. S. Ferreira, M. E. Mobius, R. J. Young, and J. N.

Coleman, “Sensitive electromechanical sensors using viscoelastic graphene-polymer nanocomposites,” vol. 354, no. 6317, pp. 1257–1260. [Online]. Available: https://www.sciencemag.org/lookup/doi/10.1126/science.aag2879 3, 13, 14, 15, 17, 21, 65, 68, 69, 70, 87, 97, 100

[42] H. Tian, Y. Shu, Y.-L. Cui, W.-T. Mi, Y. Yang, D. Xie, and T.-L. Ren, “Scalable fabrication of high-performance and flexible graphene strain sensors,” vol. 6, no. 2, pp. 699–705. [Online]. Available: http://xlink.rsc.org/?DOI=C3NR04521H 3, 23, 74, 76

[43] C. S. Boland, “Quantifying the Contributing Factors toward Signal Fatigue in Nanocomposite Strain Sensors,” vol. 2, no. 8, pp. 3474–3480. [Online]. Available: https://pubs.acs.org/doi/10.1021/acsapm.0c00510 3, 77, 80, 106, 113

[44] S. Chen, Z. Lou, D. Chen, K. Jiang, and G. Shen, “Polymer-Enhanced Highly Stretchable Conductive Fiber Strain Sensor Used for Electronic Data Gloves,” vol. 1, no. 7, p. 1600136. [Online]. Available: http://doi.wiley.com/10.1002/admt.201600136 3, 23, 74, 76

[45] C. Yan, J. Wang, W. Kang, M. Cui, X. Wang, C. Y. Foo, K. J. Chee, and P. S. Lee, “Highly stretchable piezoresistive graphene–nanocellulose nanopaper for strain sensors,” vol. 26, no. 13, pp. 2022–2027. 3, 23, 74, 76

[46] Z. Tang, S. Jia, F. Wang, C. Bian, Y. Chen, Y. Wang, and B. Li, “Highly Stretchable Core–Sheath Fibers via Wet-Spinning for Wearable Strain Sensors,” vol. 10, no. 7, pp. 6624–6635. [Online]. Available: https://pubs.acs.org/doi/10.1021/acsami.7b18677 3, 23, 72, 74, 76

[47] Y. R. Jeong, H. Park, S. W. Jin, S. Y. Hong, S.-S. Lee, and J. S. Ha, “Highly stretchable and sensitive strain sensors using fragmentized graphene foam,” vol. 25,

no. 27, pp. 4228–4236. 3, 23, 74, 76

[48] M. Amjadi, A. Pichitpajongkit, S. Lee, S. Ryu, and I. Park, "Highly stretchable and sensitive strain sensor based on silver nanowire–elastomer nanocomposite," vol. 8, no. 5, pp. 5154–5163. 3, 23, 72, 74, 76

[49] G. Shi, Z. Zhao, J.-H. Pai, I. Lee, L. Zhang, C. Stevenson, K. Ishara, R. Zhang, H. Zhu, and J. Ma, "Highly Sensitive, Wearable, Durable Strain Sensors and Stretchable Conductors Using Graphene/Silicon Rubber Composites," vol. 26, no. 42, pp. 7614–7625. [Online]. Available: http://doi.wiley.com/10.1002/adfm.201602619 3, 23, 74, 76

[50] N. Lu, C. Lu, S. Yang, and J. Rogers, "Highly Sensitive Skin-Mountable Strain Gauges Based Entirely on Elastomers," vol. 22, no. 19, pp. 4044–4050. [Online]. Available: http://doi.wiley.com/10.1002/adfm.201200498 3, 23, 74, 76

[51] K. K. Kim, S. Hong, H. M. Cho, J. Lee, Y. D. Suh, J. Ham, and S. H. Ko, "Highly sensitive and stretchable multidimensional strain sensor with prestrained anisotropic metal nanowire percolation networks," vol. 15, no. 8, pp. 5240–5247. 3, 13, 23, 74, 76

[52] H. Yang, X. Yao, Z. Zheng, L. Gong, L. Yuan, Y. Yuan, and Y. Liu, "Highly sensitive and stretchable graphene-silicone rubber composites for strain sensing," vol. 167, pp. 371–378. [Online]. Available: https://linkinghub.elsevier.com/retrieve/pii/S0266353818304378 3, 17, 21, 87

[53] C. Lee, L. Jug, and E. Meng, "High strain biocompatible polydimethylsiloxane-based conductive graphene and multiwalled carbon nanotube nanocomposite strain sensors," vol. 102, no. 18, p. 183511. [Online]. Available: http://aip.scitation.org/doi/10.1063/1.4804580 3, 23, 74, 76

[54] D. Niu, W. Jiang, G. Ye, K. Wang, L. Yin, Y. Shi, B. Chen, F. Luo, and H. Liu, "Graphene-elastomer nanocomposites based flexible piezoresistive sensors for strain and pressure detection," vol. 102, pp. 92–99. [Online]. Available: https://linkinghub.elsevier.com/retrieve/pii/S0025540817341910 3, 87

[55] J. T. Muth, D. M. Vogt, R. L. Truby, Y. Mengüç, D. B. Kolesky, R. J. Wood, and J. A. Lewis, "Embedded 3D Printing of Strain Sensors within Highly Stretchable Elastomers," vol. 26, no. 36, pp. 6307–6312. [Online]. Available: http://doi.wiley.com/10.1002/adma.201400334 3, 23, 74, 76

[56] T. Yamada, Y. Hayamizu, Y. Yamamoto, Y. Yomogida, A. Izadi-Najafabadi, D. N. Futaba, and K. Hata, "A stretchable carbon nanotube strain sensor for human-motion detection," vol. 6, no. 5, pp. 296–301. [Online]. Available: http://www.nature.com/articles/nnano.2011.36 3, 23, 74, 76

[57] N. Luo, Y. Huang, J. Liu, S.-C. Chen, C. P. Wong, and N. Zhao, "Hollow-Structured Graphene-Silicone-Composite-Based Piezoresistive Sensors: Decoupled Property Tuning and Bending Reliability," vol. 29, no. 40, p. 1702675. [Online]. Available: http://doi.wiley.com/10.1002/adma.201702675 4, 87

[58] J. N. Coleman, "Liquid Exfoliation of Defect-Free Graphene," vol. 46, no. 1, pp. 14–22. [Online]. Available: https://pubs.acs.org/doi/10.1021/ar300009f 6, 9, 10, 11, 13, 15, 16, 43, 52

[59] C. Backes, B. M. Szydłowska, A. Harvey, S. Yuan, V. Vega-Mayoral, B. R. Davies, P.-l. Zhao, D. Hanlon, E. J. G. Santos, M. I. Katsnelson, W. J. Blau, C. Gadermaier, and J. N. Coleman, "Production of Highly Monolayer Enriched Dispersions of Liquid-Exfoliated Nanosheets by Liquid Cascade Centrifugation," vol. 10, no. 1, pp. 1589–1601. [Online]. Available: https://pubs.acs.org/doi/10.1021/acsnano.5b07228 6, 10, 11, 33

[60] A. E. Del Rio Castillo, V. Pellegrini, A. Ansaldo, F. Ricciardella, H. Sun, L. Marasco, J. Buha, Z. Dang, L. Gagliani, E. Lago, N. Curreli, S. Gentiluomo, F. Palazon, M. Prato, R. Oropesa-Nuñez, P. S. Toth, E. Mantero, M. Crugliano, A. Gamucci, A. Tomadin, M. Polini, and F. Bonaccorso, "High-yield production of 2D crystals by wet-jet milling," vol. 5, no. 5, pp. 890–904. [Online]. Available: http://xlink.rsc.org/?DOI=C8MH00487K 6, 10

[61] C. Soldano, A. Mahmood, and E. Dujardin, "Production, properties and potential of graphene," vol. 48, no. 8, pp. 2127–2150. [Online]. Available: https://linkinghub.elsevier.com/retrieve/pii/S0008622310000928 6

[62] D. Abergel, V. Apalkov, J. Berashevich, K. Ziegler, and T. Chakraborty, "Properties of graphene: A theoretical perspective," vol. 59, no. 4, pp. 261–482. [Online]. Available: https://www.tandfonline.com/doi/full/10.1080/00018732.2010.487978 6

[63] K. F. Mak, M. Y. Sfeir, Y. Wu, C. H. Lui, J. A. Misewich, and T. F. Heinz, "Measurement of the Optical Conductivity of Graphene," vol. 101, no. 19, p. 196405. [Online]. Available: https://link.aps.org/doi/10.1103/PhysRevLett.101.196405 6

[64] A. A. Balandin, S. Ghosh, W. Bao, I. Calizo, D. Teweldebrhan, F. Miao, and C. N. Lau, "Superior Thermal Conductivity of Single-Layer Graphene," vol. 8, no. 3, pp. 902–907. [Online]. Available: https://pubs.acs.org/doi/10.1021/nl0731872 6

[65] S. Gadipelli and Z. X. Guo, "Graphene-based materials: Synthesis and gas sorption, storage and separation," vol. 69, pp. 1–60. [Online]. Available: https://linkinghub.elsevier.com/retrieve/pii/S0079642514000784 6

[66] A. H. Castro Neto, F. Guinea, N. M. R. Peres, K. S. Novoselov, and A. K. Geim, "The electronic properties of graphene," vol. 81, no. 1, pp. 109–162. [Online]. Available: https://link.aps.org/doi/10.1103/RevModPhys.81.109 6, 8

[67] M. Sprinkle, D. Siegel, Y. Hu, J. Hicks, A. Tejeda, A. Taleb-Ibrahimi, P. Le Fèvre, F. Bertran, S. Vizzini, H. Enriquez, S. Chiang, P. Soukiassian, C. Berger, W. A. de Heer, A. Lanzara, and E. H. Conrad, "First Direct Observation of a Nearly Ideal Graphene Band Structure," vol. 103, no. 22, p. 226803. [Online]. Available: https://link.aps.org/doi/10.1103/PhysRevLett.103.226803 6

[68] J. Wang, F. Ma, W. Liang, and M. Sun, "Electrical properties and applications of graphene, hexagonal boron nitride (h-BN), and graphene/h-BN heterostructures," vol. 2, pp. 6–34. [Online]. Available: https://linkinghub.elsevier.com/retrieve/pii/S2542529317300597 7

[69] K. Bolotin, K. Sikes, Z. Jiang, M. Klima, G. Fudenberg, J. Hone, P. Kim, and H. Stormer, "Ultrahigh electron mobility in suspended graphene," vol. 146, no. 9-10, pp. 351–355. [Online]. Available: https://linkinghub.elsevier.com/retrieve/pii/S0038109808001178 7

[70] S. V. Morozov, K. S. Novoselov, M. I. Katsnelson, F. Schedin, D. C. Elias, J. A. Jaszczak, and A. K. Geim, "Giant Intrinsic Carrier Mobilities in Graphene and Its Bilayer," vol. 100, no. 1, p. 016602. [Online]. Available: https://link.aps.org/doi/10.1103/PhysRevLett.100.016602 7

[71] F. Schwierz, "Graphene transistors," vol. 5, no. 7, pp. 487–496. [Online]. Available: http://www.nature.com/articles/nnano.2010.89 7

[72] A. K. Geim, "Graphene: Status and Prospects," vol. 324, no. 5934, pp. 1530–1534. [Online]. Available: https://www.sciencemag.org/lookup/doi/10.1126/science.1158877 8

[73] C. Lee, X. Wei, J. W. Kysar, and J. Hone, "Measurement of the Elastic Properties and Intrinsic Strength of Monolayer Graphene," vol. 321, no. 5887, pp. 385–388. [Online].

Available: https://www.sciencemag.org/lookup/doi/10.1126/science.1157996 8

[74] D. G. Papageorgiou, I. A. Kinloch, and R. J. Young, "Mechanical properties of graphene and graphene-based nanocomposites," vol. 90, pp. 75–127. [Online]. Available: https://linkinghub.elsevier.com/retrieve/pii/S0079642517300968 8

[75] A. Zurutuza and C. Marinelli, "Challenges and opportunities in graphene commercialization," vol. 9, no. 10, pp. 730–734. [Online]. Available: http://www.nature.com/articles/nnano.2014.225 8

[76] C. H. A. Tsang, H. Huang, J. Xuan, H. Wang, and D. Leung, "Graphene materials in green energy applications: Recent development and future perspective," vol. 120, p. 109656. [Online]. Available: https://linkinghub.elsevier.com/retrieve/pii/S1364032119308627 9

[77] J. Yang, P. Hu, and G. Yu, "Perspective of graphene-based electronic devices: Graphene synthesis and diverse applications," vol. 7, no. 2, p. 020901. [Online]. Available: http://aip.scitation.org/doi/10.1063/1.5054823 9

[78] M. Garcia-Hernandez and J. Coleman, "Materials science of graphene: A flagship perspective," vol. 3, no. 1, p. 010401. [Online]. Available: https://iopscience.iop.org/article/10.1088/2053-1583/3/1/010401 9

[79] C. Mattevi, H. Kim, and M. Chhowalla, "A review of chemical vapour deposition of graphene on copper," vol. 21, no. 10, pp. 3324–3334. [Online]. Available: http://xlink.rsc.org/?DOI=C0JM02126A 9

[80] S. Bae, H. Kim, Y. Lee, X. Xu, J.-S. Park, Y. Zheng, J. Balakrishnan, T. Lei, H. Ri Kim, Y. I. Song, Y.-J. Kim, K. S. Kim, B. Özyilmaz, J.-H. Ahn, B. H. Hong, and S. Iijima, "Roll-to-roll production of 30-inch graphene

films for transparent electrodes," vol. 5, no. 8, pp. 574–578. [Online]. Available: http://www.nature.com/articles/nnano.2010.132 9

[81] J. N. Coleman, M. Lotya, A. O'Neill, S. D. Bergin, P. J. King, U. Khan, K. Young, A. Gaucher, S. De, R. J. Smith, I. V. Shvets, S. K. Arora, G. Stanton, H.-Y. Kim, K. Lee, G. T. Kim, G. S. Duesberg, T. Hallam, J. J. Boland, J. J. Wang, J. F. Donegan, J. C. Grunlan, G. Moriarty, A. Shmeliov, R. J. Nicholls, J. M. Perkins, E. M. Grieveson, K. Theuwissen, D. W. McComb, P. D. Nellist, and V. Nicolosi, "Two-Dimensional Nanosheets Produced by Liquid Exfoliation of Layered Materials," vol. 331, no. 6017, pp. 568–571. [Online]. Available: https://www.sciencemag.org/lookup/doi/10.1126/science.1194975 10

[82] C. Backes, R. J. Smith, N. McEvoy, N. C. Berner, D. McCloskey, H. C. Nerl, A. O'Neill, P. J. King, T. Higgins, D. Hanlon, N. Scheuschner, J. Maultzsch, L. Houben, G. S. Duesberg, J. F. Donegan, V. Nicolosi, and J. N. Coleman, "Edge and confinement effects allow in situ measurement of size and thickness of liquid-exfoliated nanosheets," vol. 5, no. 1, p. 4576. [Online]. Available: http://www.nature.com/articles/ncomms5576 10, 28, 29, 33

[83] C. Backes, D. Campi, B. M. Szydlowska, K. Synnatschke, E. Ojala, F. Rashvand, A. Harvey, A. Griffin, Z. Sofer, N. Marzari, J. N. Coleman, and D. D. O'Regan, "Equipartition of Energy Defines the Size–Thickness Relationship in Liquid-Exfoliated Nanosheets," vol. 13, no. 6, pp. 7050–7061. [Online]. Available: https://pubs.acs.org/doi/10.1021/acsnano.9b02234 10, 11, 33

[84] C. Backes, T. M. Higgins, A. Kelly, C. Boland, A. Harvey, D. Hanlon, and J. N. Coleman, "Guidelines for Exfoliation, Characterization and Processing of Layered Materials Produced by Liquid Exfoliation," vol. 29, no. 1, pp. 243–255. [Online]. Available: https://pubs.acs.org/doi/10.1021/acs.chemmater.6b03335 10, 33

[85] C. Backes, K. R. Paton, D. Hanlon, S. Yuan, M. I. Katsnelson, J. Houston, R. J. Smith, D. McCloskey, J. F. Donegan, and J. N. Coleman, "Spectroscopic metrics allow in situ measurement of mean size and thickness of liquid-exfoliated few-layer graphene nanosheets," vol. 8, no. 7, pp. 4311–4323. [Online]. Available: http://xlink.rsc.org/?DOI=C5NR08047A 10, 28, 29, 30, 33, 91, 92, 93

[86] K. R. Paton, E. Varrla, C. Backes, R. J. Smith, U. Khan, A. O'Neill, C. Boland, M. Lotya, O. M. Istrate, P. King, T. Higgins, S. Barwich, P. May, P. Puczkarski, I. Ahmed, M. Moebius, H. Pettersson, E. Long, J. Coelho, S. E. O'Brien, E. K. McGuire, B. M. Sanchez, G. S. Duesberg, N. McEvoy, T. J. Pennycook, C. Downing, A. Crossley, V. Nicolosi, and J. N. Coleman, "Scalable production of large quantities of defect-free few-layer graphene by shear exfoliation in liquids," vol. 13, no. 6, pp. 624–630. [Online]. Available: http://www.nature.com/articles/nmat3944 10, 11, 12, 13, 14

[87] P. G. Karagiannidis, S. A. Hodge, L. Lombardi, F. Tomarchio, N. Decorde, S. Milana, I. Goykhman, Y. Su, S. V. Mesite, D. N. Johnstone, R. K. Leary, P. A. Midgley, N. M. Pugno, F. Torrisi, and A. C. Ferrari, "Microfluidization of Graphite and Formulation of Graphene-Based Conductive Inks," vol. 11, no. 3, pp. 2742–2755. [Online]. Available: https://pubs.acs.org/doi/10.1021/acsnano.6b07735 10

[88] R. J. Smith, P. J. King, M. Lotya, C. Wirtz, U. Khan, S. De, A. O'Neill, G. S. Duesberg, J. C. Grunlan, G. Moriarty, J. Chen, J. Wang, A. I. Minett, V. Nicolosi, and J. N. Coleman, "Large-Scale Exfoliation of Inorganic Layered Compounds in Aqueous Surfactant Solutions," vol. 23, no. 34, pp. 3944–3948. [Online]. Available: http://doi.wiley.com/10.1002/adma.201102584 10, 11

[89] M. Lotya, P. J. King, U. Khan, S. De, and J. N. Coleman, "High-Concentration, Surfactant-Stabilized Graphene Dispersions," vol. 4, no. 6, pp. 3155–3162. [Online].

Available: https://pubs.acs.org/doi/10.1021/nn1005304 10, 11

[90] M. J. Large, S. P. Ogilvie, A. Amorim Graf, P. J. Lynch, M. A. O'Mara, T. Waters, I. Jurewicz, J. P. Salvage, and A. B. Dalton, "Large-Scale Surfactant Exfoliation of Graphene and Conductivity-Optimized Graphite Enabling Wireless Connectivity," vol. 5, no. 7, p. 2000284. [Online]. Available: https://onlinelibrary.wiley.com/doi/abs/10.1002/admt.202000284 10, 12, 88, 118

[91] Y. Hernandez, M. Lotya, D. Rickard, S. D. Bergin, and J. N. Coleman, "Measurement of Multicomponent Solubility Parameters for Graphene Facilitates Solvent Discovery," vol. 26, no. 5, pp. 3208–3213. [Online]. Available: https://pubs.acs.org/doi/10.1021/la903188a 10, 13

[92] M. Lotya, Y. Hernandez, P. J. King, R. J. Smith, V. Nicolosi, L. S. Karlsson, F. M. Blighe, S. De, Z. Wang, I. T. McGovern, G. S. Duesberg, and J. N. Coleman, "Liquid Phase Production of Graphene by Exfoliation of Graphite in Surfactant/Water Solutions," vol. 131, no. 10, pp. 3611–3620. [Online]. Available: https://pubs.acs.org/doi/10.1021/ja807449u 11

[93] R. J. Smith, M. Lotya, and J. N. Coleman, "The importance of repulsive potential barriers for the dispersion of graphene using surfactants," vol. 12, no. 12, p. 125008. [Online]. Available: https://iopscience.iop.org/article/10.1088/1367-2630/12/12/125008 11

[94] A. Payne and R. Whittaker, "Reinforcement of rubber with carbon black," vol. 1, no. 4, pp. 203–214. [Online]. Available: https://linkinghub.elsevier.com/retrieve/pii/0010436170900054 12

[95] G. Yang, R. Teng, and P. Xiao, "Electrical properties of crosslinked polyethylene/carbon black switching composites as a function of morphology and

structure of the carbon black," vol. 18, no. 4, pp. 477–483. [Online]. Available: http://doi.wiley.com/10.1002/pc.10299 12

[96] J. Feng, "Carbon black (CB)-filled conductive polymer composites : CB distribution and electrical properties," p. b691220. [Online]. Available: http://lbezone.ust.hk/bib/b691220 12

[97] T. Noguchi, T. Nagai, and J. Seto, "Melt viscosity and electrical conductivity of carbon black-PVC composite: CARBON BLACK-PVC COMPOSITES," vol. 31, no. 6, pp. 1913–1924. [Online]. Available: http://doi.wiley.com/10.1002/app.1986.070310632 12

[98] A. Kato, Y. Ikeda, and S. Kohjiya, "Carbon Black-Filled Natural Rubber Composites: Physical Chemistry and Reinforcing Mechanism," in *Polymer Composites*, S. Thomas, J. Kuruvilla, S. K. Malhotra, K. Goda, and M. S. Sreekala, Eds. Wiley-VCH Verlag GmbH & Co. KGaA, pp. 515–543. [Online]. Available: http://doi.wiley.com/10.1002/9783527645213.ch17 12

[99] S. Wang, P. Wang, and T. Ding, "Resistive viscoelasticity of silicone rubber/carbon black composite," vol. 32, no. 1, pp. 29–35. [Online]. Available: http://doi.wiley.com/10.1002/pc.21012 12

[100] "The fracture energy of hybrid carbon and glass fibre composites," vol. 10, no. 3, p. 182. [Online]. Available: https://linkinghub.elsevier.com/retrieve/pii/0010436179903288 12

[101] A. Bunsell and B. Harris, "Hybrid carbon and glass fibre composites," vol. 5, no. 4, pp. 157–164. [Online]. Available: https://linkinghub.elsevier.com/retrieve/pii/0010436174901074 12

[102] M. Miwa and N. Horiba, "Effects of fibre length on tensile strength of carbon/glass fibre hybrid composites," vol. 29, no. 4, pp. 973–977. [Online]. Available: http://link.springer.com/10.1007/BF00351419 12

[103] J. Summerscales and D. Short, "Carbon fibre and glass fibre hybrid reinforced plastics," vol. 9, no. 3, pp. 157–166. [Online]. Available: https://linkinghub.elsevier.com/retrieve/pii/0010436178903415 12

[104] J. M. Scott and D. C. Phillips, "Carbon fibre composites with rubber toughened matrices," vol. 10, no. 4, pp. 551–562. [Online]. Available: http://link.springer.com/10.1007/BF00566560 12

[105] F. Nanni and M. Valentini, "Electromagnetic properties of polymer–carbon nanotube composites," in *Polymer–Carbon Nanotube Composites*. Elsevier, pp. 329–346. [Online]. Available: https://linkinghub.elsevier.com/retrieve/pii/B9781845697617500113 12

[106] T. Mcnally and P. Pötschke, "Introduction to polymer–carbon nanotube composites," in *Polymer–Carbon Nanotube Composites*. Elsevier, pp. xxi–xxvii. [Online]. Available: https://linkinghub.elsevier.com/retrieve/pii/B9781845697617500290 12

[107] G. Odegard, "Multiscale modeling of polymer–carbon nanotube composites," in *Polymer–Carbon Nanotube Composites*. Elsevier, pp. 376–399. [Online]. Available: https://linkinghub.elsevier.com/retrieve/pii/B9781845697617500137 12

[108] L. E. Helseth, "Electrical impedance spectroscopy of multiwall carbon nanotube–PDMS composites under compression," vol. 5, no. 10, p. 105002. [Online]. Available: https://iopscience.iop.org/article/10.1088/2053-1591/aada3c 12

[109] P. Song, J. Song, and Y. Zhang, "Stretchable conductor based on carbon nanotube/carbon black silicone rubber nanocomposites with highly mechanical,

electrical properties and strain sensitivity," vol. 191, p. 107979. [Online]. Available: https://linkinghub.elsevier.com/retrieve/pii/S1359836820300470 12

[110] J. Du and H.-M. Cheng, "The Fabrication, Properties, and Uses of Graphene/Polymer Composites," vol. 213, no. 10-11, pp. 1060–1077. [Online]. Available: http://doi.wiley.com/10.1002/macp.201200029 12

[111] M. Wang, X. Duan, Y. Xu, and X. Duan, "Functional Three-Dimensional Graphene/Polymer Composites," vol. 10, no. 8, pp. 7231–7247. [Online]. Available: https://pubs.acs.org/doi/10.1021/acsnano.6b03349 12, 23, 74, 76

[112] R. Rafiee and A. Eskandariyun, "Estimating Young's modulus of graphene/polymer composites using stochastic multi-scale modeling," vol. 173, p. 106842. [Online]. Available: https://linkinghub.elsevier.com/retrieve/pii/S1359836819303002 12

[113] A. Idowu, B. Boesl, and A. Agarwal, "3D graphene foam-reinforced polymer composites – A review," vol. 135, pp. 52–71. [Online]. Available: https://linkinghub.elsevier.com/retrieve/pii/S0008622318303695 12

[114] D. Verma, P. C. Gope, A. Shandilya, and A. Gupta, "Mechanical-Thermal-Electrical and Morphological Properties of Graphene Reinforced Polymer Composites: A Review," vol. 67, no. 6, pp. 803–816. [Online]. Available: http://link.springer.com/10.1007/s12666-014-0408-5 12

[115] M. T. Byrne and Y. K. Gun'ko, "Recent Advances in Research on Carbon Nanotube-Polymer Composites," vol. 22, no. 15, pp. 1672–1688. [Online]. Available: http://doi.wiley.com/10.1002/adma.200901545 12

[116] P. Alam, D. Mamalis, C. Robert, C. Floreani, and C. M. Ó Brádaigh, "The fatigue of carbon fibre reinforced plastics - A review," vol. 166, pp. 555–579. [Online]. Available: https://linkinghub.elsevier.com/retrieve/pii/S1359836818321784 12

[117] N. Behabtu, C. C. Young, D. E. Tsentalovich, O. Kleinerman, X. Wang, A. W. K. Ma, E. A. Bengio, R. F. ter Waarbeek, J. J. de Jong, R. E. Hoogerwerf, S. B. Fairchild, J. B. Ferguson, B. Maruyama, J. Kono, Y. Talmon, Y. Cohen, M. J. Otto, and M. Pasquali, "Strong, Light, Multifunctional Fibers of Carbon Nanotubes with Ultrahigh Conductivity," vol. 339, no. 6116, pp. 182–186. [Online]. Available: https://www.sciencemag.org/lookup/doi/10.1126/science.1228061 12

[118] R. Socher, B. Krause, M. T. Müller, R. Boldt, and P. Pötschke, "The influence of matrix viscosity on MWCNT dispersion and electrical properties in different thermoplastic nanocomposites," vol. 53, no. 2, pp. 495–504. [Online]. Available: https://linkinghub.elsevier.com/retrieve/pii/S0032386111010251 12

[119] A. V. Tobolsky and T. D. Callinan, "Properties and Structure of Polymers," vol. 107, no. 10, p. 243C. [Online]. Available: https://iopscience.iop.org/article/10.1149/1.2427514 13

[120] S. J. Clarson, J. J. Fitzgerald, M. J. Owen, and S. D. Smith, Eds., *Silicones and Silicone-Modified Materials*, ser. ACS Symposium Series. American Chemical Society, vol. 729. [Online]. Available: https://pubs.acs.org/doi/book/10.1021/bk-2000-0729 13

[121] A. Ferguson, A. Harvey, I. J. Godwin, S. D. Bergin, and J. N. Coleman, "The dependence of the measured surface energy of graphene on nanosheet size," vol. 4, no. 1, p. 015040. [Online]. Available: https://iopscience.iop.org/article/10.1088/2053-1583/aa50c0 13, 45

[122] A. Ferguson, I. T. Caffrey, C. Backes, J. N. Coleman, and S. D. Bergin, "Differentiating Defect and Basal Plane Contributions to the Surface Energy of Graphite Using Inverse Gas Chromatography," vol. 28, no. 17, pp. 6355–6366. [Online]. Available: https://pubs.acs.org/doi/10.1021/acs.chemmater.6b02721 13

[123] C. Hansen, *Hansen Solubility Parameters: A User's Handbook, Second Edition*. CRC Press. [Online]. Available: http://www.crcnetbase.com/doi/book/10.1201/9781420006834 13, 22, 51, 52

[124] P. Lee, J. Lee, H. Lee, J. Yeo, S. Hong, K. H. Nam, D. Lee, S. S. Lee, and S. H. Ko, "Highly stretchable and highly conductive metal electrode by very long metal nanowire percolation network," vol. 24, no. 25, pp. 3326–3332. 13, 23, 74, 76

[125] A. Noël, J. Faucheu, J.-M. Chenal, J.-P. Viricelle, and E. Bourgeat-Lami, "Electrical and mechanical percolation in graphene-latex nanocomposites," vol. 55, no. 20, pp. 5140–5145. [Online]. Available: https://linkinghub.elsevier.com/retrieve/pii/S0032386114007174 13, 14, 15, 16

[126] P. M. Kogut and J. P. Straley, "Distribution-induced non-universality of the percolation conductivity exponents," vol. 12, no. 11, pp. 2151–2159. [Online]. Available: https://iopscience.iop.org/article/10.1088/0022-3719/12/11/023 14, 97

[127] M. El Achaby, F.-E. Arrakhiz, S. Vaudreuil, A. el Kacem Qaiss, M. Bousmina, and O. Fassi-Fehri, "Mechanical, thermal, and rheological properties of graphene-based polypropylene nanocomposites prepared by melt mixing," vol. 33, no. 5, pp. 733–744. [Online]. Available: http://doi.wiley.com/10.1002/pc.22198 14

[128] M. El Achaby, F. Z. Arrakhiz, S. Vaudreuil, E. M. Essassi, A. Qaiss, and M. Bousmina, "Preparation and characterization of melt-blended graphene nanosheets-poly(vinylidene fluoride) nanocomposites with enhanced properties," vol. 127, no. 6, pp. 4697–4707. [Online]. Available: http://doi.wiley.com/10.1002/app.38081 14

[129] H.-B. Zhang, W.-G. Zheng, Q. Yan, Y. Yang, J.-W. Wang, Z.-H. Lu, G.-Y. Ji, and Z.-Z. Yu, "Electrically conductive polyethylene terephthalate/graphene

nanocomposites prepared by melt compounding," vol. 51, no. 5, pp. 1191–1196. [Online]. Available: https://linkinghub.elsevier.com/retrieve/pii/S003238611000056X 14

[130] O. M. Istrate, K. R. Paton, U. Khan, A. O'Neill, A. P. Bell, and J. N. Coleman, "Reinforcement in melt-processed polymer–graphene composites at extremely low graphene loading level," vol. 78, pp. 243–249. [Online]. Available: https://linkinghub.elsevier.com/retrieve/pii/S000862231400623X 14

[131] D. Verma and K. L. Goh, "Functionalized Graphene-Based Nanocomposites for Energy Applications," in *Functionalized Graphene Nanocomposites and Their Derivatives*. Elsevier, pp. 219–243. [Online]. Available: https://linkinghub.elsevier.com/retrieve/pii/B9780128145487000118 15

[132] J. Hicks, A. Behnam, and A. Ural, "A computational study of tunneling-percolation electrical transport in graphene-based nanocomposites," vol. 95, no. 21, p. 213103. [Online]. Available: http://aip.scitation.org/doi/10.1063/1.3267079 15

[133] C. M. Hansen, "50 Years with solubility parameters—past and future," vol. 51, no. 1, pp. 77–84. [Online]. Available: https://linkinghub.elsevier.com/retrieve/pii/S0300944004001298 15

[134] J. J. Richardson, J. Cui, M. Björnmalm, J. A. Braunger, H. Ejima, and F. Caruso, "Innovation in Layer-by-Layer Assembly," vol. 116, no. 23, pp. 14 828–14 867. [Online]. Available: https://pubs.acs.org/doi/10.1021/acs.chemrev.6b00627 15

[135] Y. Chevalier and M.-A. Bolzinger, "Emulsions stabilized with solid nanoparticles: Pickering emulsions," vol. 439, pp. 23–34. [Online]. Available: https://linkinghub.elsevier.com/retrieve/pii/S092777571300157X 15, 16, 38, 44

[136] R. McGorty, J. Fung, D. Kaz, and V. N. Manoharan, "Colloidal self-assembly at an interface," vol. 13, no. 6, pp. 34–42. [Online]. Available: https://linkinghub.elsevier.com/retrieve/pii/S1369702110701073 15, 16, 38

[137] Q. Monégier du Sorbier, A. Aimable, and C. Pagnoux, "Influence of the electrostatic interactions in a Pickering emulsion polymerization for the synthesis of silica–polystyrene hybrid nanoparticles," vol. 448, pp. 306–314. [Online]. Available: https://linkinghub.elsevier.com/retrieve/pii/S0021979715001733 15, 16, 25, 38

[138] T. Ngai and S. A. F. Bon, Eds., *Particle-Stabilized Emulsions and Colloids: Formation and Applications*, ser. RSC Soft Matter Series. Royal Society of Chemistry, no. v.3. 15, 16, 38

[139] Y. Yang, Z. Fang, X. Chen, W. Zhang, Y. Xie, Y. Chen, Z. Liu, and W. Yuan, "An Overview of Pickering Emulsions: Solid-Particle Materials, Classification, Morphology, and Applications," vol. 8, p. 287. [Online]. Available: http://journal.frontiersin.org/article/10.3389/fphar.2017.00287/full 15, 16, 38

[140] P. Steward, J. Hearn, and M. Wilkinson, "An overview of polymer latex film formation and properties," vol. 86, no. 3, pp. 195–267. [Online]. Available: https://linkinghub.elsevier.com/retrieve/pii/S0001868699000378 15, 16

[141] D. C. Sundberg and Y. G. Durant, "Latex Particle Morphology, Fundamental Aspects: A Review," vol. 11, no. 3, pp. 379–432. [Online]. Available: https://www.tandfonline.com/doi/full/10.1081/PRE-120024420 15, 16

[142] W. Xing, M. Tang, J. Wu, G. Huang, H. Li, Z. Lei, X. Fu, and H. Li, "Multifunctional properties of graphene/rubber nanocomposites fabricated by a modified latex compounding method," vol. 99, pp. 67–74. [Online]. Available: https://linkinghub.elsevier.com/retrieve/pii/S0266353814001584 16

[143] N. P. Ashby and B. P. Binks, "Pickering emulsions stabilised by Laponite clay particles," vol. 2, no. 24, pp. 5640–5646. [Online]. Available: http://xlink.rsc.org/?DOI=b007098j 16, 38

[144] S. Cauvin, P. J. Colver, and S. A. F. Bon, "Pickering Stabilized Miniemulsion Polymerization: Preparation of Clay Armored Latexes," vol. 38, no. 19, pp. 7887–7889. [Online]. Available: https://pubs.acs.org/doi/10.1021/ma051070z 16, 38

[145] Y. He, F. Wu, X. Sun, R. Li, Y. Guo, C. Li, L. Zhang, F. Xing, W. Wang, and J. Gao, "Factors that Affect Pickering Emulsions Stabilized by Graphene Oxide," vol. 5, no. 11, pp. 4843–4855. [Online]. Available: https://pubs.acs.org/doi/10.1021/am400582n 16, 38

[146] M. J. Large, S. P. Ogilvie, M. Meloni, A. Amorim Graf, G. Fratta, J. Salvage, A. A. K. King, and A. B. Dalton, "Functional liquid structures by emulsification of graphene and other two-dimensional nanomaterials," vol. 10, no. 4, pp. 1582–1586. [Online]. Available: http://xlink.rsc.org/?DOI=C7NR05568D 16, 38

[147] S. J. Woltornist, J.-M. Y. Carrillo, T. O. Xu, A. V. Dobrynin, and D. H. Adamson, "Polymer/Pristine Graphene Based Composites: From Emulsions to Strong, Electrically Conducting Foams," vol. 48, no. 3, pp. 687–693. [Online]. Available: https://pubs.acs.org/doi/10.1021/ma5024236 16, 19, 20, 38

[148] S. J. Woltornist, D. Varghese, D. Massucci, Z. Cao, A. V. Dobrynin, and D. H. Adamson, "Controlled 3D Assembly of Graphene Sheets to Build Conductive, Chemically Selective and Shape-Responsive Materials," vol. 29, no. 18, p. 1604947. [Online]. Available: http://doi.wiley.com/10.1002/adma.201604947 16, 19, 38

[149] F. Chen, D. Varghese, S. T. McDermott, I. George, L. Geng, and D. H. Adamson, "Interface-exfoliated graphene-based conductive screen-printing inks:

Low-loading, low-cost, and additive-free," vol. 10, no. 1, p. 18047. [Online]. Available: http://www.nature.com/articles/s41598-020-74821-3 16

[150] S. P. Ogilvie, M. J. Large, A. J. Cass, A. A. Graf, A. C. Sehnal, M. A. O'Mara, P. J. Lynch, J. P. Salvage, M. Alfonso, P. Poulin, A. A. K. King, and A. B. Dalton. Nanosheet-stabilized emulsions: Ultra-low loading segregated networks and surface energy determination of pristine few-layer 2D materials. [Online]. Available: http://arxiv.org/abs/2005.06330 16, 25, 96, 97

[151] U. Khan, H. Porwal, A. O'Neill, K. Nawaz, P. May, and J. N. Coleman, "Solvent-Exfoliated Graphene at Extremely High Concentration," vol. 27, no. 15, pp. 9077–9082. [Online]. Available: https://pubs.acs.org/doi/10.1021/la201797h 17

[152] H. Pang, T. Chen, G. Zhang, B. Zeng, and Z.-M. Li, "An electrically conducting polymer/graphene composite with a very low percolation threshold," vol. 64, no. 20, pp. 2226–2229. [Online]. Available: https://linkinghub.elsevier.com/retrieve/pii/S0167577X10005379 19

[153] X.-Y. Qi, D. Yan, Z. Jiang, Y.-K. Cao, Z.-Z. Yu, F. Yavari, and N. Koratkar, "Enhanced Electrical Conductivity in Polystyrene Nanocomposites at Ultra-Low Graphene Content," vol. 3, no. 8, pp. 3130–3133. [Online]. Available: https://pubs.acs.org/doi/10.1021/am200628c 19

[154] Y. Lu, M. C. Biswas, Z. Guo, J.-W. Jeon, and E. K. Wujcik, "Recent developments in bio-monitoring via advanced polymer nanocomposite-based wearable strain sensors," vol. 123, pp. 167–177. [Online]. Available: https://linkinghub.elsevier.com/retrieve/pii/S0956566318306365 20

[155] C. S. Boland, "Stumbling through the Research Wilderness, Standard Methods To Shine Light on Electrically Conductive Nanocomposites for

Future Healthcare Monitoring," p. acsnano.9b06847. [Online]. Available: https://pubs.acs.org/doi/10.1021/acsnano.9b06847 20, 23, 68, 72, 74, 76, 108, 110, 111, 112

[156] M. Bao, "Introduction to MEMS Devices," in *Analysis and Design Principles of MEMS Devices*. Elsevier, pp. 1–32. [Online]. Available: https://linkinghub.elsevier.com/retrieve/pii/B9780444516169500023 20

[157] M. Pyo, C. C. Bohn, E. Smela, J. R. Reynolds, and A. B. Brennan, "Direct Strain Measurement of Polypyrrole Actuators Controlled by the Polymer/Gold Interface," vol. 15, no. 4, pp. 916–922. [Online]. Available: https://pubs.acs.org/doi/10.1021/cm020312w 20

[158] V. Koncar, "Composites and hybrid structures," in *Smart Textiles for In Situ Monitoring of Composites*. Elsevier, pp. 153–215. [Online]. Available: https://linkinghub.elsevier.com/retrieve/pii/B9780081023082000024 21

[159] P. H. Mott and C. M. Roland, "Limits to Poisson's ratio in isotropic materials - general result for arbitrary deformation," vol. 87, no. 5, p. 055404. [Online]. Available: http://arxiv.org/abs/1204.3859 21

[160] P. K. Freakley, A. R. Payne, and A. B. Davey, *Theory and Practice of Engineering with Rubber*. Applied Science Publishers. 21

[161] C. S. Boland, U. Khan, M. Binions, S. Barwich, J. B. Boland, D. Weaire, and J. N. Coleman, "Graphene-coated polymer foams as tuneable impact sensors," vol. 10, no. 11, pp. 5366–5375. [Online]. Available: http://xlink.rsc.org/?DOI=C7NR09247D 21, 110

[162] L. Pan, A. Chortos, G. Yu, Y. Wang, S. Isaacson, R. Allen, Y. Shi, R. Dauskardt, and Z. Bao, "An ultra-sensitive resistive pressure sensor based on hollow-sphere

microstructure induced elasticity in conducting polymer film," vol. 5, no. 1, p. 3002. [Online]. Available: http://www.nature.com/articles/ncomms4002 21

[163] L. Zhao, B. Jiang, and Y. Huang, "Self-healable polysiloxane/graphene nanocomposite and its application in pressure sensor," vol. 54, no. 7, pp. 5472–5483. [Online]. Available: http://link.springer.com/10.1007/s10853-018-03233-6 21

[164] J. Lee, S. Kim, J. Lee, D. Yang, B. C. Park, S. Ryu, and I. Park, "A stretchable strain sensor based on a metal nanoparticle thin film for human motion detection," vol. 6, no. 20, pp. 11 932–11 939. 23, 74, 76

[165] K. Takei, Z. Yu, M. Zheng, H. Ota, T. Takahashi, and A. Javey, "Highly sensitive electronic whiskers based on patterned carbon nanotube and silver nanoparticle composite films," vol. 111, no. 5, pp. 1703–1707. 23, 74, 76

[166] D. Kang, P. V. Pikhitsa, Y. W. Choi, C. Lee, S. S. Shin, L. Piao, B. Park, K.-Y. Suh, T.-i. Kim, and M. Choi, "Ultrasensitive mechanical crack-based sensor inspired by the spider sensory system," vol. 516, no. 7530, p. 222. 23, 74, 76

[167] S. Zhu, J.-H. So, R. Mays, S. Desai, W. R. Barnes, B. Pourdeyhimi, and M. D. Dickey, "Ultrastretchable fibers with metallic conductivity using a liquid metal alloy core," vol. 23, no. 18, pp. 2308–2314. 23, 74, 76

[168] S.-H. Bae, Y. Lee, B. K. Sharma, H.-J. Lee, J.-H. Kim, and J.-H. Ahn, "Graphene-based transparent strain sensor," vol. 51, pp. 236–242. 23, 74, 76

[169] Q. Liu, M. Zhang, L. Huang, Y. Li, J. Chen, C. Li, and G. Shi, "High-quality graphene ribbons prepared from graphene oxide hydrogels and their application for strain sensors," vol. 9, no. 12, pp. 12 320–12 326. 23, 74, 76

[170] X. Liao, Q. Liao, X. Yan, Q. Liang, H. Si, M. Li, H. Wu, S. Cao, and Y. Zhang, "Flexible and highly sensitive strain sensors fabricated by pencil drawn for wearable monitor," vol. 25, no. 16, pp. 2395–2401. 23, 74, 76

[171] S.-J. Park, J. Kim, M. Chu, and M. Khine, "Highly Flexible Wrinkled Carbon Nanotube Thin Film Strain Sensor to Monitor Human Movement," vol. 1, no. 5, p. 1600053. [Online]. Available: http://doi.wiley.com/10.1002/admt.201600053 23, 74, 76

[172] Q. Liu, J. Chen, Y. Li, and G. Shi, "High-Performance Strain Sensors with Fish-Scale-Like Graphene-Sensing Layers for Full-Range Detection of Human Motions," vol. 10, no. 8, pp. 7901–7906. [Online]. Available: https://pubs.acs.org/doi/10.1021/acsnano.6b03813 23, 74, 76

[173] Y. Cheng, R. Wang, J. Sun, and L. Gao, "A Stretchable and Highly Sensitive Graphene-Based Fiber for Sensing Tensile Strain, Bending, and Torsion," vol. 27, no. 45, pp. 7365–7371. [Online]. Available: http://doi.wiley.com/10.1002/adma.201503558 23, 74, 76

[174] M. Hempel, D. Nezich, J. Kong, and M. Hofmann, "A Novel Class of Strain Gauges Based on Layered Percolative Films of 2D Materials," vol. 12, no. 11, pp. 5714–5718. [Online]. Available: https://pubs.acs.org/doi/10.1021/nl302959a 23, 74, 76

[175] C. S. Boland, U. Khan, C. Backes, A. O'Neill, J. McCauley, S. Duane, R. Shanker, Y. Liu, I. Jurewicz, A. B. Dalton, and J. N. Coleman, "Sensitive, High-Strain, High-Rate Bodily Motion Sensors Based on Graphene–Rubber Composites," vol. 8, no. 9, pp. 8819–8830. [Online]. Available: https://pubs.acs.org/doi/10.1021/nn503454h 23, 54, 74, 76, 80, 108, 111

[176] S. Jiang, H. Zhang, S. Song, Y. Ma, J. Li, G. H. Lee, Q. Han, and J. Liu, "Highly Stretchable Conductive Fibers from Few-Walled Carbon Nanotubes Coated on Poly(*m* -phenylene isophthalamide) Polymer Core/Shell Structures," vol. 9, no. 10, pp. 10 252–10 257. [Online]. Available: https://pubs.acs.org/doi/10.1021/acsnano.5b04185 23, 74, 76

[177] P. Lee, J. Ham, J. Lee, S. Hong, S. Han, Y. D. Suh, S. E. Lee, J. Yeo, S. S. Lee, D. Lee, and S. H. Ko, "Highly Stretchable or Transparent Conductor Fabrication by a Hierarchical Multiscale Hybrid Nanocomposite," vol. 24, no. 36, pp. 5671–5678. [Online]. Available: http://doi.wiley.com/10.1002/adfm.201400972 23, 74, 76

[178] M. Zhang, C. Wang, H. Wang, M. Jian, X. Hao, and Y. Zhang, "Carbonized Cotton Fabric for High-Performance Wearable Strain Sensors," vol. 27, no. 2, p. 1604795. [Online]. Available: http://doi.wiley.com/10.1002/adfm.201604795 23, 74, 76

[179] G. Cai, J. Wang, K. Qian, J. Chen, S. Li, and P. S. Lee, "Extremely Stretchable Strain Sensors Based on Conductive Self-Healing Dynamic Cross-Links Hydrogels for Human-Motion Detection," vol. 4, no. 2, p. 1600190. [Online]. Available: http://doi.wiley.com/10.1002/advs.201600190 23, 74, 76

[180] S. Chen, Y. Wei, S. Wei, Y. Lin, and L. Liu, "Ultrasensitive Cracking-Assisted Strain Sensors Based on Silver Nanowires/Graphene Hybrid Particles," vol. 8, no. 38, pp. 25 563–25 570. [Online]. Available: https://pubs.acs.org/doi/10.1021/acsami.6b09188 23, 74, 76

[181] T. F. Tadros, "Emulsion Formation, Stability, and Rheology," in *Emulsion Formation and Stability*, T. F. Tadros, Ed. Wiley-VCH Verlag GmbH & Co. KGaA, pp. 1–75. [Online]. Available: http://doi.wiley.com/10.1002/9783527647941.ch1 22

[182] *Basic Theory of Interfacial Phenomena and Colloid Stability.* De Gruyter. [Online]. Available: https://www.degruyter.com/view/title/536630 24

[183] T. F. Tadros, *Emulsions: Formation, Stability, Industrial Applications.* De Gruyter. [Online]. Available: https://www.degruyter.com/view/title/516852 24

[184] P. W. Voorhees, "The theory of Ostwald ripening," vol. 38, no. 1-2, pp. 231–252. [Online]. Available: http://link.springer.com/10.1007/BF01017860 24

[185] T. Tadros, "Phase Inversion," in *Encyclopedia of Colloid and Interface Science*, T. Tadros, Ed. Springer Berlin Heidelberg, pp. 930–930. [Online]. Available: http://link.springer.com/10.1007/978-3-642-20665-8_128 24

[186] V. Menon and D. Wasan, "Characterization of oil—water interfaces containing finely divided solids with applications to the coalescence of water-in-oil Emulsions: A review," vol. 29, no. 1, pp. 7–27. [Online]. Available: https://linkinghub.elsevier.com/retrieve/pii/0166662288801690 25

[187] B. P. Binks and J. H. Clint, "Solid Wettability from Surface Energy Components: Relevance to Pickering Emulsions," vol. 18, no. 4, pp. 1270–1273. [Online]. Available: https://pubs.acs.org/doi/10.1021/la011420k 25

[188] R. Aveyard, B. P. Binks, and J. H. Clint, "Emulsions stabilised solely by colloidal particles," vol. 100-102, pp. 503–546. [Online]. Available: https://linkinghub.elsevier.com/retrieve/pii/S0001868602000696 25

[189] J. Lyklema, "The surface tension of pure liquids," vol. 156, no. 1-3, pp. 413–421. [Online]. Available: https://linkinghub.elsevier.com/retrieve/pii/S0927775799001004 25, 45

[190] A. Harvey, C. Backes, Z. Gholamvand, D. Hanlon, D. McAteer, H. C. Nerl, E. McGuire, A. Seral-Ascaso, Q. M. Ramasse, N. McEvoy, S. Winters, N. C.

Berner, D. McCloskey, J. F. Donegan, G. S. Duesberg, V. Nicolosi, and J. N. Coleman, "Preparation of Gallium Sulfide Nanosheets by Liquid Exfoliation and Their Application As Hydrogen Evolution Catalysts," vol. 27, no. 9, pp. 3483–3493. [Online]. Available: https://pubs.acs.org/doi/10.1021/acs.chemmater.5b00910 28

[191] A. A. Graf, S. P. Ogilvie, H. J. Wood, C. J. Brown, M. Tripathi, A. A. K. King, A. B. Dalton, and M. J. Large, "Raman Metrics for Molybdenum Disulfide and Graphene Enable Statistical Mapping of Nanosheet Populations," vol. 32, no. 14, pp. 6213–6221. [Online]. Available: https://pubs.acs.org/doi/10.1021/acs.chemmater.0c02109 29, 92

[192] M. Hulman, "Raman spectroscopy of graphene," in *Graphene*. Elsevier, pp. 156–183. [Online]. Available: https://linkinghub.elsevier.com/retrieve/pii/B9780857095084500071 30

[193] M. Lotya, A. Rakovich, J. F. Donegan, and J. N. Coleman, "Measuring the lateral size of liquid-exfoliated nanosheets with dynamic light scattering," vol. 24, no. 26, p. 265703. [Online]. Available: https://iopscience.iop.org/article/10.1088/0957-4484/24/26/265703 35, 92

[194] S. Fujime and K. Kubota, "Dynamic light scattering from dilute suspensions of thin discs and thin rods as limiting forms of cylinder, ellipsoid and ellipsoidal shell of revolution," vol. 23, no. 1-2, pp. 1–13. [Online]. Available: https://linkinghub.elsevier.com/retrieve/pii/0301462285800594 35

[195] L.-Y. Chu, A. S. Utada, R. K. Shah, J.-W. Kim, and D. A. Weitz, "Controllable monodisperse multiple emulsions," vol. 119, no. 47, pp. 9128–9132. [Online]. Available: http://doi.wiley.com/10.1002/ange.200701358 39

[196] A. J. C. A. A. G. A. C. S. M. A. O. P. J. L. J. P. S. A. A. K. K. A. B. D. Sean P. Ogilvie, Matthew J. Large, "Nanosheet-stabilised emulsions: Ultra-low loading

segregated networks and surface energy determination of pristine few-layer 2D materials (Submitted)." 40, 42, 44

[197] F. M. Fowkes, "Determination of interfacial tensions, contact angles, and dispersion forces in surfaces by assuming additivity of intermolecular interactions in surfaces," vol. 66, no. 2, pp. 382–382. [Online]. Available: https://pubs.acs.org/doi/abs/10.1021/j100808a524 49

[198] S. Ebnesajjad, "Introduction to Plastics," in *Chemical Resistance of Commodity Thermoplastics*. Elsevier, pp. xiii–xxv. [Online]. Available: https://linkinghub.elsevier.com/retrieve/pii/B978032347358300017X 51

[199] J. Mazan, B. Leclerc, N. Galandrin, and G. Couarraze, "Diffusion of free polydimethylsiloxane chains in polydimethylsiloxane elastomer networks," vol. 31, no. 8, pp. 803–807. [Online]. Available: https://linkinghub.elsevier.com/retrieve/pii/0014305795000399 54

[200] M. Appel and G. Fleischer, "Investigation of the chain length dependence of self-diffusion of poly(dimethylsiloxane) and poly(ethylene oxide) in the melt with pulsed field gradient NMR," vol. 26, no. 20, pp. 5520–5525. [Online]. Available: https://pubs.acs.org/doi/abs/10.1021/ma00072a033 59

[201] Q. Liu and D. De Kee, "Modeling of diffusion through nanocomposite membranes," vol. 131, no. 1-3, pp. 32–43. [Online]. Available: https://linkinghub.elsevier.com/retrieve/pii/S0377025705001692 59

[202] J. Keddie and A. F. Routh, *Fundamentals of Latex Film Formation Processes and Properties*. 62, 109

[203] T. G. Beckwith, N. L. Buck, and R. D. Marangoni, *Mechanical Measurements*, 3rd ed. Addison-Wesley Pub. Co. 72

[204] Y. Huang, X. Fan, S. Chen, and N. Zhao, "Emerging Technologies of Flexible Pressure Sensors: Materials, Modeling, Devices, and Manufacturing," vol. 29, no. 12, p. 1808509. [Online]. Available: https://onlinelibrary.wiley.com/doi/abs/10.1002/adfm.201808509 87

[205] T. Swan, "Elicarb Premium Grade Powder Product Datasheet." 88

[206] L. N. Lewis, J. Stein, Y. Gao, R. E. Colborn, and G. Hutchins, "Platinum catalysts used in the silicones industry," *Platinum Metals Review*, vol. 41, no. 2, pp. 66–75, 1997. 88, 89

[207] *QSil216 Technical Data Sheet*, ACC Silicones, 12 2005. [Online]. Available: https://www.farnell.com/datasheets/2041211.pdf 89

[208] *Ecoflex 00-30 Technical Data Sheet*, Smooth-On. [Online]. Available: https://www.smooth-on.com/tb/files/ECOFLEX_SERIES_TB.pdf 89

[209] N. Patra, A. C. Barone, and M. Salerno, "Solvent effects on the thermal and mechanical properties of poly(methyl methacrylate) casted from concentrated solutions," vol. 30, no. 1, pp. 12–20. [Online]. Available: http://doi.wiley.com/10.1002/adv.20203 90

[210] N. Ioannou, H. Liu, and Y. Zhang, "Droplet dynamics in confinement," vol. 17, pp. 463–474. [Online]. Available: https://linkinghub.elsevier.com/retrieve/pii/S1877750316300308 90

[211] R. R. Nair, P. Blake, A. N. Grigorenko, K. S. Novoselov, T. J. Booth, T. Stauber, N. M. R. Peres, and A. K. Geim, "Fine Structure Constant Defines Visual Transparency of Graphene," vol. 320, no. 5881, pp. 1308–1308. [Online]. Available: https://www.sciencemag.org/lookup/doi/10.1126/science.1156965 94

[212] N. Lindahl, D. Midtvedt, J. Svensson, O. A. Nerushev, N. Lindvall, A. Isacsson, and E. E. B. Campbell, "Determination of the Bending Rigidity of Graphene via Electrostatic Actuation of Buckled Membranes," vol. 12, no. 7, pp. 3526–3531. [Online]. Available: https://pubs.acs.org/doi/10.1021/nl301080v 94

[213] J. Bergström, "Introduction and Overview," in *Mechanics of Solid Polymers*. Elsevier, pp. 1–17. [Online]. Available: https://linkinghub.elsevier.com/retrieve/pii/B9780323311502000017 104

[214] X. Li, R. Zhang, W. Yu, K. Wang, J. Wei, D. Wu, A. Cao, Z. Li, Y. Cheng, Q. Zheng, R. S. Ruoff, and H. Zhu, "Stretchable and highly sensitive graphene-on-polymer strain sensors," vol. 2, no. 1, p. 870. [Online]. Available: http://www.nature.com/articles/srep00870 111

[215] P. Worajittiphon, M. J. Large, A. A. K. King, I. Jurewicz, and A. B. Dalton, "Stretchable Conductive Networks of Carbon Nanotubes Using Plasticized Colloidal Templates," vol. 2. [Online]. Available: http://journal.frontiersin.org/Article/10.3389/fmats.2015.00015/abstract 111